Monte Carlo simulation of the GE Discovery MI 4-Ring PET/CT scanner : from validation of NEMA performance to reconstruction of simulated data

Antoine Merlet

UBFC
UNIVERSITÉ
BOURGOGNE FRANCHE-COMTÉ

UNIVERSITÉ DE BOURGOGNE

THÈSE DE DOCTORAT DE L'ÉTABLISSEMENT UNIVERSITÉ BOURGOGNE FRANCHE-COMTÉ

PRÉPARÉE À L'UNIVERSITÉ DE BOURGOGNE

École doctorale n°37
Sciences Pour l'Ingénieur et Microtechniques

Doctorat d'Instrumentation et informatique de l'image

par

ANTOINE MERLET

Monte Carlo simulation of the GE Discovery MI 4-Ring PET/CT scanner: from validation of NEMA performance to reconstruction of simulated data

Thèse présentée et soutenue à Dijon, le 19 mars 2024

Composition du Jury :

VISVIKIS DIMITRIS	Directeur de recherche INSERM (LATIM, Brest)	Rapporteur
JAN SÉBASTIEN	Directeur de recherche CEA (SHFJ, Orsay)	Rapporteur
LJUNGBERG MICHAEL	Professeur (Université de Lund, Lund)	Examinateur, Président
COCHET ALEXANDRE	PU-PH (Université de Bourgogne, Dijon)	Directeur de thèse
VRIGNEAUD JEAN-MARC	Physicien médical, HDR (CGFL, Dijon)	Codirecteur de thèse
PRESLES BENOÎT	MCU (Université de Bourgogne, Dijon)	Encadrant de thèse
PASQUIER HUGO	Chef de projet Recherche (GEHC, Buc)	Invité

N° | . | . | .

école doctorale **sciences pour l'ingénieur et microtechniques**

Title: Monte Carlo simulation of the GE Discovery MI 4-Ring PET/CT scanner: from validation of NEMA performance to reconstruction of simulated data

Keywords: PET, GATE, NEMA, SiPM, TOF

Abstract:

Positron emission tomography (PET) / computed tomography (CT) is a well-established molecular imaging technique for cancer diagnosis and treatment response monitoring. Its use in routine clinical practice has increased steadily in recent years, and its performance has continued to improve over time. Recent developments such as time-of-flight (TOF), point-spread function modelling, digital PET detectors (SiPMs), and long axial field-of-view have further enhanced the imaging capabilities of the technique. The use of Monte Carlo simulations in PET has long been recognised as a valuable tool to study the impact of different parameters on the quality of PET images (acquisition, reconstruction, corrections, etc.) with more flexibility than could be achieved with a physical phantom, while requiring fewer resources and less expense. In this thesis, our aim was to develop a complete GATE (Monte Carlo simulator) model of the SiPM-based and TOF-capable 4-ring General Electric Discovery MI (DMI4) PET/CT scanner.

The performance characteristics of the DMI4 scanner were evaluated over several years in accordance with the latest NEMA standard, and compared with results found in the literature for this scanner. Specifically, the DMI4 was characterised in terms of sensitivity, count losses and scatter fraction, spatial resolution, and image quality. The energy and temporal resolution of the DMI were also evaluated and compared with those of the literature, but outside the scope of the NEMA standard. Using the data obtained from the performance evaluations (raw data and expected results), we developed and validated our own NEMA analysis software (NEAT), which also included methods to organise the experimental data into sinograms. With this software, we could then evaluate the performance of our GATE model and adequately compare them to that of our DMI4 scanner.

We have reported the methodology used to design, optimise, and validate our GATE model of the DMI4 scanner. We have shown that our model has a performance very similar to that of our DMI4 scanner in terms of sensitivity, count rates, and spatial resolution. To study the image quality of the reconstructed images, we developed a reconstruction framework based on the clinical reconstruction tools provided with the DMI4 scanner (algorithm and correction). We have shown that the joint use of this framework and our GATE model could produce realistic PET images when performing clinical-like TOF-OSEM reconstructions. Finally, we have detailed the difficulties associated with the evaluation of the NEMA TOF resolution of the DMI4 (first generation), which only records compressed TOF information, thus hindering the analysis. We have shown that using our analysis software, it is possible to evaluate the NEMA TOF resolution of both the DMI4 and its GATE model.

UBFC UNIVERSITÉ BOURGOGNE FRANCHE-COMTÉ

Université Bourgogne Franche-Comté
32, avenue de l'Observatoire
25000 Besançon, France

école doctorale **sciences pour l'ingénieur et microtechniques**

Titre : Simulation Monte Carlo du scanneur TEP/TDM GE Discovery MI 4 anneaux : de la validation des performances NEMA à la reconstruction des données simulées

Mots-clés : TEP, GATE, NEMA, SiPM, TOF

Résumé :

La tomographie par émission de positons (TEP) / tomodensitométrie (TDM) est une technique d'imagerie moléculaire bien établie pour le diagnostic du cancer et le suivi de la réponse au traitement. Son utilisation dans la pratique clinique de routine a augmenté régulièrement ces dernières années et ses performances ont continué à s'améliorer au fil du temps. Des développements récents tels que le temps de vol (TOF), la modélisation de la fonction de dispersion ponctuelle, les détecteurs TEP numériques (SiPM) et le long champ de vue axial ont amélioré les capacités de cette technique d'imagerie. L'utilisation de simulations Monte Carlo en TEP est reconnue depuis longtemps comme un outil précieux pour étudier l'impact de différents paramètres (acquisition, reconstruction, corrections, etc.) sur la qualité des images TEP. De plus, un tel environemment de simulation offre plus de flexibilité que ce qui pourrait être obtenu avec un fantôme physique, tout en nécessitant moins de ressources et moins de dépenses. Dans cette thèse, notre objectif était de développer un modèle GATE (simulateur Monte Carlo) complet du scanner TEP/TDM General Electric Discovery MI à 4 anneaux (DMI4), qui est un TEP numérique capable d'utiliser l'information TOF.

Les caractéristiques de performance du scanner DMI4 ont été évaluées sur plusieurs années conformément au dernier rapport NEMA et comparées à celle reportées dans la littérature pour ce même système. Plus précisément, le DMI4 a été caractérisé en termes de sensibilité, de pertes de taux de comptage et de fraction de diffusé, de résolution spatiale, et de qualité d'image. L'énergie et la résolution temporelle du DMI4 ont également été évaluées et comparées à celles de la littérature, mais en dehors du champ d'application du rapport NEMA. En utilisant les données obtenues lors des évaluations de performance (données brutes et résultats attendus), nous avons développé et validé notre propre logiciel d'analyse NEMA (NEAT), qui contient également des méthodes pour organiser les données expérimentales en sinogrammes. Grâce à ce logiciel, nous avons pu évaluer les performances de notre modèle GATE et les comparer de manière adéquate à celles de notre TEP/TDM.

Nous avons ensuite présenté la méthodologie utilisée pour concevoir, optimiser et valider notre modèle GATE du DMI4. Nous avons montré que notre modèle avait des performances très proches de celles du DMI4 en termes de sensibilité, de taux de comptage et de résolution spatiale. Pour étudier la qualité des images reconstruites, nous avons développé un logiciel basé sur les outils de reconstruction clinique fournis avec le scanner DMI4 (algorithme et corrections). Nous avons montré que ce logiciel, combiné à notre modèle GATE, était capable de produire des images TEP réalistes pour des reconstructions TOF-OSEM de type clinique. Enfin, nous avons détaillé les difficultés liées à l'évaluation de la résolution TOF de notre système selon NEMA. En effet, les données TOF du DMI4 (première génération) sont compressées et ne peuvent pas être utilisées telles quelles pour l'analyse NEMA. Nous avons développé une méthode permettant de le faire et nous avons évalué la résolution NEMA TOF du DMI4 et de son modèle GATE.

UBFC UNIVERSITÉ BOURGOGNE FRANCHE-COMTÉ

Université Bourgogne Franche-Comté
32, avenue de l'Observatoire
25000 Besançon, France

1

ACKNOWLEDGEMENTS

During the years it took to complete this thesis, I was blessed by the scientific guidance and moral support of many individuals, including colleagues, friends, and family.

First and foremost, I would like to express my deepest gratitude to my thesis co-director Dr. Jean-Marc Vrigneaud, without whom this work could never have reached its completion. You taught me everything I now know about physics and never once seemed annoyed by my mistakes and initial lack of understanding. Your patience was second only to your kindness, and I still wonder if I truly deserved both. I could never thank you enough for the time you spent directing my research. I can only hope to become a fraction of the researcher and person you were.

My sincere gratitude also goes to my thesis supervisor, Dr. Benoît Presles, who showed me what scientific rigor truly is. I will miss our whiteboard sessions. I also thank you for the trust you placed in my ability to produce the software solutions needed throughout this thesis.

My thanks also go to Pr. Alexandre Cochet, my thesis director, for his trust and kindness. Despite the delays and hiccups, you continued to believe in the project and allowed us to steer the research in what we thought were the best directions.

I also express my gratitude to Farzam Sayah and Hanieh Jozi, two internship students I had the pleasure of working with. Your respective projects helped me advance my research further than I could have ever achieved alone.

I would also like to thank General Electric Healthcare, particularly two of its members who provided invaluable support. I extend my gratitude to Dr. Hugo Pasquier for overseeing this project and providing us with the crucial information we needed. My deepest thanks also go to Dr. Kuan-Hao Su, whose tremendous knowledge regarding DMI engineering was key to the success of this thesis.

My deepest gratitude goes to Dr. David Sarrut, who took time to help the young clueless reseracher I was. Your knowledge got me out of a seemingly inescapable dead-end, thank you so much.

I would also like to thank all my friends, starting with Julien, who is certainly the best encounter of my thesis. I deeply enjoyed our ”think-calls”, and while we sometimes talked in circles, it never resulted in a loss of time (dead time?). I gained a deep understanding of PET simulations thanks to our discussions, and being able to expose and debate my research problems with you was a relief. Man, I can never express the extent of my gratitude.

Je souhaite remercier mes amis, Elie, Luca et Thibault. Nos soirées du lundi étaient un véritable échappatoire. Merci d'avoir supporté les plats que j'ai préparés, car ils étaient au moins aussi épicés que mon caractère. Je ne compte plus le nombre de jeux de tarot que nous avons écornés. "Et celui-là, il est complet ?". Un grand merci à Mathilde et Romuald. Passer des heures au téléphone à discuter de tout et de rien avec vous était un vrai plaisir. Enfin, merci à Romain et Yohan, qui m'ont offert des moments de détente malgré la distance.

Ma gratitude la plus profonde va à ma famille, qui m'a toujours supporté, dans les deux sens du terme. À mes parents, qui ont toujours cru en moi en dépit mes écarts. Malgré ma difficulté à communiquer mes problèmes et à expliquer ma recherche, vous m'avez toujours écouté et compris bien plus que je ne pouvais l'espérer. Un grand merci à ma fratrie, qui m'a offert des weekends qui m'ont permis de m'échapper du travail, que ce soit au grenier ou bien dans le sud.

Ma dernière pensée va à Kenny.

Contents

18F-FDG 2-Deoxy-2-$\left[^{18}F\right]$FluoroGlucose

3DRP Three-Dimensonnal ReProjection

ACF Attenuation Correction Factor

APD Avalanche PhotoDiode

ART Algebraic Reconstruction Technique

BGO Bismuth Germanate

BSREM Block-Sequential Regularised Expectation Maximisation

BV Background Variability

CASToR Customizable and Advanced Software for Tomographic Reconstruction

CCUB Centre de Calcul de l'Université de Bourgogne

CFOV Centre of the Field-Of-View

CGFL Centre Georges-François Leclerc

CRC Contrast Recovery Coefficient

CSR Compton Scatter Recovery

CT Computed Tomography

CTR Coincidence Time Resolution

CTW Coincidence Timing Window

CV Coefficient of Variation

DL Deep Learning

DMI Discovery MI

DOI Depth-Of-Interaction

DSS Double Scatter Simulation

DW Delayed Window

EM Expectation Maximisation

FBP Filtered BackProjection

FDG FluoroDeoxyGlucose

FORE FOurier ReBinning

FOV Field-Of-View

FWHM Full Width at Half Maximum

FWTM Full Width at Tenth Maximum

G-APD Geiger Avalanche PhotoDiode

GATE Geant4 Application for Tomographic Emission

GB GigaByte

GE General Electric

Geant4 GEometry ANd Tracking platform

HDF Hierarchical Data Format

HU Hounsfield Unit

IEC International Electrotechnical Commission

IO Input/Output

IQ Image Quality

IR Image Roughness

keV kiloelectronVolt

LOR Line Of Response

LSO Lutetium oxyorthosilicate

LUT Look-Up-Table

LYSO Lutetium-yttrium oxyorthosilicate

MBSC Model-Based Scatter Correction

MC Monte Carlo

MLEM Maximum Likelihood Expectation Maximisation

MRI Magnetic Resonance Imaging

NDA Non-Disclosure Agreement

NEAT NEMA Analysis Tool

NEC Noise Equivalent Count

NECR Noise Equivalent Count Rate

NEMA National Electrical Manufacturers Association

OSEM Ordered-Subsets Expectation-Maximisation

PE Photo-Electron

PET Positron Emission Tomography

PMT PhotoMultiplier Tube

PSF Point Spread Function

PVE Partial-Volume Effect

QE Quantum Efficiency

RFS Randoms From Singles

ROI Region Of Interest

SART Simultaneous Algebraic Reconstruction Technique

SBR Sphere-to-Background Ratio

SCR Singles-to-Coincidences Ratio

SD Standard Deviation

SEM Standard Error of the Mean

SiPM Silicon PhotoMultiplier

SNR Signal-to-Noise Ratio

SR Single Rate

SSRB Single-Slice ReBinning

SSS Single Scatter Simulation

STIR Software for Tomographic Image Reconstruction

STR Singles Timing Resolution

TOF Time-of-Flight

WCC Well-Counter Calibration

List of Figures

List of Tables

INTRODUCTION

Positron emission tomography (PET) is a medical imaging technique used to measure physiological functions at the molecular level to diagnose disease and monitor response to treatment. This imaging modality plays a crucial role in modern medicine in assessing the functional and biochemical processes of the body's tissues.

PET works by injecting a radioactive tracer, which consists of a biologically active molecule labelled with a radioactive isotope, into the patient. The radiotracers used in PET imaging emit positrons (positively charged particles), and when these positrons collide with electrons present in the body, they undergo annihilation. This annihilation produces two 511 keV gamma rays (photons) emitted in opposite directions, which are detected by PET detectors (scintillation crystals combined with photodetectors) around the patient's body. These detected gamma rays are then used to produce tomographic images showing the spatial distribution of the radiotracer in the patient's body. Depending on the biologically active molecule selected, different physiological functions can be studied.

The use of PET imaging in clinical routine has increased steadily in recent years, and its performance has continued to evolve over time. In recent decades, there has been growing interest in combining a PET scanner with an anatomical imaging system in a single gantry. The first combined PET / computed tomography (CT) system was introduced in 2001 under the name "Discovery LS" (General Electric Healthcare). This innovation marked a significant advance in medical imaging technology by combining the functional imaging capabilities of a PET system with the anatomical imaging of the CT modality. The integration of PET and CT in a single gantry revolutionised the technique by providing both functional and structural information in a single scan, significantly improving the accuracy and efficiency of both diagnosis and treatment in clinical practice.

While PET/CT systems have been commercially available for two decades, the design of a PET scanner combined with a magnetic resonance imaging (MRI) system, an anatomical imaging modality that provides excellent contrast in soft tissues, required another decade of research and development. The main difficulty in producing this dual-modality system was the use of analogue photodetectors, called photomultiplier tubes (PMTs), in earlier PET systems. Although PMTs offered excellent performance (high gain and low noise), they were bulky, expensive, required high voltage and, most importantly, were sensitive to magnetic fields, making them incompatible with MRI.

The avalanche photodiode (APD) was the first magnetic field resistant photodetector proposed to replace PMTs, later improved by the introduction of silicon photomultipliers (SiPMs), based on these APDs. In addition to being magnetic field resistant, they offer gain and temporal resolution comparable to PMTs. As they are also cheaper and less bulky than PMTs, they have become the photodetector of choice for PET imaging systems. In fact, SiPMs are used in most of the latest generation of PET/CT systems, such as the Philips Vereos (Rausch et al., 2019), the GE Discovery MI (Hsu et al., 2017), and the Siemens Biograph Vision 600 (Reddin et al., 2018). Time-of-flight (TOF) imag-

ing, which uses additional information to locate the annihilation events, has also been democratised thanks to the good temporal resolution of SiPMs.

The performance of PET systems is typically evaluated on phantoms using protocols described in the National Electrical Manufacturers Association (NEMA) standard. First published in 1994, the latest version (2018) codifies seven tests used to characterise a PET system. This standard is essential for the comparison and design of PET scanners. PET systems are so complex that it is often difficult for a user (physicist and/or researcher) to study the impact of specific parameters (geometry, detectors, acquisition, and reconstruction parameters) on performance characteristics. Monte Carlo simulations have long been recognised as a valuable alternative to experimental studies for a number of PET imaging applications, including detector design, evaluation of image reconstruction algorithms, correction techniques, dosimetry, and pharmacokinetic modelling (Zaidi, 1999). They also offer greater flexibility than physical phantoms, while requiring fewer resources and expense. Among the Monte Carlo simulators, the Geant4 Application for Tomographic Emission (GATE) is a well-known simulation toolkit. GATE models of several PET systems have already been proposed by the scientific community.

Having a complete model of a PET system and being able to produce clinical-like simulated images could open a vast field of research applications. For example, for our research group, a major interest lies in the fact that a large clinical-like dataset could be generated and used in deep learning applications, such as PET image denoising. In 2017, the Discovery MI 4-ring (GE HealthCare) PET/CT scanner was installed at the Centre Georges-François Leclerc (CGFL). It was the first SiPM-based PET/CT scanner installed in France. The main objective of this thesis was to create a GATE model of this scanner, and to validate the model using the latest NEMA standard. With a clinical-like reconstruction framework of our GATE model, one could generate realistic PET images from simulated data. This work, carried out in collaboration with GE Healthcare, provided a unique opportunity to set up a complete framework in which the reconstruction and correction of data simulated by GATE is managed by the manufacturer's reconstruction tools, similar to those used in a clinical environment.

This manuscript is divided into two main parts, each consisting of several chapters.

Part I provides the theoretical knowledge related to PET imaging. In Chapter 2, the physical concepts behind PET imaging are presented, and the instrumentation related to the detection of annihilation events is detailed in Chapter 3. Chapter 4 then presents the inherent limitations of PET imaging, followed by Chapter 5, which summarises the methods for PET data acquisition and storage. Chapter 6 focuses on the various tomographic reconstruction algorithms commonly used in PET imaging, while Chapter 7 describes the many corrections necessary to obtain quantitative PET images. At the end of Part I, the motivation for this thesis work is developed (Chapter 8).

In Part II of the manuscript, the contributions of this thesis are detailed. Firstly, the performance of the CGFL's DMI4 scanner was evaluated using the manufacturer's tools, in accordance with NEMA standards (Chapter 9). The obtained acquisition data and performance results were then used to develop and validate a home-made NEMA analysis tool (NEAT), independent of the manufacturer's NEMA tools. Chapter 10 focuses on the GATE model of the DMI4 scanner. The framework developed is presented, and the methodology associated with the design of our model is detailed. The validation of the GATE model was carried out by first reproducing the experimental NEMA acquisitions in GATE, and then by comparing the performance of our model with the experimental performance pre-

viously obtained. Finally, Chapter 11 presents the NEMA TOF resolution test, which was added to the latest NEMA standard (2018) after the installation of the DMI4 scanner at the CGFL (2017), and which we successfully applied to a first-generation (Gen1) scanner.

I

POSITRON EMISSION TOMOGRAPHY

2

PET PHYSICS

This chapter provides an overview of the fundamental physics underlying positron emission tomography (PET) imaging. It begins with an introduction to the properties of radiotracers and their interaction with the human body. Radiotracers are the essential agents that make PET imaging possible. Photon interactions with matter in PET imaging are then detailed, shedding light on how gamma photons emitted by radiotracers interact with different tissues and detectors. Finally, the role of Monte Carlo simulations in particle transport is outlined, showing their importance in modelling and optimising PET systems for accurate and informative imaging.

This chapter serves as an essential foundation for understanding the fundamental principles of PET technology.

2.1/ RADIOTRACERS

Radiotracers are generally composed of two parts: a biologically active molecule designed to target a specific metabolic process in the body, and a labelling radioactive isotope, used to locate the radiotracer in the body. Both components of the radiotracer must have specific properties to be suitable for clinical imaging, the most important of which are listed below. The photons emitted by the radioactive isotope should have sufficient energy to escape from the body and allow effective external detection. The radionuclide half-life, i.e. the time required for half of radioactive atoms of a given radionuclide to decay, should be in the range of minutes to hours to facilitate clinical use. Very short physical half-lives would prevent sufficient preparation and injection time, while long effective half-lives (a combination of biological and physical half-lives) would expose the patient to unnecessary radiation. The biologically active molecule must have high specificity for the targeted metabolism and ensure minimal change in its biochemical properties upon incorporation of the radionuclide.

In PET imaging, isotopes must be positron (β^+) emitters. When a β^+ emitter decays (shown in Figure 2.1), a proton in its nucleus is converted into a neutron, resulting in the emission of a positron and an electron neutrino (an electrically neutral particle). The positron, which is the antiparticle of the electron, has the same mass as an electron but carries a positive charge. After being ejected from the nucleus, the positron travels a short distance through matter (typically a few millimetres), gradually losing its kinetic energy in the surrounding tissue. Once most of its energy has been deposited, the positron can combine with an electron present in the matter, resulting in the formation of a short-lived positronium, or less commonly in direct annihilation (Harpen, 2004). The instability of this positronium leads to the annihilation of the electron and positron, converting their masses into energy. The energy released is emitted as two 511 keV annihilation photons in almost exactly opposite directions. The two anti-parallel annihilation photons can be

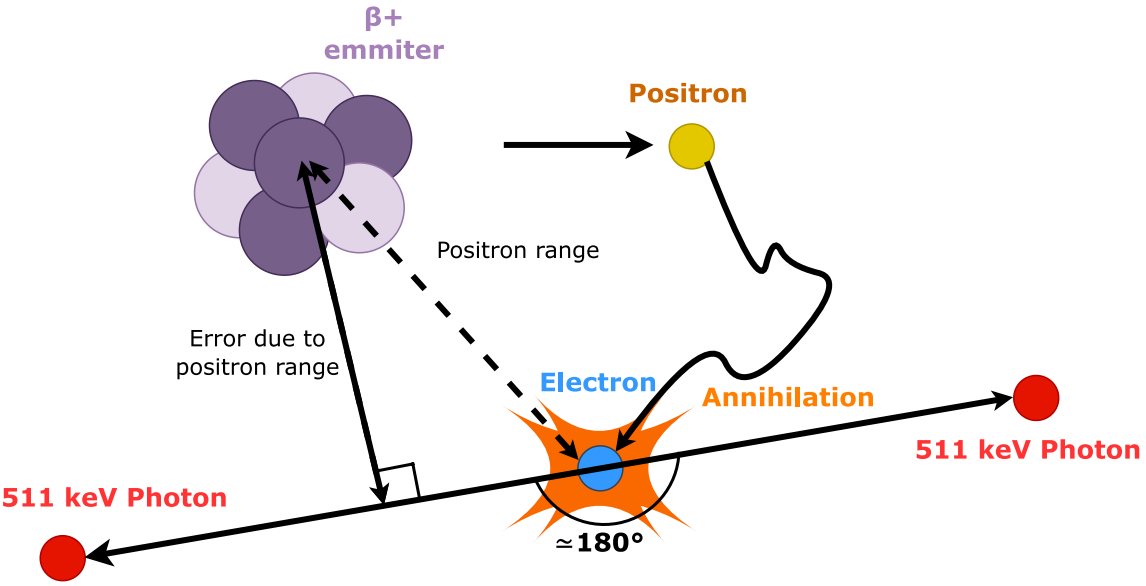

Figure 2.1: After emission, the β^+ particle will travel a short distance before annihilating with an electron of the medium. This annihilation results in the emission of two 511 keV annihilation photons.

used to define a line passing through the annihilation location, called the annihilation line. 2-deoxy-2-$\left[^{18}F\right]$fluoroglucose (18F-FDG) is the most widely used radiotracer in PET imaging because it has all the properties mentioned above. The ^{18}F is the radioactive isotope and the fluorodeoxyglucose (FDG) is the biologically active molecule, which is a glucose analogue. The decay of ^{18}F has a 96.9% chance to undergo β^+ decay (characteristic known as the branching ratio) and the half-life of ^{18}F is 110 minutes, making it suitable for off-site production. Although 18F-FDG enters cells in a similar way to glucose, it cannot be metabolised and is therefore trapped inside the cells. This leads to an accumulation of 18F-FDG proportional to the glucose consumption of the cells. Glucose is used by cells to produce energy and many diseases cause an increase in glucose metabolism. Malignant cells, for example, can be identified on PET images as having a high uptake of 18F-FDG.

2.2/ PHOTON INTERACTIONS WITH MATTER IN PET IMAGING

2.2.1/ PHOTOELECTRIC INTERACTION

The photoelectric effect is a fundamental phenomenon in which an incident photon transfers all of its energy to an atom, resulting in the ejection of an electron, called a photoelectron (PE), and the subsequent disappearance of the incident photon (see Figure 2.2).

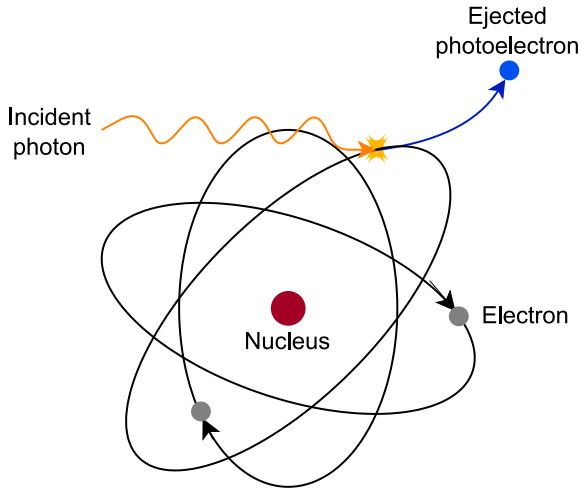

Figure 2.2: Illustration of the photoelectric interaction. The incident photon transfers all its energy to the ejected PE, causing the photon to disappear.

In this process, part of the energy of the incident photon, denoted E_0, is used to overcome the binding energy of an orbital electron within an atom. In the common case where a K-shell electron is ejected, the kinetic energy of the ejected PE, denoted E_{PE}, is determined by:

$$\mathrm{E}_{\mathrm{PE}} = \mathrm{E}_0 - \mathrm{K}_{\mathrm{B}} \tag{2.1}$$

where K_{B} represents the binding energy for an electron on the K-shell.

The probability of photoelectric absorption is influenced by the atomic number (denoted

Z) of the absorbing atom, the binding energy, and the incident photon energy. This probability is often described in terms of the photoelectric cross-section, denoted as σ, which quantifies the probability of the interaction occurring. The probability of photoelectric absorption increases exponentially with Z and decreases rapidly with the energy of the incident photon Dönmez (2017). Photoelectric absorption has a relatively low probability in human tissue at 511 keV. In contrast, high Z elements such as lead, denoted as ^{82}Pb, have a significantly higher photoelectric cross-section, justifying their use as common shielding materials in radiation protection.

2.2.2/ COMPTON SCATTERING

Compton scattering is a fundamental process in which a photon interacts with an orbiting electron in the outer shell of an atom, resulting in the ejection of an electron, called a recoil electron. This interaction causes the incident photon to be deflected from its original path, and some of its energy is transferred to the ejected recoil electron (see Figure 2.3).

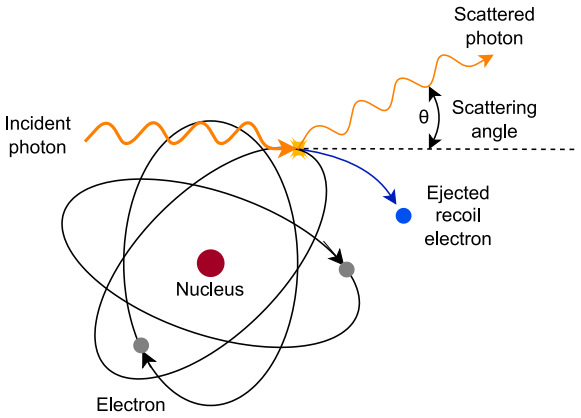

Figure 2.3: Illustration of the Compton interaction, where the incident photon is deflected through a scattering angle θ. Some of its energy is transferred to the ejected recoil electron.

During this interaction, the incident photon changes direction and transfers some of its energy to the recoil electron. The energy of the scattered photon, denoted $\mathrm{E_{sc}}$, is related to the scattering angle, denoted θ, by the Equation (2.2):

$$\mathrm{E_{sc}}(\theta) = \frac{\mathrm{E_0}}{1 + \frac{\mathrm{E_0}}{0.511}(1 - \cos\theta)}, \tag{2.2}$$

where $\mathrm{E_0}$ is the incident photon energy.

At a scattering angle of 180 degrees (backscattering), the energy retained by the scattered photon is minimal ($\mathrm{E_{sc}^{min}} = \mathrm{E_{sc}}(180)$) and the energy transferred to the recoil electron is maximal ($\mathrm{E_{re}^{max}} = \mathrm{E_0} - \mathrm{E_{sc}^{min}}$). Conversely, when the scattering angle is close to 0 degrees, the scattered photon is only slightly deflected and retains almost all of its initial energy. The probability of Compton interactions decreases with increasing energy. It also depends mainly on the number of electrons available in the atom and is therefore less dependent on Z than the photoelectric interaction Dönmez (2017). For β^+ particles (i.e. 511 keV annihilation photons), the corresponding values for $\mathrm{E_{sc}^{min}}$ and $\mathrm{E_{re}^{max}}$ are 170 keV and 341 keV, respectively, illustrating the conservation of the initial energy $\mathrm{E_0} = 511$ keV.

2.3/ MONTE CARLO SIMULATIONS FOR PARTICLE TRANSPORT

Monte Carlo (MC) methods are computational algorithms based on the repeated sampling of random variables. In the context of particle transport simulations, the modelled system is typically represented as a three-dimensional lattice or geometry, consisting of different materials with distinct properties. These simulations involve the random sampling of initial particle conditions, including their positions, energies, and directions, followed by the tracking of their interactions and motions as they traverse the system. By tracking particles individually and recording their trajectories, MC simulations provide comprehensive insights into particle interactions and transport within complex systems.

When a particle is emitted, its initial position, energy, and direction are determined by the characteristics of the source. The particle is then tracked step by step through the system as it interacts with materials and undergoes various physical processes.

MC simulations use probability density functions derived from established physical models to calculate the probability of different types of interaction occurring, and thus to determine the distance the particle will travel before its next interaction. Once the distance is determined, the particle's position is updated accordingly. If the particle undergoes an interaction, calculations are performed to account for changes in its properties, such as energy or direction.

The tracking process continues until one of the following conditions is met: the particle leaves the system, loses enough energy to stop, or reaches a predefined termination condition. Throughout the simulation, data is recorded on the properties of the particle, its trajectory, interactions, and potential generation of secondary particles.

Several Monte Carlo simulators are available for emission tomography imaging, each with unique features and applications. SimSET (Simulation System for Emission Tomography) is specialised for PET and SPECT, providing tools for photon transport and detector interactions, along with predefined scanner models and phantoms, and support for user-defined geometries. PeneloPET (España et al., 2009) offers high accuracy in simulating electromagnetic interactions, realistic detector responses, and tools for defining complex geometries. MCNP (Monte Carlo N-Particle, Rising et al. (2023)) is a general-purpose code capable of simulating neutron, photon, electron, and ion transport, known for its versatility and detailed physics models.

Finally, the most notable MC simulator is GEometry ANd Tracking platform (Geant4) (Agostinelli et al., 2003). Geant4 uses a combination of the composition and rejection Monte Carlo methods. The composition method is used when the cumulative distribution function of the variable to be sampled can be expressed as a mixture of cumulative distribution functions. If this approach is not applicable, the acceptance-rejection method can be used. In this method, samples are drawn in a higher dimensional space until they fall within the density function of the initial variable.

Originally released in 1998 by the Geant4 collaboration (Agostinelli et al., 2003), Geant4 has evolved over time, with the latest stable version released in February 2023. This versatile toolkit enables the simulation of particle transport in a wide range of fields, including high-energy physics, space and radiation science, and medical physics. In particular, it has become a standard MC simulation tool in the field of nuclear medicine (Zaidi, 1999; Buvat et al., 2002).

3

INSTRUMENTATION

This chapter describes the essential components and technologies that constitute a PET imaging system. A comprehensive review of the instrumentation required for PET imaging is given, and its role in producing high quality images is outlined. PET instrumentation covers various aspects including scintillation crystals, photodetectors, block detectors, event detection, and the central concept of time-of-flight (TOF) technology. By summarising the intricacies of PET instrumentation, this chapter provides the reader with an understanding of the technological fundamentals that enable clinical and research applications of PET imaging.

3.1/ SCINTILLATION CRYSTALS

Materials capable of emitting light upon energy deposition are known as scintillators. In these materials, radiation causes ionisation and/or excitation of atoms and molecules, resulting in the release of energy. This energy can be released as thermal energy, visible light, or ultraviolet light.

In nuclear imaging, inorganic scintillators are the most commonly used scintillators. The scintillation mechanism of these materials is achieved by the particular structure of the crystal lattice. Dense scintillation crystals are typically used for PET detection to efficiently convert the 511 keV photons produced during the annihilation process into visible light. In a PET system, the crystals are generally arranged in detector blocks which are placed in a ring geometry around the object to be imaged (see Section 3.3). The geometry of a PET scanner plays a crucial role in the performance characteristics of the system (see Chapter 3) and in its ability to distinguish and accurately represent small details or structures in the imaged object, a property known as spatial resolution.

To maximise the cross-section of the photoelectric effect, PET scintillators are chosen to have a high Z number. The higher the cross-section of the photoelectric effect, the better the detection of the 511 keV γ photons, allowing the use of thinner crystals.

PET scintillators are also chosen for their ability to rapidly emit a large number of visible photons. A large number of photons is required to reduce the statistical uncertainties in the final detected signal, with a higher light yield leading to improved temporal and spatial resolution. The rate of light emission is referred to as the scintillation decay time, which has a significant effect on the ability of the system to precisely timestamp detected events, property known as temporal resolution (see Chapter 9).

Another key feature of scintillators is the proportionality between the amount of light produced and the energy deposited in the crystal by the incident photon. This proportionality allows the incident photons to be selected and sorted according to their energy.

In early PET systems, inorganic scintillator crystals were commonly made from bismuth germanate (BGO), known for its excellent intrinsic detection efficiency for 511 keV photons, which is the fraction of radiation that interacts within the detector as it passes through. In modern PET systems, lutetium oxyorthosilicate (LSO) is a popular choice, offering a slightly lower intrinsic detection efficiency compared to BGO, but a higher photon yield and faster decay. Lutetium-yttrium oxyorthosilicate (LYSO) crystals, which contain yttrium in place of some lutetium atoms, are often preferred to LSO due to their lower production cost.

3.2/ PHOTODETECTORS

3.2.1/ PHOTOMULTIPLIER TUBES

Photomultiplier tubes (PMTs) consist of a number of components which convert the weak light emitted by the scintillation crystals into an electrical signal (see Figure 3.1). The input of a PMT, called the photocathode, is coated with a photoemissive substance that releases PEs when exposed to light. Typically, one to three PEs are released for every ten photonic hits on the photocathode (Cherry et al., 2012). The ratio of the number of PEs

released to the number of incident light photons is called the quantum efficiency (QE). This property is a critical factor in the performance of the photodetector. A high QE ensures that the scintillation light produced by γ interactions in the scintillation crystal is efficiently converted into PEs. This results in a more intense electrical signal, minimising statistical fluctuations in the measurement of the spatial and energetic signal.

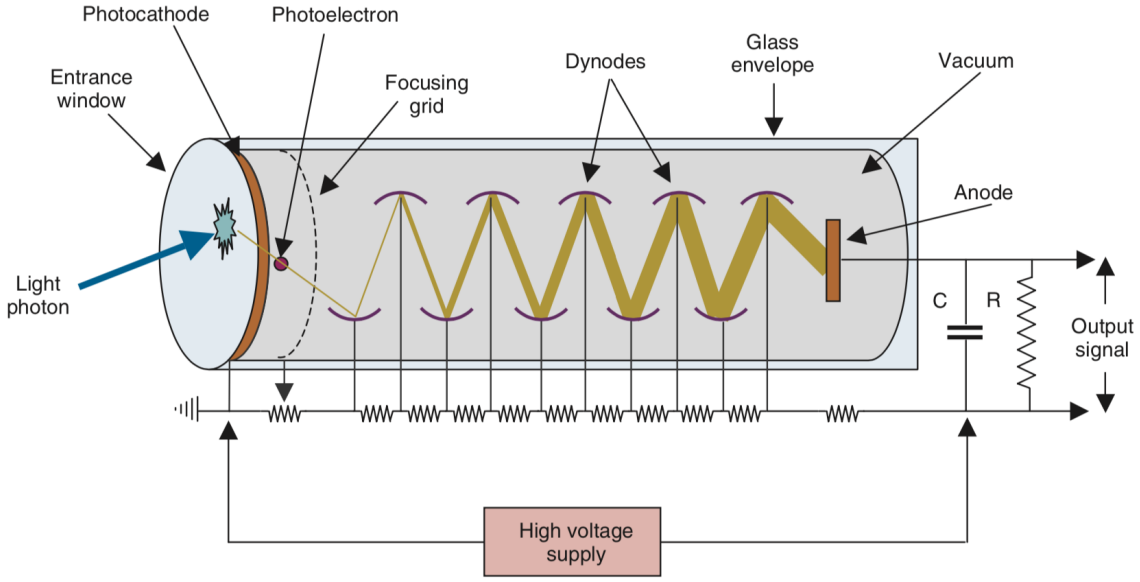

Figure 3.1: Cross-sectional view of a photomultiplier tube (Cherry et al., 2012).

Next to the photocathode are the dynodes (see Figure 3.1), which are metal plates held at a positive potential. To guide the PEs released by the photocathode efficiently to the dynodes, a focusing grid is used. When a PE reaches a dynode, secondary electrons are ejected and some of these secondary electrons are directed to the next dynode. This initiates a multiplication process: each dynode provides a multiplication factor of approximately three to six, resulting in a significant amplification of the initial signal. At the anode (last dynode), the resulting amplification of the electrons exceeds one million, producing a sharp current pulse.

PMTs require high voltages, typically around 1300 volts and more. Voltage stability is essential to maintain consistent multiplication factors and stable signal amplification. For example, a 1% increase in voltage will result in a 10% increase in the current collected at the anode (Cherry et al., 2012). PMTs are also susceptible to external electromagnetic fields, which can introduce unwanted noise and interference. This susceptibility to external electromagnetic fields makes PMTs unsuitable for hybrid PET/magnetic resonance imaging (MRI) systems, where strict electromagnetic compatibility is required.

3.2.2/ SILICON PHOTOMULTIPLIERS

Silicon-based solid-state photodetectors, often referred to as photodiodes, can be used as an alternative to traditional PMTs. They offer several advantages, particularly in the context of PET imaging.

When light photons from the scintillator reach a silicon photodetector, they carry enough energy to create electron-hole pairs within the silicon material. By applying an electric

field to the photodetector, the generated electrons move to one side of the diode, while the holes move to the other side, resulting in an electric current. This current is measured by electrodes positioned at each end of the photodiode and is proportional to the energy deposited in the detector.

The main advantages of silicon-based photodetectors are their high QE (>60% vs 10-30% for PMTs) and their ability to withstand significant magnetic fields (sufficient for PET/MRI applications). However, they have a lower internal gain than PMTs, resulting in a lower signal-to-noise ratio (SNR) than PMTs.

To address this shortcoming, alternative silicon-based photodetectors have been developed. The PIN diode offers a higher QE and improved ability to accurately timestamp events (temporal resolution), but lacks intrinsic gain. The avalanche photodiode (APD) uses a strong internal electric field to produce an avalanche of electrons when photons interact, resulting in increased gain (up to three orders of magnitude) and excellent QE (around 90%). However, its gain and temporal resolution remain inferior to that of PMTs.

APDs can be operated in Geiger mode (geiger avalanche photodiode (G-APD)) by applying an even higher voltage to further amplify the electron avalanche, resulting in a substantial gain increase comparable to that of PMTs. However, a major drawback is the constant amplitude of the resulting signal, regardless of the nature or energy of the incident particles. This leads to a loss of proportionality between the signal current and the number of incident photons.

This limitation has been overcome with the introduction of silicon photomultipliers (SiPMs). SiPMs consist of arrays of G-APD cells connected in parallel across a surface, typically from one to a few mm^2. The output signal of a SiPM is the sum of all signals emitted by the individual G-APDs cells, ensuring proportionality to the number of activated G-APD cells. This proportionality is maintained as long as the number of incident light photons is less than the number of G-APDs cells on a given SiPM.

SiPMs offer a lower QE than APDs, but better than PMTs, are resistant to magnetic fields, and provide gain and temporal resolution comparable to PMTs. They also operate at lower voltages, eliminating the need for high-voltage power supplies. However, the gain provided by SiPMs is subject to temperature variations. Therefore, stabilisation systems are required, either to maintain temperature consistency or to adjust the applied voltage in response to temperature changes.

SiPMs have become the photodetectors of choice for PET imaging systems. They combine the advantages of magnetic field resistance, high QE and gain, making them well suited for the demands of modern PET. SiPMs are used in most of the latest generation of clinical PET systems, such as the Philips Vereos (Rausch et al., 2019), the GE Discovery MI (Hsu et al., 2017), and the Siemens Biograph Vision 600 (Reddin et al., 2018).

3.3/ BLOCK DETECTORS

In a PET system, the transfer of information between the scintillation material and the photodetectors (PMT or SiPM) plays a vital role in the instrumentation chain.

In clinical PET imaging, the scintillation material is often organised into a crystal array. This arrangement is achieved by making partial cuts through a larger piece of scintillator,

resulting in an array of multiple crystal elements, commonly referred to as pixels. In addition, the spaces or cuts between these elements may be filled with a reflective material to reduce cross-talk, which is the unintentional sharing of scintillation light between adjacent scintillator elements.

Ideally, a one-to-one (1:1) coupling, where each pixel is connected to a dedicated photodetector, would be the most efficient coupling logic. In such a setup, the pixel size would define the spatial resolution of the system, allowing each detected event to be localised to a single pixel. This could also simplify the identification of scattered events. However, practical limitations associated with the first PMTs used, in particular their size and cost, have led to the adoption of different coupling strategies.

The block detector concept proposed by Casey et al. (1986) offers an alternative solution. In this initial design, a larger number of scintillation crystals are coupled to a reduced number of photodetectors. Figure 3.2 illustrates the block detector structure using four photodetectors (PMTs or SiPMs).

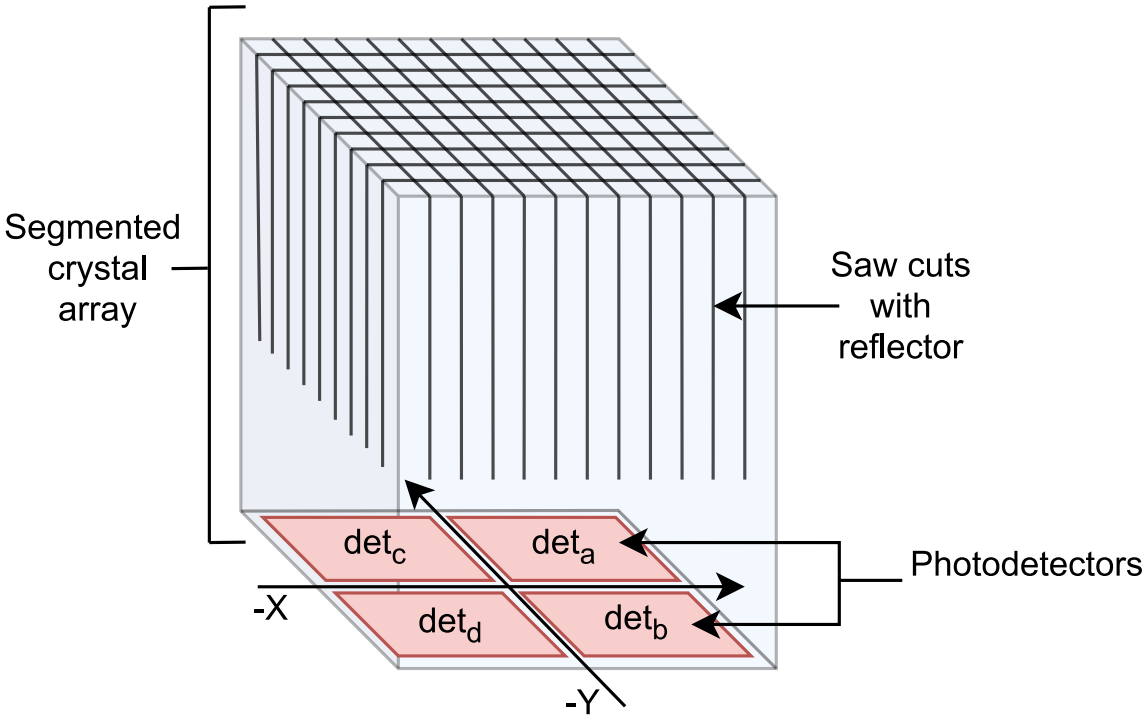

Figure 3.2: Illustration of the structure of a block detector. The scintillation material is cut into small crystal pixels. The light produced is read by four individual photodetectors.

This configuration results in optical multiplexing, where the light produced by the crystal array is detected and split between the photodetectors. The position of an interaction within the crystal block is calculated using the centroid of the detected information, weighted by the amount of light collected by each photodetector. For a block of N photodetectors at known locations $(\mathrm{x_i}, \mathrm{y_i})$, interaction position estimates are given by the Anger algorithm:

$$\begin{cases} \hat{x} & = \frac{\sum_{i=1}^{N} x_i S_i}{\sum_{i=1}^{N} S_i} \\ \\ \hat{y} & = \frac{\sum_{i=1}^{N} y_i S_i}{\sum_{i=1}^{N} S_i} \end{cases} \tag{3.1}$$

where S_i is the signal collected by each photodetector i.

In the latest generation of SiPMs-based PET systems, often referred to as digital PET, the size of the photodetector is no longer a limiting factor, and some commercially available clinical PET systems such as the Phillips Vereos propose a (1:1) coupling between crystals and SiPMs. However, a (1:1) coupling introduces technical challenges due to the large number of SiPM devices, resulting in a large number of output channels. Various signal multiplexing methods have been proposed to overome this problem (Park et al., 2022), and some digital PETs still use a multiplexing logic applied to SiPMs (Siemens, GEHC).

3.4/ EVENT DETECTION

When a photon interacts within the scintillation crystals and is detected by a photodetector, the electronics of that detector generate a pulse. This pulse undergoes energy discrimination to:

- discard photons that have lost some energy due to Compton scattering;
- discard high-energy photons that have been emitted by non-pure isotopes;
- limit the situation where two photons interact in close temporal proximity within the same detector and are integrated into a single pulse, a phenomenon called ”pile-up” (see Section 4.3.2)

The pulses remaining after energy discrimination are called single events.

As previously mentioned, annihilation photons are emitted simultaneously and in nearly opposite directions. Therefore, the near-simultaneous detection of two photons can indicate that an annihilation has occurred somewhere along the line connecting the two detectors, called the LOR. To exploit this temporal property, each single event is assigned a timestamp based on its detection time. If the difference between the timestamps of two single events is less than a threshold value, denoted τ, they are paired to form a coincidence event. In other words, a single event S_1 detected at a time T_1 can be paired into a coincidence with any other single event detected between $T_1 - \tau$ and $T_1 + \tau$. This time interval is known as the coincidence timing window (CTW), and its width is $T_1 + \tau - (T_1 - \tau) = 2\tau$. The resulting coincidence events are then associated with the LOR defined by the two detectors that recorded the respective single events.

This coincidence pairing process can be performed post-acquisition using all timestamped single events (see Section 5.2.1) or directly during acquisition in the system electronics using a coincidence unit (see Figure 3.3).

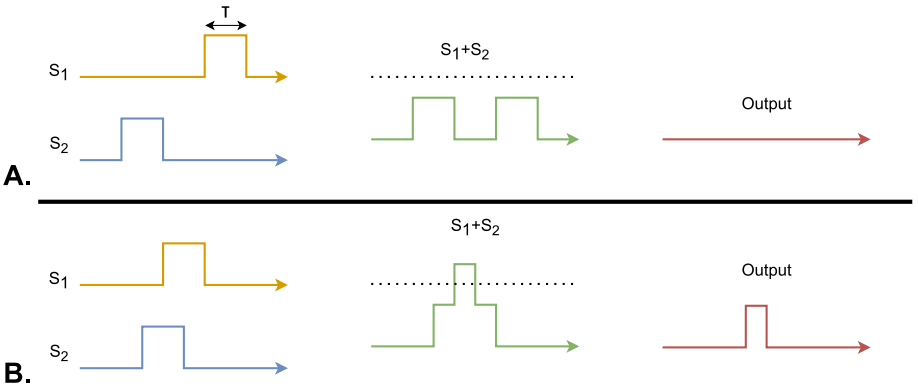

Figure 3.3: Illustration of the coincidence pairing of two different single events S_1 and S_2 using a coincidence unit. Each event generates a pulse of width τ when detected. **A.** As the two events are separated in time by more than one τ, there is no overlap between their pulses: their addition does not produce a sufficient signal on the output channel. **B.** The two pulses partially overlap, producing a signal in the output channel: this signal is used to form a coincidence event using the two pulses.

Ideally, this coincidence pairing process should produce coincidences where the two single events are the result of the detection of two photons coming from the same annihilation. Furthermore, the LOR used to characterise a coincidence event should overlap with the annihilation line. In such an ideal case, a coincidence is called a true coincidence (see Figure 3.4(a)), since the LOR associated with a true coincidence is aligned with the actual annihilation line. True coincidences are the only useful signals detected by PET systems. Unfortunately, several processes can prevent the detection of photons originating from the same annihilation event (See Chapter 4), resulting in ”untrue” coincidences that provide unwanted information.

If one or both of the detected photons from the same annihilation undergo Compton scattering, a so-called scatter coincidence can be formed during the pairing process (see Figure 3.4(b)). In such cases, at least one photon deviates from its initial emission direction. Although both photons come from the same annihilation, the change in direction introduces a misalignment of the LOR with respect to the actual annihilation line, leading to an inaccurate estimate of the annihilation location (See Section 4.1.4).

In situations where two single events from different annihilations are detected and paired within the same CTW, a so-called random coincidence occurs (see Figure 3.4(c)). Since the two photons detected are not from the same annihilation, random coincidences do not represent an annihilation event and contribute to the noise in the recorded coincidences. Although the formation of random coincidences cannot be completely avoided, correction methods have been developed (see Section 7.4).

Finally, as the radioactive activity increases, several single events may be recorded within the same CTW, resulting in multiple coincidence pairs (see Figure 3.4(d)). Depending on the design of the coincidence processor, multiple coincidences can be either retained or rejected on the basis of different criteria.

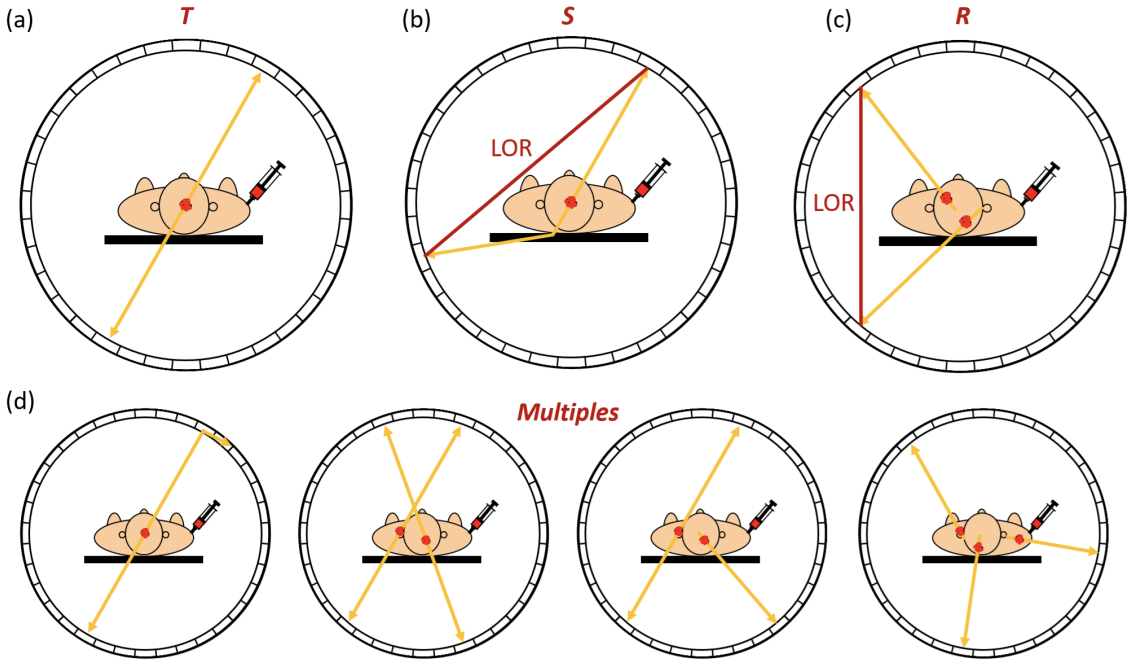

Figure 3.4: Illustration of the different types of coincidences detected by a PET system: (a) true coincidence, (b) scatter coincidence, (c) random coincidence and (d) multiple coincidences.

3.5/ TIME-OF-FLIGHT INFORMATION

One of the most notable developments in recent PET systems is the introduction of TOF technology. Consider a coincidence event C consisting of two single events, S1 and S2, recorded at times T_1 and T_2, respectively. The time difference Δt between these events is related to the distances D_1 and D_2 travelled by S1 and S2, as shown in Figure 3.5, by the equation:

$$\Delta t = T_2 - T_1 = \frac{|D_2 - D_1|}{c}, \tag{3.2}$$

where c is the velocity of light (3×10^{10} cm.sec^{-1}).

The distances D_1 and D_2 can be used to calculate Δd, the distance between the location of the annihilation and the centre of the LOR as follows:

$$\Delta d = \frac{|D_2 - D_1|}{2} \tag{3.3}$$

By substituting $|D_2 - D_1|$ with $\Delta t \times c$ (according to Equation 3.2) in Equation 3.3, the relationship between distance and time differences becomes:

$$\Delta d = \frac{\Delta t \times c}{2} \tag{3.4}$$

In theory, with perfect measurements of T_1 and T_2, the estimation of Δd would allow the accurate localisation of the annihilation event along the LOR, eliminating the need for

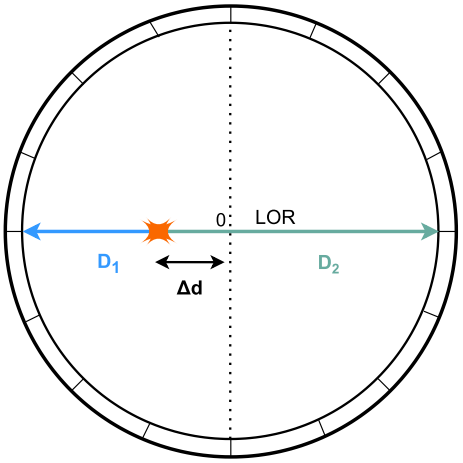

Figure 3.5: Illustration of distances in a PET system to calculate Δd using TOF information. The recording time difference between two events and the speed of light can be used to calculate the size of D_1 and D_2.

image reconstruction. However, the temporal information associated with each coincidence is subject to uncertainties introduced by the temporal resolution of each detector, called the singles timing resolution (STR). This uncertainty affects the estimate of Δd. For coincidences, the term coincidence time resolution (CTR) is used. Assuming Gaussian statistics, the CTR is related to the STR as follows:

$$\mathrm{STR} = \sqrt{2}/\mathrm{CTR} \tag{3.5}$$

For a system such as the Discovery MI 4-ring with a CTR of 375 ps, the resulting spatial uncertainty would be 5.6 cm. This level of uncertainty does not allow PET images to be produced from TOF information alone. However, TOF data can be used as additional information for iterative reconstruction methods (see Section 6).

4

LIMITATIONS INHERENT TO PET SYSTEMS

In this chapter, the inherent limitations and biases that affect the performance and accuracy of PET imaging systems are discussed. They are divided into three main groups. Physics-induced biases are factors related to the physics of positron emission and the interaction of emitted photons with matter in the human body. These factors include positron range, non-collinearity of annihilation photons, gamma ray attenuation, and Compton scattering. Instrumentation biases are induced by the design and properties of PET system components, such as scintillation crystals and detectors. In this section, crystal dimensions, crystal scattering, depth-of-interaction (DOI) effects, and the arc effect are discussed. Finally, detection systems are subject to dead time and pile-up, which can lead to count rate limitations and non-linear count rate behaviour. Understanding these limitations is essential as it guides the development of correction techniques and optimisation strategies.

4.1/ PHYSICS INDUCED BIAS

4.1.1/ POSITRON RANGE

As discussed in Section 2.1, a positron emitted during the decay of β^+ emitters travels a short distance before annihilating with an electron from the surrounding tissue. This distance, known as the positron range, is the distance from the positron emission to the positron annihilation, as shown in Figure 2.1. The extent of the positron range depends on the energy of the emitted positron, which is specific to the isotope being used. The point spread function of the positron range has a characteristic 'cusp-like' shape (Levin et al., 1999). The positron range in soft tissue is typically of the order of millimetres, with ^{18}F having a positron range of approximately 0.6 millimetres (Conti et al., 2016).

Because of this positron range, the LOR is misplaced a few millimetres away from the actual location of the β^+ emission. Since the annihilation line is used to estimate the position of the radiotracer, the positron range introduces an error in the location of the initial β^+ decay event. This in turn degrades the spatial resolution and causes blurring in the resulting PET image.

4.1.2/ NON-COLLINEARITY

During the annihilation process, the positron (or positronium) may have a non-zero kinetic energy. As a result, the two annihilation photons produced are not emitted at a perfect angle of 180 degrees, but instead show a small angular spread, as depicted in Figure 4.1. This phenomenon is known as non-collinearity, and the angular distribution follows a Gaussian shape with a full width at half maximum (FWHM) of about $\sim 0.6°$ (Cherry et al., 2012).

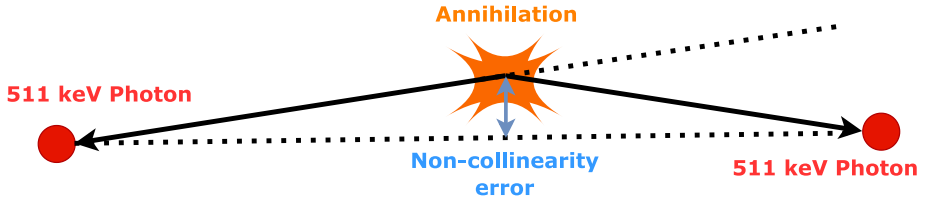

Figure 4.1: Illustration of the mismatch between LOR and annihilation line caused by the non-collinearity of two annihilation photons.

Non-collinearity introduces a misplacement of the LOR with respect to the annihilation position. This effect is independent of the initial positron energy but is directly proportional to the radius R of the PET ring. It induces a Gaussian blurring of the spatial resolution (expressed in FWHM) given by 0.0044R. Consequently, photon non-collinearity has a significant impact on the spatial resolution of clinical PET systems.

4.1.3/ ATTENUATION

Attenuation refers to the loss of detected events caused by the presence of a dense medium within the object, resulting from either photoelectric interactions or scattering processes. Consequently, a LOR passing through a significant amount of attenuating

material will underestimate the amount of activity along that LOR, introducing a quantification bias in the final PET image.

The attenuation induced by each material can be characterised by a linear attenuation coefficient μ, which quantifies the probability that a photon of a given energy will interact with a given material as it passes through it. This coefficient is expressed in terms of probability per unit distance (see Section 2.2). For PET, where the primary interactions are the photoelectric effect and Compton scattering, the linear attenuation coefficient of a material can be considered as the sum of these two interaction coefficients:

$$\mu \simeq \mu_{\text{photoelectric}} + \mu_{\text{Compton}} \tag{4.1}$$

Let $\mathrm{I}(0)$ be the initial intensity of monoenergetic photons emitted along a given LOR without attenuation. Let d be the thickness of the absorber causing attenuation along this LOR. In a narrow geometry (no scattering detected), the intensity $\mathrm{I}(x)$ ($x \in [0, \mathrm{d}]$) of the beam transmitted through the thickness d of linear attenuation coefficient μ along the LOR is described by the attenuation formula:

$$\mathrm{I}(x) = \mathrm{I}_0.e^{-\mu x}, x \in [0, \mathrm{d}] \tag{4.2}$$

4.1.4/ COMPTON SCATTERING

Photons undergoing Compton scattering are subject to changes in trajectory and energy, as described by Equation 2.2. These changes in trajectory lead to incorrect positioning of the LOR (see Figure 3.4b).

4.2/ INSTRUMENTATION INDUCED BIASES

4.2.1/ CRYSTAL DIMENSIONS

Scintillation crystals play a key role in PET scanner detection systems. Their properties, including cross-section and thickness, are carefully selected to optimise various system performance metrics. Crystal cross-section is the primary factor influencing the spatial resolution of PET systems. Small crystals offer more accurate positioning of detected events (assuming perfect detection electronics) (Cherry et al., 2012), while thicker crystals offer better intrinsic detection efficiency. Clinical PET systems comprising BGO, LSO, or LYSO scintillators typically use crystals two to three centimetres thick (Cherry et al., 2012).

4.2.2/ CRYSTAL SCATTERING

Scintillator materials used in PET detectors, such as BGO, LSO, and LYSO, exhibit a photofraction of less than 45% for 511 keV gamma rays (Zhang et al., 2019b). Consequently, there is a high probability of Compton scattering. If scattering occurs within the crystal, the photon may lose energy and either undergo further Compton scattering or be

absorbed via the photoelectric effect. When considering coincidences, it is highly probable that at least one of the photons will undergo inter-crystal scattering (Zhang et al., 2019b). Crystal scattering results in the misalignment of the LOR, leading to reduced spatial resolution when detected. It can also cause a loss of sensitivity (percentage of detected events over the number of emitted events) if it is deflected outside the detection system.

4.2.3/ DEPTH-OF-INTERACTION

In PET systems with standard architecture (see Section 3.3), it is impossible to determine the depth of photon interaction within the crystal. Therefore, the position associated with a detected event in a crystal is recorded as occurring either at the front or at the centre of the crystal, leading to the DOI effect, also known as the parallax effect. For annihilation lines passing through the centre of the field-of-view (FOV), this lack of depth information is not problematic because the associated LORs are orthogonal to the detector surface. However, for incoming photons at a non-orthogonal angle to the crystal surface, the DOI effect leads to a discrepancy between the LOR recorded by the system and the actual annihilation line, as shown in Figure 4.2. This effect reduces the spatial resolution along the radial direction. It becomes more pronounced as both radial distance and crystal thickness increase.

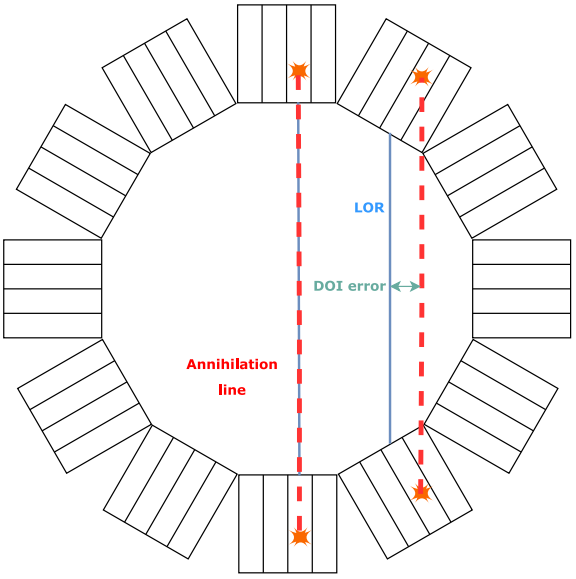

Figure 4.2: Illustration of the DOI effect, where the misalignment (in green) of the LOR (in blue) with respect to the annihilation line (in red) becomes more important with increasing radial offset.

4.2.4/ ARC EFFECT

The arc effect is named after the curved nature of the detector ring and describes the uneven spacing of parallel LORs. LORs passing near the centre of the FOV are more widely spaced than those at the extremities, as shown in Figure 4.3. This effect leads to non-uniform sampling of the data along the radial axis (see Section 5.2.2).

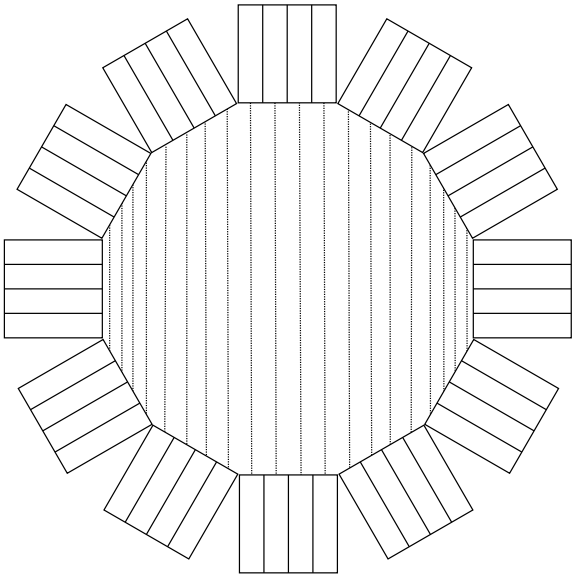

Figure 4.3: Illustration of the arc effect, where the distance between parallel LORs decreases as the radial distance increases.

4.3/ DETECTION INDUCED BIASES

4.3.1/ DEAD TIME

The electronic processing of the photons detected by the scintillation crystals is fast, but not instantaneous. The time required to process an event is called dead time and is often denoted τ. At very high count rates, there is a high probability that more one count will occur per dead time interval of an electronic block. This make it impossible to process all the events detected, and results in an observed count rate lower than the true count rate. Therefore, the count rate capability of PET systems as a function of the activity is not linear.

Mathematically, the dead time of a component can be modelled according to two different behaviours: paralysable and non-paralysable. Let X be a detected event that generates an arbitrary dead time. Let Y be a second event that occurs during the dead time induced by X, and that is therefore not detected by the system. If Y is ignored with no effect on the electronics' dead time, the system is said to be non-paralysable. In the opposite case, if Y is not counted but still triggers a dead time, the system is said to be paralysable. According to these definitions, non-paralysable systems have a fixed dead time between each observable event, leading to a plateau in the observed count rate at very high activities. Conversely, a paralysable system will be unable to accept events as long as there is more than one event per dead time interval, leading to losses in the observed count rate at very high activities (see figure 4.4).

The system dead time is the combination of all the dead times of its components. Different components of a system may be represented by one model or the other. The global dead time of the system is therefore a mixture of both models. If a particular component has a significantly long dead time compared to others, then the system dead time can be determined (and modelled) by the dead time of that component.

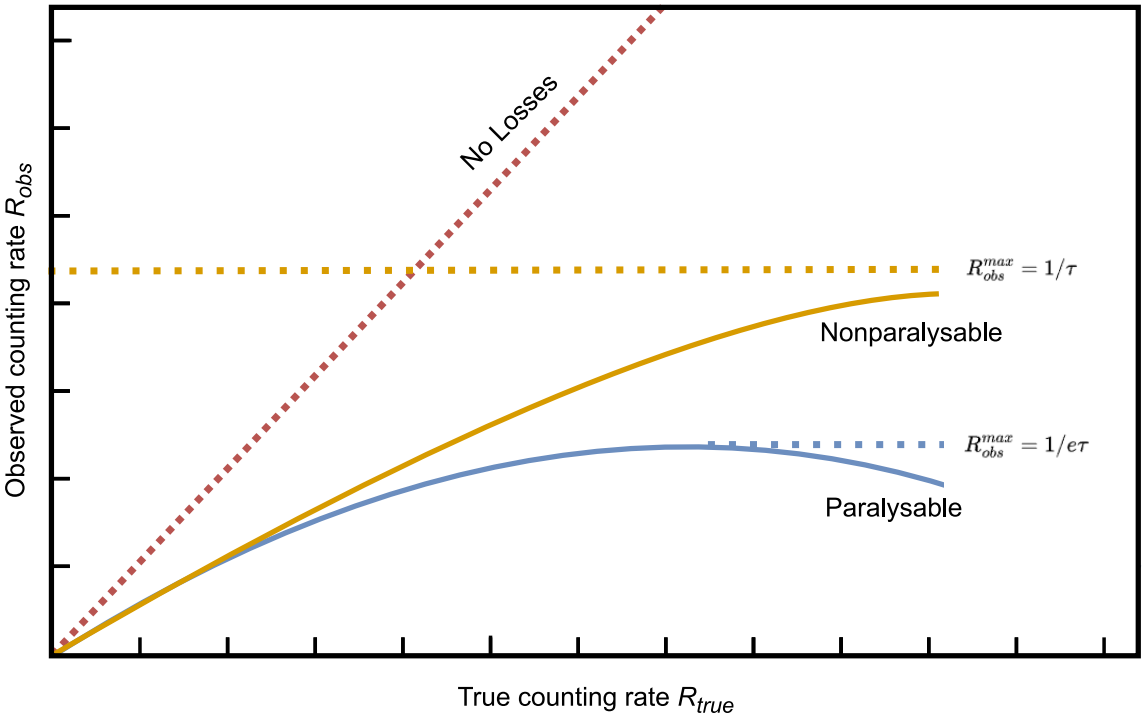

Figure 4.4: Illustration of the non-paralysable and paralysable dead time models for two systems with the same value of τ.

The effects of a dead time τ on the observed count rates $\mathrm{R_{obs}}$ with respect to the true count rates $\mathrm{R_{true}}$ can be modelled by Equation 4.3 for a paralysable system and by Equation 4.4 for a non-paralysable system.

$$\mathrm{R_{obs}} = \mathrm{R_{true}}.e^{-\mathrm{R_{true}}.\tau} \tag{4.3}$$

and

$$\mathrm{R_{obs}} = \frac{\mathrm{R_{true}}}{1 + \mathrm{R_{true}}.\tau} \tag{4.4}$$

For a paralysable system, $\mathrm{R_{obs}^{max}}$ is given by:

$$\mathrm{R_{obs}^{max}} = 1/e\tau \tag{4.5}$$

In the case of a non-paralysable system, the observed count rate value of the plateau, denoted $\mathrm{R_{obs}^{max}}$, is given by:

$$\mathrm{R_{obs}^{max}} = 1/\tau \tag{4.6}$$

4.3.2/ PILE-UP

Pile-up is a special case of dead time, where the integration time of a single photon is longer than the time separating the arrival of two photons. Pile-up occurs when the energy

of two photons is integrated into a single energy, resulting in a single pulse (Cherry et al., 2012).

On the one hand, the recorded piled-up energy may be higher than the upper threshold of the energy discrimination. In this case, the event is simply rejected, resulting in the loss of two detected photons and lowering the count rate. On the other hand, if at least one of the piled-up photons has undergone Compton scattering, the total piled-up energy may still be accepted by the energy discrimination process. In such a case, only one event is recorded with incorrect energy, spatial, and temporal information, causing artefacts in the image.

5

DATA ACQUISITION

This chapter discusses aspects of data acquisition in PET imaging in order to lay the groundwork for the subsequent chapters on reconstruction techniques and corrections. Data acquisition is fundamental to the ability of any PET system to provide information on the distribution of radiotracers within the human body. The different acquisition modes, such as 2D and 3D acquisition, are presented, each with its advantages and limitations. The methods used to store the acquired data are also described, namely the standard PET sinogram and the versatile list-mode format.

5.1/ 2D AND 3D ACQUISITION MODES

In the early days of multi-ring PET systems, axial collimators (or septas) were used to separate the rings of the tomograph. Coincidences orthogonal to the axis of the PET system were kept to form direct planes (see Figure 5.1A). This orthogonality ensures that both photons of a given coincidence are detected in the same detector ring. In addition, cross planes could be formed, using the coincidences recorded between adjacent detector rings (see Figure 5.1B).

The sole use of direct and cross planes is referred to as two-dimensional (2D) acquisition, as only parallel planes are used. In a system with $\mathrm{N} = 36$ detector rings, such as the DMI 4-ring (4×9 rings), 36 direct and 35 $(\mathrm{N} - 1)$ cross planes are defined, for a total of 71 $(2\mathrm{N} - 1)$ coincidence planes.

The use of septa provides an efficient rejection of photons scattered in the body and helps to reduce the number of random coincidences. In a 2D acquisition mode, the acquired planes can be reconstructed using 2D filtered backprojection (FBP) to obtain contiguous 2D transaxial image planes, which are stacked to obtain a single image volume (see Section 6.1).

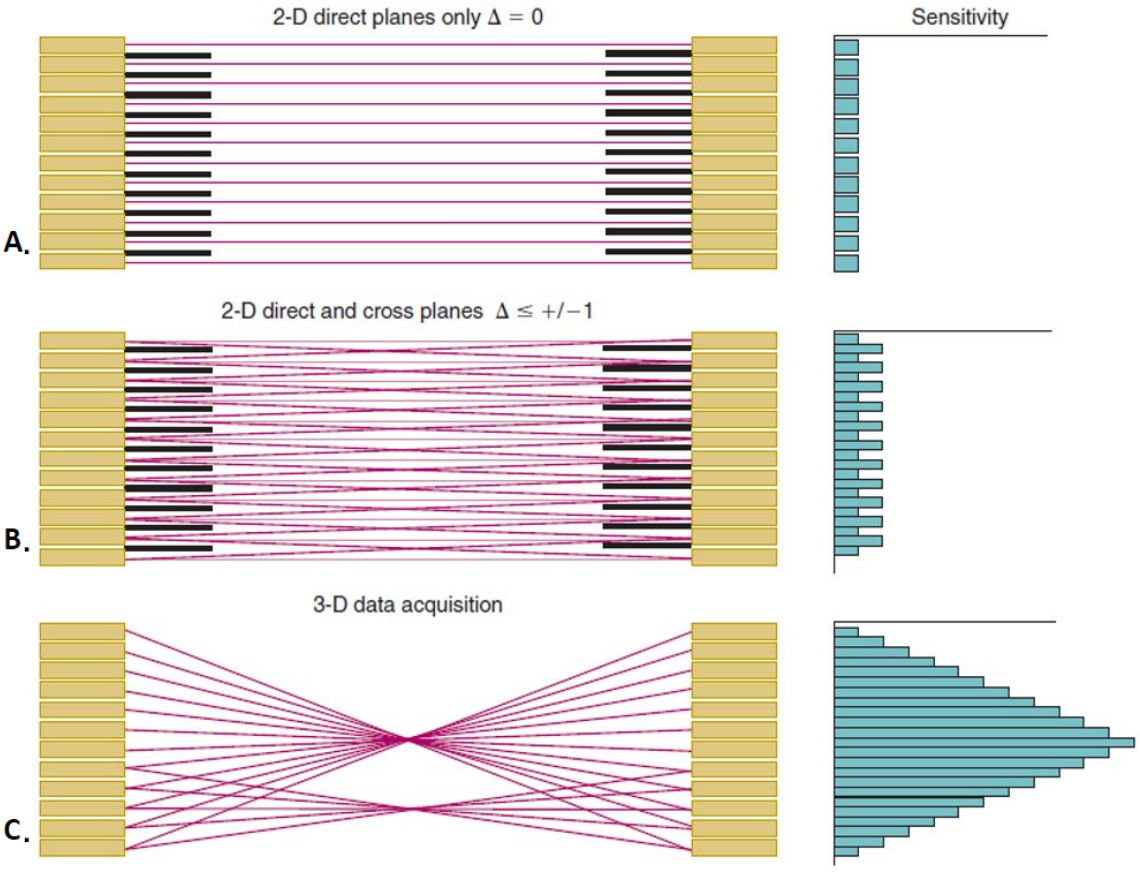

Figure 5.1: Axial cross-sections through a multi-ring scanner are shown on the left, and the corresponding axial sensitivity profiles on the right. Δ is the ring index difference. A. 2D direct planes acquisition. B. 2D direct and cross planes acquisition. C. 3D oblique planes acquisition. Adapted from (Cherry et al., 2012).

However, the use of septas results in the rejection of many possible valid photons, which in turn leads to low system sensitivity. In the three-dimensional (3D) acquisition mode, the septas are removed to allow coincidence detection between different detector rings (see Figure 5.1C). Oblique planes can then be defined for each possible combination of detector rings, in addition to the direct and cross planes mentioned above. For an N-rings PET system, a maximum of N^2 planes can be defined.

Although more scattered and random counts are recorded without the septas, the gain in sensitivity is in the range of 5 to 7 times when compared to 2D acquisitions (Lodge et al., 2006). The axial sensitivity profile resulting from a 3D acquisition is no longer uniform but rather triangular, peaking at the centre of the axial FOV. At the axial extremities of the FOV, the sensitivity is comparable to that of 2D acquisitions.

Initially, the 3D acquisition mode was hampered by the need for significant storage capacity, as well as high reconstruction time and complexity. These limitations have been overcome by technological advances over the past few decades, and the 2D mode has now been replaced by the 3D mode in the clinical setting.

5.2/ DATA STORAGE

5.2.1/ LIST-MODE

During a PET acquisition, the recorded events and their properties can be stored sequentially in a single file, called a list-mode file. This list-mode format records the detector index, measured energy, and detection time (timestamp) of each photon. A list-mode can either contain all single events or be restricted to coincidence events only.

The main advantage of this data storage mode is the availability of the properties of each photon. It can be used to extract TOF information, and to perform time-dependent post-processing techniques, such as tracer kinetics analysis from dynamic imaging or respiratory motion correction.

The availability of this detailed information comes at the price of a very large file, the size of which is proportional to the event rate. Thanks to recent technological developments, the size of list-mode files acquired in a clinical setting is not an issue. However, for research purposes, where a higher activity may be used, the list-mode can reach several hundred GigaByte (GB), which can cause problems in storing, compressing, transferring, reading, and processing the data (see Chapter 11). Nevertheless, the list-mode format is expected to become the data storage method of choice for PET acquisition due to the possibilities offered by its flexibility.

5.2.2/ SINOGRAMS

5.2.2.1/ 3D SINOGRAM

The fundamental assumption in PET imaging is that the position of the $\beta+$ emitter lies somewhere along the LOR connecting the two detectors involved in the detection.

When considering a single ring of detectors, the annihilation photon pairs associated with this direct plane can be arranged in a 2D matrix (also called a 2D histogram), where each

cell in this matrix corresponds to the number of events recorded along a given LOR. Each row of this matrix represents a projection, which is the number of events recorded at a given angle, denoted ϕ, while each column represents the radial offset from the centre of the PET gantry, denoted r (see Figure 5.2).

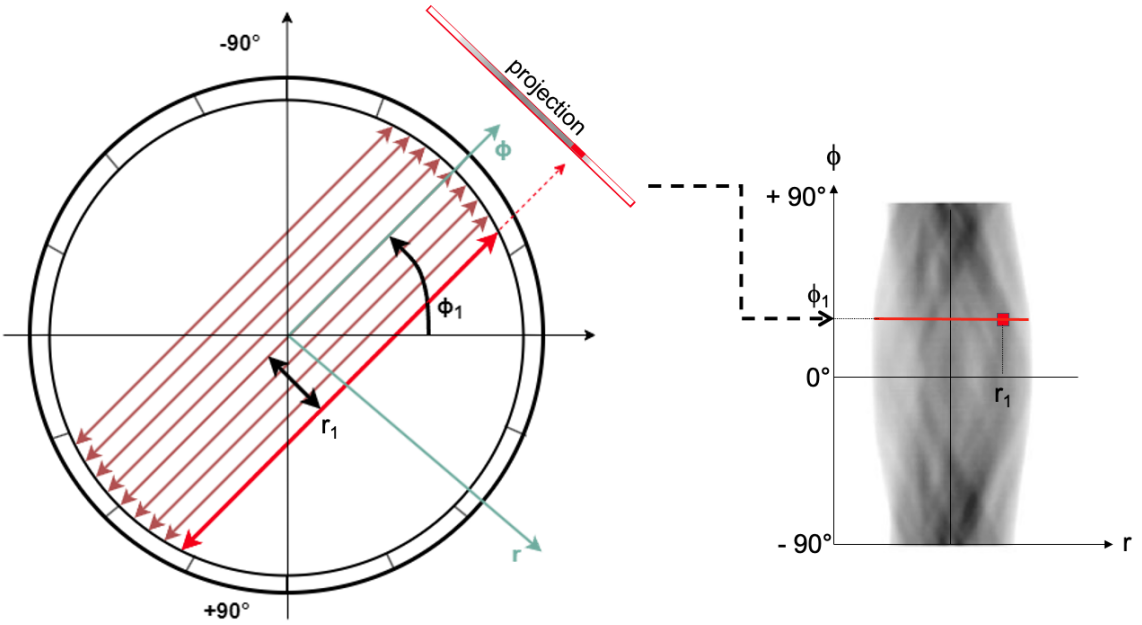

Figure 5.2: Illustration of the placement of a LOR of angle ϕ_1 at a radial distance r_1 in a sinogram

The content of a given sinogram line therefore represents all the parallel LORs of angle ϕ. This data organisation leads to the representation of a point object in image space as a sinusoidal line in sinogram space, as shown in Figure 5.3. The projection angles in a sinogram are only considered over $180°$ and not over $360°$, because the information between the detector pair $(\mathrm{d_a}, \mathrm{d_b})$ is redundant with the information of the pair $(\mathrm{d_b}, \mathrm{d_a})$.

Considering a system with N detector rings and d detectors around each ring, the N direct planes can be represented as N sinograms, which can be stacked axially to store the data acquired in 2D mode.

In the case of a 3D acquisition, a 2D sinogram must be generated for each possible combination of detector rings. Each oblique coincidence plane is defined by its azimuthal angle, denoted θ (often called the slice number), and can be arranged in a 3D sinogram of axis $(\mathrm{r}, \phi, \theta)$.

For the same PET system with N detector rings, a total of N^2 2D sinograms can be formed. Therefore, it is common to index the θ of the 3D sinogram from 0 to $\mathrm{N}^2 - 1$ ($\theta_{\mathrm{index}} \in [\![0, \mathrm{N}^2[\![$).

Then the number of detectors det (assumed to be even) around the ring can be used to index values of ϕ. Since the projections of the sinogram only cover $180°$ (from $-90°$ to $+90°$ on Figure 5.2), ϕ can be indexed on $\phi_{\mathrm{index}} \in [\![0, \frac{\mathrm{det}}{2}[\![$.

Finally, the r axis of the sinogram should span the FOV of the system. A practical way of sampling r is again to use the number det of crystals around the ring. Using parallel lines passing through opposite pairs of detectors, and therefore orthogonal to the projection plane, each projection can be sampled in $\frac{\mathrm{det}}{2}$ radial distance bins. Using this approach, the resulting radial bins are non-uniform due to the arc effect (see Instrumentation induced

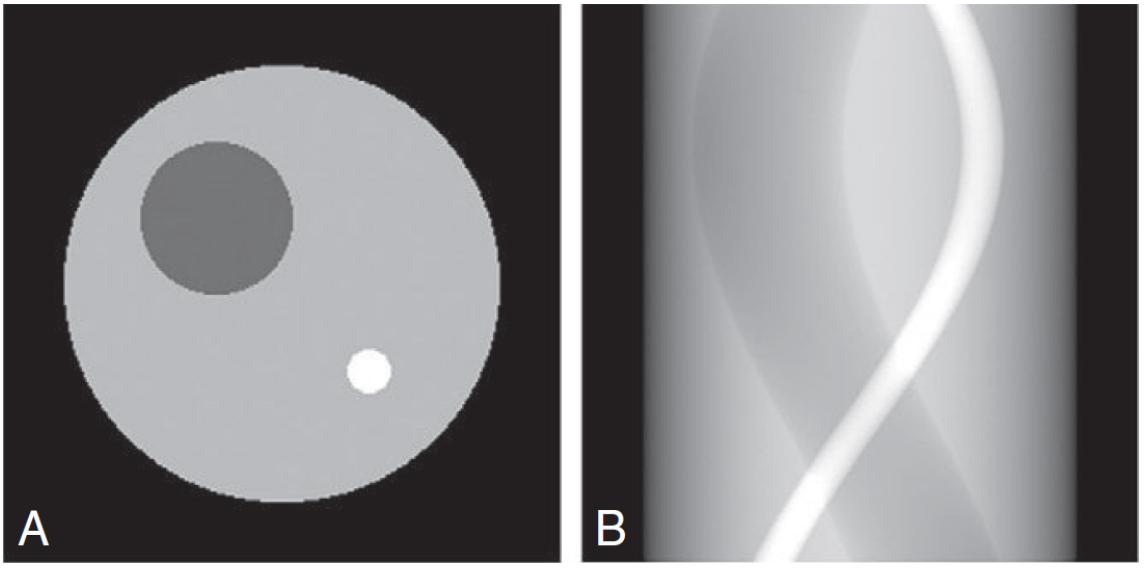

Figure 5.3: A. a cylindrical object in 2D image space with two regions, and B. the same cylindrical object in projection space over $180°$(Cherry et al., 2012).

biases).

It should be noted that, unlike the list-mode format, the size of the sinogram depends only on the number of LORs to be stored. Its size is therefore independent of the counting rates. It can also be extended with additional dimensions to store additional data, such as the TOF information, by sampling each LOR according to the measured TOF difference. The sinogram is often the storage method of choice, as each detected coincidence results in only one value increment, rather than a new entry with multiple values for the list-mode. This method of data storage method is less demanding on the input/output (IO) electronics of the PET system than a list-mode format.

5.2.2.2/ SINOGRAM REBINNING ALGORITHMS

Nowadays, 2D PET acquisitions have been abandoned in favour of 3D acquisitions, where the acquired data is stored in 3D sinograms. However, 2D sinograms are still useful for performing simple analysis tasks, fast reconstructions, and visual inspections, that are difficult or impossible to perform on 3D sinograms. Algorithms that can be used to reorganise 3D sinogram data into 2D sinograms containing only direct and cross planes are called rebinning algorithms. The most popular are single-slice rebinning (SSRB) (Daube-Witherspoon et al., 1987) and fourier rebinning (FORE) (Defrise et al., 1997). These algorithms are approximations of the three-dimensonnal reprojection (3DRP), a 3D FBP method, leading to fast implementation and execution. For example, to study the counting properties of a PET system, the SSRB (zeroth-order approximation) is generally sufficient, while the FORE (first-order approximation) has proved to be a reliable alternative to the 3DRP algorithm (Defrise et al., 1997) and is therefore more suitable for qualitative evaluations.

A visual example of the SSRB algorithm is given in Figure 5.4, using data from a PET system with $\mathrm{N} = 6$ detector rings. A two-ring combination is identified by the pair $(\mathrm{d}_1, \mathrm{d}_2)$, where d_1 and d_2 are individual ring indexes. In this example uses zero-indexing for the

detector rings and stacked rebinned 2D sinograms. The indexes are sorted with respect to the Z-axis of the scanner (head-to-feet) and only four different oblique planes are considered. All 2D direct planes can be directly associated with the corresponding 2D direct sinograms (Figure 5.4A, blue colour). The oblique planes are then rebinned to fall in either a direct plane or a cross-plane (Figure 5.4B, green colour) according to their ring index sum $d_1 + d_2$[1]. For example, the two oblique planes defined by $(1, 4)$ and $(0, 5)$ are both rebinned in the 2D sinogram number 5. When multiple planes are rebinned into the same 2D sinogram, their data are summed to obtain the final SSRB sinogram. Therefore, although it is a stack of 2D sinograms, the sensitivity of the resulting SSRB sinogram is triangular in shape, peaking at the central detector ring (see Figure 5.1C).

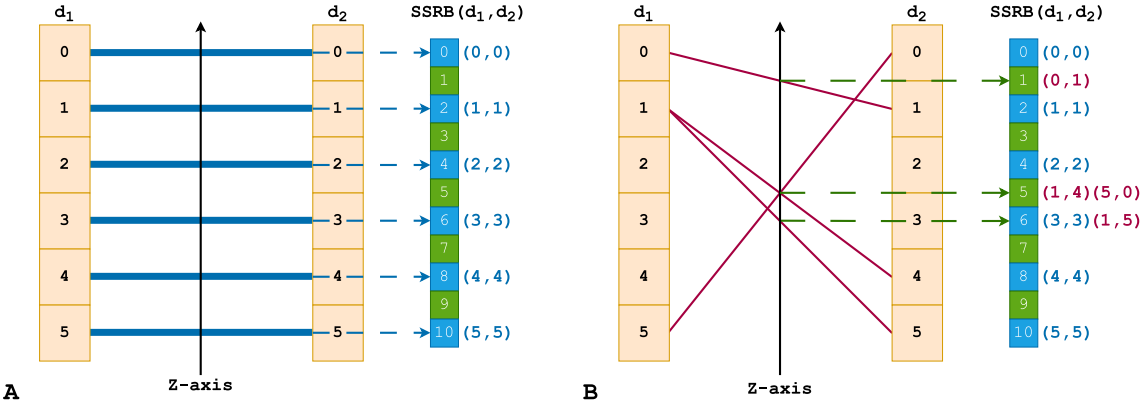

Figure 5.4: Illustration of the SSRB algorithm on a PET system with six detector rings. A. Standard formation of direct planes. B. Rebinning of oblique planes in direct and cross-planes using SSRB.

[1] Defrise et al. (1997) uses the ring difference, denoted δ, rather than the ring index sum due to a different indexing methodology. Nonetheless, both indexing methods give equivalent results.

6

RECONSTRUCTION

The aim of tomographic reconstruction is to obtain an image of the spatial distribution of the radiotracer in the FOV using the data acquired along each LOR. Given that a 3D PET image can be seen as a stack of 2D PET images (often referred to as slices), and to simplify this chapter, we will focus on the reconstruction of a 2D slice from 1D projections. First, analytical methods are described, where tomographic reconstruction is considered as a continuous linear inverse problem. Then, iterative reconstruction methods are introduced and three specific algorithms are presented: maximum likelihood expectation maximisation, ordered-subsets expectation-maximisation, and block-sequential regularised expectation maximisation. Finally, the incorporation of TOF data into the iterative reconstruction process is described.

6.1/ ANALYTICAL RECONSTRUCTION

Analytical reconstruction methods were the earliest approaches used in PET imaging. Based on the integral line model and assuming noise-free data, they aim to find a direct mathematical solution to transform the acquired projections into an image.

6.1.1/ RADON TRANSFORM

In the context of 2D reconstruction, only LORs that lie within a given imaging plane are considered. The location of a LOR can be described by the polar coordinates (x_r, ϕ), as shown in Figure 6.1. A rotating coordinate system (x_r, y_r) can be defined. It is linked to the Cartesian coordinates x and y according to Equation 6.1.

$$\begin{bmatrix} x \\ y \end{bmatrix} = \begin{bmatrix} \cos\phi & -\sin\phi \\ \sin\phi & \cos\phi \end{bmatrix} \begin{bmatrix} x_r \\ y_r \end{bmatrix} \tag{6.1}$$

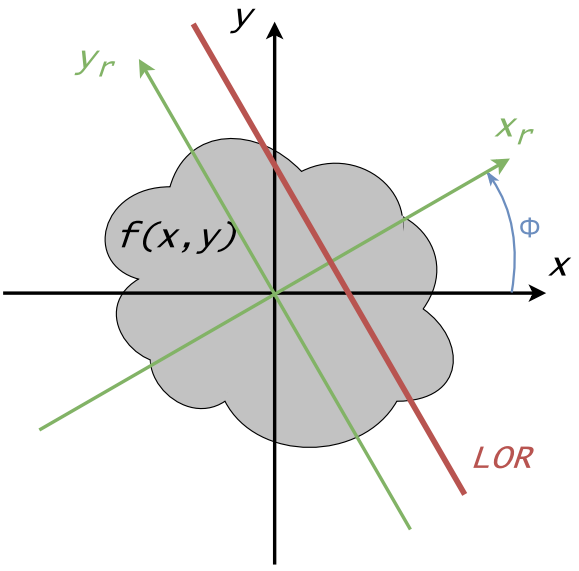

Figure 6.1: Illustration of the rotating coordinate system used to describe the position of the LOR.

Using this rotated coordinate system, the 1D projection p of f in the direction $(-sin(\Phi), cos(\Phi))$ is given by the integral of f along that direction. For all values of x_r and Φ, we obtain the Radon transform, which is formally defined as follows:

$$p(x_r, \phi) = \int_{-\infty}^{+\infty} f(x_r \cos\phi - y_r \sin\phi,\ x_r \sin\phi + y_r \cos\phi)\, dy_r, \forall x_r \in \mathbb{R}, \forall \phi \in \mathbb{R} \tag{6.2}$$

The 1D projections obtained at different angles ϕ are often stored in a 2D sinogram (see Section 5.2.2). The primary goal of analytical reconstruction is to invert the Radon transform and reconstruct the activity distribution f from the values $p(x_r, \phi)$, i.e. from the projections p.

6.1.2/ FILTERED BACKPROJECTION

An initial estimate f^* of the activity distribution f can be obtained by simple backprojections. For all points $(x, y) \in \mathbb{R}^2$, this consists in summing all the projections passing through that point:

$$f^*(x, y) = \int_0^{\pi} p(x_r, \phi) d\phi = \int_0^{\pi} p(x \cos\phi + y \sin\phi,\ \phi)\, d\phi \tag{6.3}$$

For a given LOR (x_r, ϕ), backprojecting the value of the projection $p(x_r, \Phi)$ is equivalent to copying the value $p(x_r, \Phi)$ to the points (x, y) belonging to the LOR. The simple backprojection f^* is not the true inverse of the Radon transform, but rather a blurring estimate of it. With a limited number of projection angles, this approach introduces streak artefacts along the backprojected lines. Although an infinite number of projections can reduce these artefacts, it would still result in a blurred, low-contrast image with apparent activity outside the true source.

One method for removing the blur caused by simple backprojections is to filter the projections in Fourier space. This method is called FBP and provides an exact inverse of the Radon transform. The central slice theorem, which is used in many analytical reconstructions, is applied in the FBP. It states that for a given angle ϕ, the 1D Fourier transform, denoted $\mathcal{F}_1$, of a projection p with respect to x_r is equal to the 2D Fourier transform, denoted $\mathcal{F}_2$ of the image f:

$$\forall v_x, v_y \in \mathbb{R}, \mathcal{F}_2[f](v_x, v_y) = \mathcal{F}_1[p](v_r, \phi) \tag{6.4}$$

with

$$\mathcal{F}_1[p](v_r, \phi) = \int_{-\infty}^{+\infty} p(x_r, \phi) e^{-2i\pi v_r x_r} dx_r \tag{6.5}$$

and

$$\mathcal{F}_2[f](v_x, v_y) = \int_{-\infty}^{+\infty} \int_{-\infty}^{+\infty} f(x, y) e^{-2i\pi(v_x x + v_y y)} dxdy \tag{6.6}$$

where $v_x = v_r cos(\phi)$ and $v_y = v_r sin(\phi)$ the polar coordinates of x, y, respectively, in Fourier space.

Using the inverse 2D Fourier transform, denoted $\mathcal{F}_2^{-1}$, of $\mathcal{F}_2[f]$, the activity distribution f can be expressed as follows for all $(x, y) \in \mathbb{R}^2$:

$$f(x, y) = \mathcal{F}_2^{-1}[\mathcal{F}_2[f]](x, y) = \int_{-\infty}^{+\infty} \int_{-\infty}^{+\infty} \mathcal{F}_2[f](v_x, v_y) e^{i2\pi(v_x x + v_y y)} dv_x dv_y \tag{6.7}$$

Using the central slice theorem described in Equation 6.4, it is possible to rewrite Equation 6.7 as follows:

$$f(x, y) = \int_{-\infty}^{+\infty} \int_{-\infty}^{+\infty} \mathcal{F}_1[p](v_r, \phi) e^{i2\pi(v_x x + v_y y)} dv_x dv_y \tag{6.8}$$

By replacing v_x and v_y with their previous definitions, we can further simplify Equation 6.8:

$$f(x,y) = \int_0^{\pi} \int_{-\infty}^{+\infty} |v_r| \mathcal{F}_1[p](v_r,\phi) e^{i2\pi v_r(cos(\phi)x+sin(\phi)y)} dv_r d\phi \tag{6.9}$$

According to Equation 6.9, to obtain the image f from its projections, we must (1) for each projection calculate its 1D Fourier transform; multiply by the absolute value of $|v_r|$ (filter it) and compute the inverse Fourier transform; and then (2) perform the simple backprojection of these filtered projections. Although filtering the projections in the frequency domain by $|v_r|$, known as the ramp filter, theoretically removes the blurring of the simple backprojection and thus allows the image f to be reconstructed exactly from its projections, this filter also amplifies the high frequencies and therefore the noise. To remedy this, the ramp filter can be multiplied by an apodisation window, which suppresses the high frequencies. The two most common apodisation windows are the Hann window and the Butterworth window.

6.1.3/ LIMITATIONS

The equations described above can be applied to 1D projections stored in a 2D sinogram to obtain a stack of 2D images. For 3D sinograms, the azimuthal angle θ is taken into account for all projections. While implementing 2D backprojection for image reconstruction is relatively straightforward, 3D backprojection is computationally intensive due to the additional integration over the azimuthal angle and the need for axial data interpolation. Proper filtering of back projections in 3D space adds further complexity. Although extensively studied, the use of fully 3D FBP is typically avoided due to its complexity (Kinahan et al., 2004). A simpler solution is to use the rebinning algorithms described in Section 5.2.2.2, which reorganise a 3D sinogram into 2D sinograms, allowing the 2D FBP method described above to be used.

Despite its speed, ease of implementation, and visually accurate reconstructions, 2D FBP is not without limitations. Any inaccuracies in the acquired data or in the detection system can lead to significant errors in the frequency domain during backprojection. While detectors are considered to be punctual in the context of FBP, they have thickness and width in the real world. As a result, the solid angle of each detector varies depending on the source location, leading to sensitivity variations between detector pairs. In addition, several limitations of the acquisition system, such as the spatial resolution of the detectors and scattered radiations, cannot be taken into account with FBP.

6.2/ ITERATIVE RECONSTRUCTION

6.2.1/ INTRODUCTION

While analytical methods try to solve a line integral, iterative reconstruction algorithms are based on a discrete formulation of the reconstruction problem. Let f be an image vector (also called an activity vector) of J elements and p be the projection vector of I elements. Here, f can contain either pixels (2D) or voxels (3D)[1], and p can contain 1D

[1] Other data representations have been proposed (blobs, Lewitt (1992)), but are less common.

or 2D projections. The link between the projection data and the resulting image can be written as:

$$p = Hf \iff \forall i \in [\![1, I]\!], p_i = \sum_{j=1}^{J} \mathrm{H}_{i,j} f_j, \tag{6.10}$$

where H is the system matrix of size $I \times J$ used to model a combination of degrading effects (see Chapter 7). Ultimately, each element $\mathrm{H}_{i,j}$ of H contains the probability that an annihilation occurring in the image element j contributes to the data acquired in the projection element i. An intuitive solution to the discrete tomographic reconstruction problem would be to inverse H to obtain f. However, H is of high dimension, usually not a square matrix, so it is often difficult or impossible to invert it directly.

6.2.2/ ITERATIVE ALGORITHMS CONCEPT

Iterative algorithms attempt to obtain the true radiotracer distribution in the object, denoted f, by successive (iterative) estimates of the radiotracer distribution, denoted f^*, using the projection data acquired by the system, denoted p.

An initial image estimate of f is determined and used to obtain the associated forward projection estimate, denoted p^*. A cost function is then used to quantify the similarity between the current projection estimate and the measured projection. Based on the observed difference, the image estimate is updated and used to obtain the next projection estimate. The updating process ensures that the estimated projections are closer to the measured projections for the next iteration.

This 'forward project - compare, back-project - update' process is repeated until one of the following two criteria is met: either 1) the cost function is minimised, or 2) a pre-defined number of iterations is reached. Figure 6.2 illustrates this general workflow for an iterative tomographic reconstruction of a 2D object.

Iterative reconstruction algorithms can be divided into algebraic and statistical methods. Algebraic methods aim to solve the linear Equation 6.10 by minimising the L2 norm between the estimated projections and the actual projections. Notable algorithms in this category are the algebraic reconstruction technique (ART) (Gordon et al., 1970) and the simultaneous algebraic reconstruction technique (SART) (Gilbert, 1972) methods. For the reconstruction of PET data, statistical methods are preferred because they model the statistical nature of the noise contained in the acquired data. Among these methods, the maximum likelihood expectation maximisation (MLEM) algorithm, first proposed by Dempster et al. (1977) and later adapted to emission tomography by Shepp et al. (1982), is used as the basis for most clinical reconstruction algorithms in PET studies. Therefore, the rest of this Chapter is dedicated to this class of algorithms.

6.2.3/ MAXIMUM-LIKELIHOOD EXPECTATION-MAXIMISATION

Since photon emissions and detections are assumed to follow a Poisson distribution, most statistical methods use a Poisson distribution to model the projection data[2]. The

[2]Other statistical models can be used to properly represent changes in the measurement distribution, especially due to data correction and high count rates.

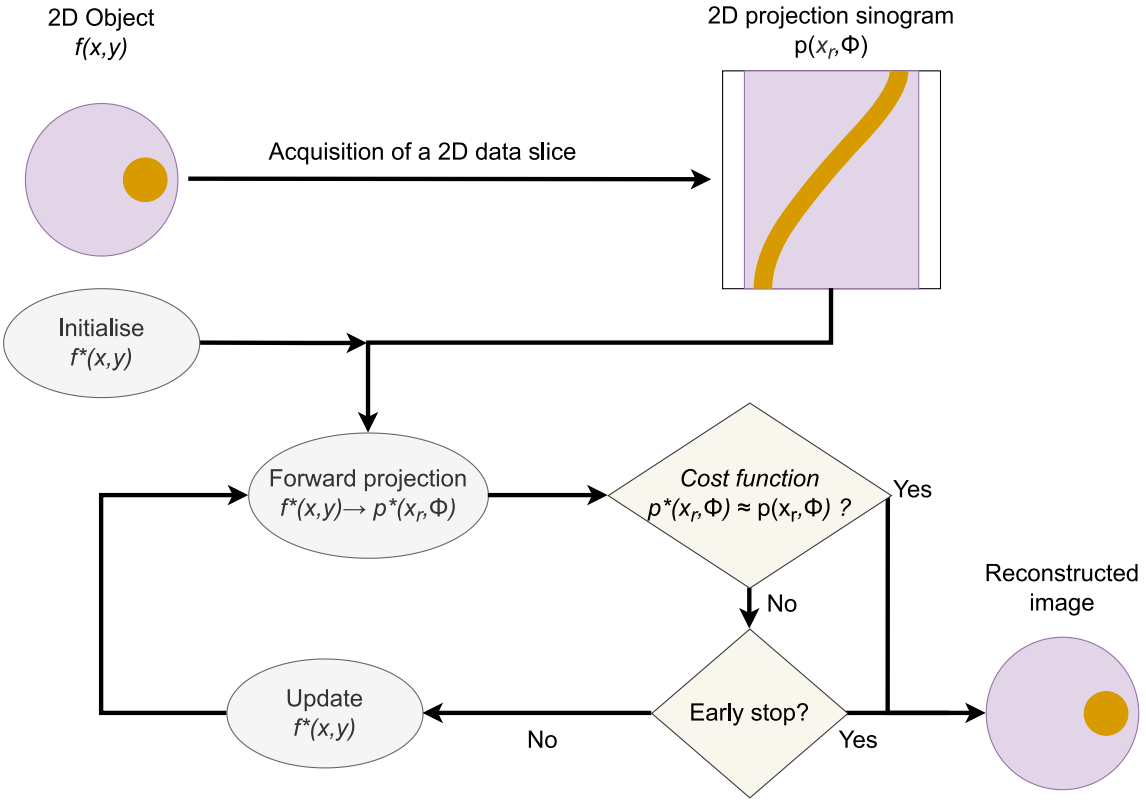

Figure 6.2: Illustration of the steps involved in iterative tomographic reconstruction of 2D data. The image estimate is progressively updated towards an improved solution by minimising a cost function.

probability of detecting p_i photons in the projection element i is given by:

$$P(p_i|\overline{p_i}) = e^{-\overline{p_i}} \frac{\overline{p_i}^{p_i}}{p_i!}, \tag{6.11}$$

where $\overline{p_i}$ is the mean number of photons detected by the projection element i.

We can rewrite Equation 6.10 to take account of the statistical nature of the data as follows:

$$\overline{p} = \mathrm{H}\overline{f} \iff \forall i \in [\![1, I]\!], \overline{p_i} = \sum_{j=1}^{J} \mathrm{H}_{i,j}\overline{f_j}, \tag{6.12}$$

where $\overline{f_j}$ is the mean number of annihilations in image pixel j.

The MLEM algorithm aims to find the mean number of annihilations in the image that can produce the projection vector p with the highest likelihood:

$$P(p|\overline{f}) = \prod_{i=1}^{I} P(p_i|\overline{p_i}) = \prod_{i=1}^{I} e^{-\overline{p_i}} \frac{\overline{p_i}^{p_i}}{p_i!} \tag{6.13}$$

Using Equation 6.12, we obtain:

$$P(p|\overline{f}) = \prod_{i=1}^{I} \frac{e^{-\sum_{j=1}^{J} \mathrm{H}_{i,j}\overline{f_j}} (\sum_{j=1}^{J} \mathrm{H}_{i,j}\overline{f_j})^{p_i}}{p_i!} \tag{6.14}$$

Equation 6.14 is the formulation of the likelihood to be maximised. This formulation, which involves the multiplication of probabilities, is not convenient for optimisation purposes. To obtain an additive formulation of Equation , one approach is to maximise the logarithm of the likelihood (the log-likelihood) instead:

$$\max_{\overline{f}\geq 0}(\ln(P(p|\overline{f}))) = \sum_{i=1}^{I}\Big(-\sum_{j=1}^{J} \mathrm{H}_{i,j}\overline{f_j} + p_i\ ln(\sum_{j=1}^{J} \mathrm{H}_{i,j}\overline{f_j}) - ln(p_i!)\Big) \tag{6.15}$$

Since the last term ($ln(p_i!)$) is constant, it can be ignored in the maximisation process:

$$\max_{\overline{f}\geq 0}(\ln(P(p|\overline{f}))) = \sum_{i=1}^{I}\Big(-\sum_{j=1}^{J} \mathrm{H}_{i,j}\overline{f_j} + p_i\ ln(\sum_{j=1}^{J} \mathrm{H}_{i,j}\overline{f_j}))\Big) \tag{6.16}$$

The image vector $\overline{f}$, for which the log-likelihood reaches its maximum value, is found by solving the following equation:

$$\frac{\partial \ln(P(p|\overline{f}))}{\partial \overline{f_j}} = -\sum_{i=1}^{I} \mathrm{H}_{ij} + \sum_{i=1}^{I} \frac{p_i}{\sum_{j=1}^{J} \mathrm{H}_{ij}\overline{f}_j} \mathrm{H}_{ij} = 0 \tag{6.17}$$

This Equation cannot be solved analytically. Instead, the expectation maximisation (EM) algorithm is used to iterate towards an estimate solution. The MLEM update can be written as:

$$\overline{f_j^{n+1}} = \frac{\overline{f_j^n}}{\sum_{i=1}^{I} \mathrm{H}_{ij}} \sum_{i=1}^{I} \mathrm{H}_{ij} \frac{p_i}{\sum_{j=1}^{J} \mathrm{H}_{ij}\overline{f_j^n}} \tag{6.18}$$

Equation 6.18 is the final MLEM algorithm formulation, and can be understood as:

$$\overline{f_{\text{new}}} = \overline{f_{\text{old}}} \times \mathrm{NBP}\Big(\frac{\text{Measured Proj}}{\text{Proj of}\,\overline{f_{\text{old}}}}\Big), \tag{6.19}$$

where f_{old} and f_{new} are the previous and current image estimates, respectively. NBP is the normalised backprojection operator (normalised by $\sum_{i=1}^{I} \mathrm{H}_{ij}$), and Proj are the projections.

For the first iteration, an initial image estimate is given. Due to the multiplicative nature of the update rule, a constant positive non-null image is often used.

The MLEM algorithm provides a predictable convergence (between 50 to 200 iterations), but the images it converges on are very noisy (Shepp et al., 1982). To reduce the noise, a smoothing post-filtering process can be applied, or the MLEM algorithm can be stopped early, before convergence. This early stopping can follow a criterion (Veklerov et al., 1987), or a user-defined fixed number of iterations. Finally, the convergence of MLEM is slow because backward and forward projections are used at each iteration on the complete projection set (see Equation 6.19 and Figure 6.2).

6.2.4/ ORDERED-SUBSETS EXPECTATION-MAXIMISATION

Several methods have been proposed to deal with the slow convergence of MLEM. The ordered-subsets expectation-maximisation (OSEM) algorithm (Hudson et al., 1994) is the most popular, where projection data are divided into S_b subsets (often disjoint), with S_b being the subset b. The estimate update is applied to each subset, rather than to the entire projection data. It is worth noting that the convergence of OSEM has not been proven, but it has been observed empirically that the estimated image after n iterations of OSEM is close to that after $b \times n$ iterations of MLEM. Therefore, OSEM updates the image estimates b times more than MLEM, resulting in about a b-fold reduced reconstruction time. This speed increase has made OSEM the reconstruction algorithm of choice in clinical routine. MLEM can be seen as OSEM with $b = 1$, and the OSEM update rule can be written as:

$$\overline{f_j^{(n,b)}} = \frac{\overline{f_j^{(n,b-1)}}}{\sum_{i' \in S_b} H_{i'j}} \sum_{i \in S_b} H_{ij} \frac{p_i}{\sum_k H_{ik} \overline{f_k^{n,b-1}}}, \tag{6.20}$$

where $\overline{f}$ is the image estimate, j and k are the voxel indices, i and i' are the projection vector indices, n is the iteration number, H is the system matrix, and p is the measured projection vector.

6.2.5/ BLOCK-SEQUENTIAL REGULARISED EXPECTATION MAXIMISATION

Block-sequential regularised expectation maximisation (BSREM) algorithms, originally proposed by De Pierro et al. (2001), use prior knowledge of image quality to penalise differences in the values of neighbouring image elements. This allows every image element to achieve full convergence, resulting in a globally convergent image (Ahn et al., 2003). Ross (2014) presented Q.Clear (Q.Clear; GE Healthcare), the only implementation of a BSREM available for clinical PET data reconstruction. It is a Bayesian penalised likelihood algorithm, where an additional term is added to Equation 6.16:

$$\max_{f \geq 0}(\ln(P(p|\overline{f}))) = \sum_{i=1}^{I}\Big(-\sum_{j=1}^{J} H_{i,j}\overline{f_j} + p_i \, ln(\sum_{j=1}^{J} H_{i,j}\overline{f_j}) - \beta \, R(\sum_{j=1}^{J} H_{i,j}\overline{f_j})\Big), \tag{6.21}$$

where R is the Relative Difference Penalty (RDP) (Nuyts et al., 2002) used to penalise noise, and β is a user-defined constant that controls the relative strength of the regularisation term relative to the data statistics (Ross, 2014). The BSREM algorithm is then used to solve Equation 6.21 (De Pierro et al., 2001; Ahn et al., 2003). Since BSREM can be ran to full convergence without excessive introduction of noise, there is no need for an early stop. Therefore, in contrast to OSEM, where iterations and subsets are chosen by the user, BSREM only offers β as a reconstruction parameter. The values of β need to be optimised according to the field of application (oncology, PET/computed tomography (CT)) and specific combinations of PET systems, acquisition time, and radiotracers (Teoh et al., 2015; Reynés-Llompart et al., 2018; Lindström et al., 2020).

6.2.6/ TOF RECONSTRUCTION

As mentioned in Section 5.2, recent PET systems are able to acquire TOF information as supplementary data for each LOR. These data are represented by the arrival time difference, denoted Δt (as defined in Equation 3.2). In the reconstruction processes described above, the emission probability of a photon along a given LOR was uniform (see Figure 6.3A). With TOF information, it is possible to restrict the emission probability (while keeping the probability sum to 1) to only a part of this LOR (see Figure 6.3B).

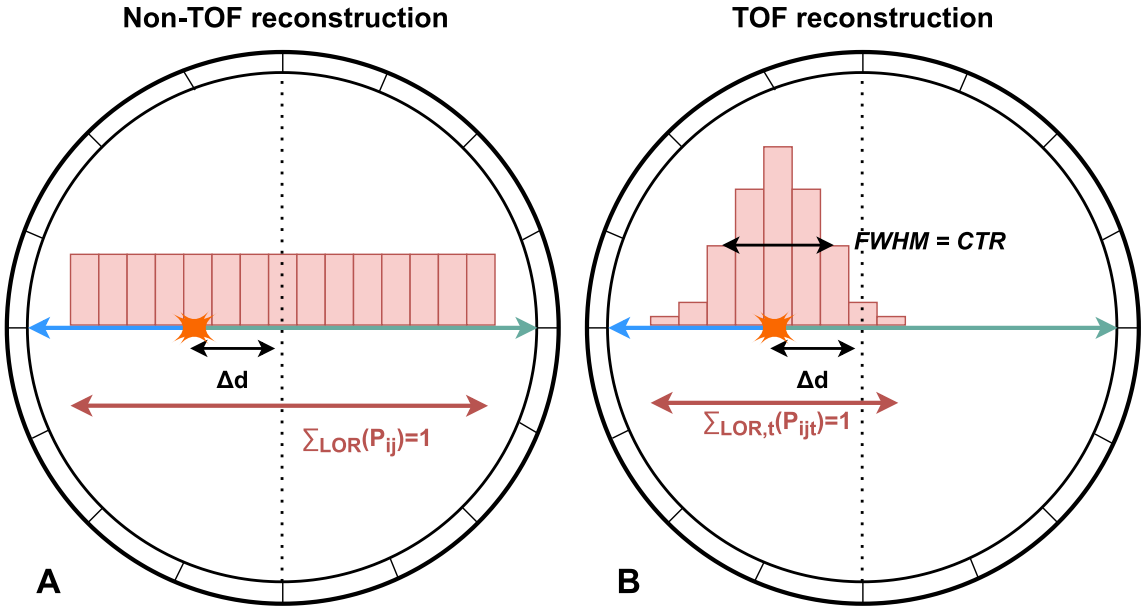

Figure 6.3: Distribution of emission probability on a LOR for a given annihilation. **A** a non-TOF reconstruction, where the emission probabilities are equally distributed along the LOR considered. **B** a TOF reconstruction, where the distance Δd (see Equation 3.3) is used to centre a Gaussian kernel of FWHM CTR.

.

However, the value Δt is affected by the scanner's CTR, and is therefore subject to inaccuracies, which are assumed to follow a Gaussian distribution (see Equation 3.5). Therefore, the emission probability along the LOR is modelled by a Gaussian kernel centred around Δd (see Equation (see Equation 3.3), the most probable annihilation location, and the CTR of the system is used to set the FWHM of the kernel. In the case of an OSEM reconstruction with TOF information, the general OSEM iterative algorithm 6.20 can be written as follows:

$$\overline{f_j^{(n,b)}} = \frac{\overline{f_j^{(n,b-1)}}}{\sum_{i' \in S_b} H_{i'tj}} \sum_{i \in S_b} H_{ijt} \frac{p_i}{\sum_k H_{ikt} \overline{f_k^{n,b-1}}}, \tag{6.22}$$

where t is the indexing of the TOF probabilities.

7

PET DATA CORRECTION

The ultimate goal of PET imaging is to provide an intensity image where the value of the image elements is proportional to the amount of activity (or concentration) at the corresponding location in the object. This proportionality is important to accurately quantify activity levels in different organs or tissues. To do this, the data to be reconstructed must be corrected for many deleterious factors, either before, during, or after the reconstruction process. These factors have been described in Chapter 4, and the system matrix H mentioned in section 6.2.2 can be written according to the contribution of each physical effect (Qi et al., 1998; Qi, 2005):

$$H = H_{range} H_{norm} H_{blur} H_{geom} H_{attn} \tag{7.1}$$

where H_{range} is the positron range (Section 4.1.1), H_{norm} is the normalisation factor of the detectors sensitivities (Section 7.2), H_{blur} is the combination of the blur caused by inter-crystal scattering (Section 4.1.4), non-collinearity of the positrons (Section 4.1.2) and DOI effect (Section 4.2.3) combined with finite crystal dimensions (Section 4.2.1), H_{geom} contains the detection probabilities according to the solid angle of the detectors, and H_{attn} represents the attenuation of photons in the object (Section 4.1.3). In this Chapter, the methodology associated with each correction is described.

7.1/ ARC EFFECT

Due to the curved nature of the detector ring, LORs passing near the centre of the FOV are more widely spaced than LORs at the extremities of the FOV (see Section 4.2.4). In analytical reconstruction methods such as FBP, the data are assumed to be uniformly sampled, so a resampling method must be used before the reconstruction process. For iterative reconstruction algorithms, this effect is taken into account in the geometric model of the system matrix (H_{geom} in Equation 7.1).

7.2/ NORMALISATION

For PET data, the normalisation correction H_{norm} is used to compensate for any non-uniform sensitivity of the LORs.

All LORs passing through the centre of the FOV are orthogonal to their respective detector surface (see Figure 7.1a). However, for LORs that do not intersect with the centre of the FOV, the incoming photon will strike the crystal surface at a non-orthogonal angle and the crystal thickness encountered will differ. At angles relatively close to 90 degrees with the detector surface (P1 on Figure 7.1b), a thickness equal to the crystal length can be traversed. At larger angles with the detector surface (P2 on Figure 7.1b), the larger detector thickness leads to a higher intrinsic detection efficiency. Therefore, the intrinsic detection efficiency is not uniform across the detector surface and is LOR-dependant, as a given LOR will always provide the same striking angle.

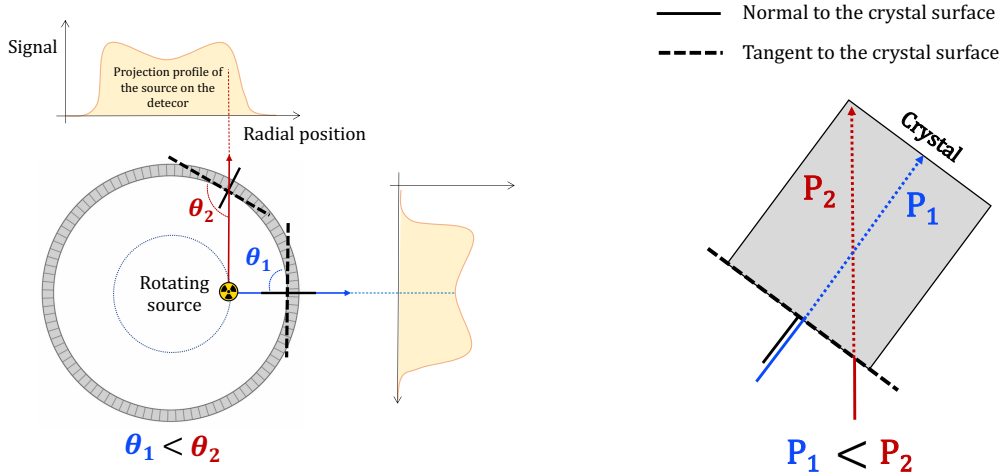

Figure 7.1: (a) Radial position of the rotating source on the projection profile, according to the angle to the detector surface (θ_1 and θ_2). **(b)** The detector thickness encountered by a photon striking the crystal surface normally (P_1 in blue) is less than that encountered by a photon striking at larger angles (P_2 in red).

In addition, the non-uniform sensitivity of LORs can be further amplified by differences in crystal efficiency caused by small random variations in crystal dimensions, changes in

the amount of light transferred from the crystal to the SiPM or PMT, or systemic variations in timing information.

A straightforward approach to obtaining the LOR-wise normalisation factor is the direct inversion technique. In this case, data are collected for each LOR using a single source, and the measured counts in each LOR are normalised to a single averaged value. While this method is achievable with a rotating point or line source of ^{68}Ge (Medicine, 1995), a very large number of counts would be required to obtain a satisfactory count statistic per LOR. In addition, low activity must be used to avoid dead time and pile-up effects. The acquisition time required to obtain system-wide normalisation factors is therefore of the order of days.

Alternatively, component-based normalisation methods (Hoffman et al., 1989; Ollinger, 1995; Medicine, 1995) using variance reduction techniques (Hoffman et al., 1989) can be used to improve the statistical accuracy of the data and reduce the acquisition time. For two detectors, denoted i and j, the resulting coincidence detection efficiency, denoted $\epsilon_{i,j}$, is the product of the individual detector efficiencies (ϵ_i and ϵ_j) and the LOR geometric efficiency, denoted $g_{i,j}$, as:

$$\epsilon_{i,j} = \epsilon_i \epsilon_j g_{i,j} \tag{7.2}$$

To obtain ϵ_i and ϵ_j, data are collected using a planar or cylindrical source. A variance reduction method is then used to reduce the statistical noise using data collected in the opposite fan detectors (Hoffman et al., 1989). According to this method, the crystal efficiency ϵ_i^u is estimated by summing all counts between the detector i in the scanner ring u and a fan group of similar detectors opposite to it (C_i^u). By computing all ϵ_i^u in a ring u, and with a sufficiently large number of fan detector elements in C_i^u, it can be shown that:

$$\epsilon_i^u = \frac{\overline{C_i^u}}{C_i^u}, \tag{7.3}$$

where $\overline{C_i^u}$ is the mean count observed over all detectors i in ring u. The geometric factors $g_{i,j}$ are assumed to be constant, since the structure of a PET system is not expected to change over time. Therefore, they are usually obtained (and later provided) by the manufacturer using a single acquisition with very high statistics.

The first approach described in the section (rotating ^{68}Ge source) used counts per LOR to find the normalisation factors. In contrast, the component-based normalisation method uses counts per detector, greatly reducing the statistical noise.

7.3/ ATTENUATION

Photon attenuation was introduced in Section 4.1.3, and is denoted H_{atten} in Equation 7.1. The coincidence detection method used in PET imaging is particularly suited to correct for photon attenuation. Consider a point source located at an unknown depth x in an attenuating volume of uniform attenuation μ and thickness L along a given LOR. Then the probabilities of two photons from the same annihilation, noted P_1 and P_2, escaping the volume without attenuation (i.e. reaching the detector ring) are given by:

$$P_1 = e^{-\mu x} \quad \text{and} \quad P_2 = e^{-\mu(L-x)} \tag{7.4}$$

The probability that both P_1 and P_2 escape the volume is given by their product:

$$P_1 \times P_2 = e^{-\mu x} \times e^{-\mu(L-x)} = e^{-\mu L} \tag{7.5}$$

From the above Equation 7.5, it can be seen that the attenuation of a LOR is given by the thickness L of the uniformly attenuating volume, and is independent of the source location x.

Prior to the commercialisation of hybrid PET/CT systems, dedicated PET scanners could use a rotating ^{68}Ge point or rod source to acquire transmission images before, during, or after the PET scan (Daube-Witherspoon et al., 1988). With the advent of PET/CT, the estimation of attenuation correction factors (ACFs) has shifted from transmission imaging with external radionuclide sources to CT-based ACFs estimation. The intensity of CT images is represented in Hounsfield unit (HU), which is a linear scaling of linear attenuation coefficients. This scaling is performed according to the CT effective energy E_{eff}, where air and water are assigned values of -1000 HU and 0 HU, respectively. The effective energy is defined as the energy of a monochromatic (single-energy) X-ray beam having the same attenuation coefficient as a polychromatic X-ray spectrum, such as that produced by a CT tube. The HU value of a given image element, denoted HU_{el}, is given by:

$$HU_{el} = 1000 \times \frac{\mu_{el}(E_{eff}) - \mu_{water}(E_{eff})}{\mu_{water}(E_{eff})}, \tag{7.6}$$

with μ_{el} the linear attenuation coefficient of the image element, which can be isolated knowing μ_{water}:

$$\mu_{el}(E_{eff}) = (1 + \frac{HU_{el}}{1000}) \times \mu_{water}(E_{eff}) \tag{7.7}$$

Since μ_{el} depends on the effective energy E_{eff}, and the CT beam energy is different from the PET photon energy (50-80 keV versus 511 keV), a conversion method must be used to perform PET attenuation correction using CT data. A basic approach is to segment the CT image into three classes according to the HU values: air, soft tissue, and bone (Kinahan et al., 1998). By using the linear attenuation coefficients of these materials at the desired energy (511 keV), it is possible to obtain an attenuation map suitable for attenuation correction at that energy. However, this simple approach is subject to error, as image elements close to tissue boundaries contain a mixture of materials, that are not modelled by the three classes defined earlier. In addition, tissues such as lungs have a wide range of densities, leading to variations in the linear attenuation coefficient within this region.

A hybrid approach has been proposed by Kinahan et al. (1998), combining CT segmentation (tissue and bone) by HU-based thresholding and class-specific HU scaling. Therefore, the linear attenuation coefficient as a function of HU is a piecewise linear function, with a discontinuity at the chosen threshold. As bone has a relatively high atomic number compared to tissue, there is a high probability of photoelectric interaction at X-ray energies. However, when considering an energy at 511 keV, the probability of photoelectric interactions decreases significantly in favour of Compton interactions. At lower Z-values

(soft tissue) both PET and CT energies favour Compton scattering. For this reason, a monoscaling of the HU-energy mapping cannot hold for all tissue types. This problem can be solved for any energy, denoted E, using a bilinear fitting approach described by Burger et al. (2002):

$$\mu^{PET} = \begin{cases} \mu^{PET}_{water}(E)(1 + \frac{HU_{el}}{1000}) & \text{if } HU_{el} \leq 0 \\ \mu^{PET}_{water}(E) + HU_{el}\frac{\mu^{CT}_{water}(\mu^{PET}_{bone} - \mu^{PET}_{water})}{1000(\mu^{CT}_{bone} - \mu^{CT}_{water})} & \text{if } HU_{el} > 0 \end{cases}, \tag{7.8}$$

where the linear attenuation coefficients μ are subscripted by the material (water or bone) and superscripted by the associated energy (PET for 511 keV, CT for an effective energy). This method provides a continuous mapping from the CT HU value and the PET energy-specific linear attenuation coefficient. It can be expanded to allow for a trilinear fitting, where an additional condition is used to more precisely map bone structures.

When the ACFs are obtained using a CT acquisition, the resulting attenuation map has much better spatial resolution and sampling than PET images. Therefore, it is first down-sampled using interpolation methods to match the pixel size of the PET image. The spatial resolution of the resulting attenuation map is then matched to the PET spatial resolution using a blurring filter.

7.4/ RANDOM COINCIDENCES

The two photons that form a random coincidence are generated from two unrelated annihilation events. Random events add noise to the image affecting both the measured activity uptake and image contrast. The data acquired by PET systems can be written as:

$$R_{prompt} = R_{true} + R_{random} + R_{scatter}, \tag{7.9}$$

where R_{prompt}, R_{true}, R_{random}, $R_{scatter}$ are the prompt, true, random, and scatter coincidences count rates (see Section 3.4), respectively. According to this equation, it is possible to perform a random correction by simple subtraction. However, since random events cannot be precisely identified, they must be estimated. There are two common methods for estimating random counts. The first is based on the well-known relationship between the CTW width 2τ (see Section 3.4) and the single event rates between two detectors i and j (i.e. per LOR), denoted S_i and S_j, respectively:

$$R_{ij} = 2\tau S_i S_j, \tag{7.10}$$

where R_{ij} is the estimated randoms rate between detectors i and j. Because of its nature, this method is often called the single rate (SR) method. The single event rates S_i and S_j must be similar to the single event rates that can lead to coincidences, more specifically random coincidences. Therefore, the single rate obtained just before the coincidence processing (after energy discrimination) should be recorded and used. If SR is used to correct for random events, the prompt sinogram and the single event per detector must be recorded. Random correction is performed after data acquisition.

The second method is the delayed window (DW) method, which uses a second delayed coincidence window. The DW is defined with an arbitrary time delay from the prompt

CTW, and random coincidences are formed between these two windows. Because of the delay between the windows, it is impossible for the two photons used to form the random coincidences to have come from the same annihilation. By preventing the formation of true and scatter coincidences, the DW method can quantify the random count rate between each pair of detectors.

It is worth noting that single event rates are much higher than the coincidence event rates. Therefore, the random coincidence estimate provided by the SR method is less noisy than the DW random estimate. Both methods have been compared and improved over time (Casey et al., 1986; Stearns et al., 2003; Brasse et al., 2005; Torres-Espallardo et al., 2008; Oliver et al., 2010, 2016), and thanks to several variance reduction techniques developed for the DW method, the majority of contemporary PET systems use the DW to correct for random events.

7.5/ SCATTER COINCIDENCES

Properly separating scattered coincidences from true coincidences is not a trivial task (see Section 4.1.4), and a significant number of scatter correction methods have been proposed in the literature (Zaidi, 2000; Zaidi et al., 2007; Polycarpou et al., 2011). The most popular methods are model-based scatter correction (MBSC), based on single scatter simulation (SSS) (Ollinger, 1995; Watson et al., 1996, 1997; Watson, 2000), an analytical modelling of the physical process inducing Compton scattering (Watson et al., 1996). For the majority of detected scattered events, only one of the two annihilation photons undergoes a Compton interaction, and single-scatter events account for 75% of the scatter interactions occurring in the FOV (Zaidi et al., 2004). Therefore, MBSC methods compute the single-scatter distribution, and upscale it to model the multiple scatter events.

SSS methods require an attenuation map, often obtained from a CT acquisition (see Section 7.3), and an activity distribution map. Using SSS and an iterative reconstruction algorithm, such as OSEM, a scatter estimate is simulated at each iteration (except the first) and incorporated into the reconstruction process. The first iteration is performed without scatter correction and the obtained image estimate is then used as the activity distribution map (Iatrou et al., 2006; Zaidi et al., 2007). SSS does not estimate the correction of scatter events occurring outside the FOV, mostly caused by activity located outside the FOV and by inter-crystal scattering. Such events can be estimated by performing a short scan of the body parts expected to be outside the FOV, or by extrapolation of the activity map (Shao et al., 1996; Comanor et al., 1996; Wagadarikar et al., 2014; Zhang et al., 2019a).

With the advent of TOF-PET acquisitions, several methods have modified the scatter estimation to include a time distribution of scattered events (Werner et al., 2006; Iatrou et al., 2007; Watson, 2007; Conti et al., 2012). Watson et al. (Watson et al., 2018, 2020) extended their SSS algorithm to the double scatter simulation (DSS), taking into account for double scattered events. They showed that the combination of SSS+DSS accounts for almost all internal scattering on modern PET systems.

7.6/ DEAD TIME

To correct for dead time, it is common to use the scanner response in terms of single rate. A popular method uses a uniform cylinder filled with a very high activity, where data are acquired over a long duration, as the activity decays (Dönmez, 2017). At low activities, the measured single rate, denoted Sr_{obs}, can be considered to be free of dead time effects. These low-activity data can then be extrapolated to estimate the dead time free counting rates at higher activities, denoted Sr_{ext}. Subsequently, for a given activity and using a dead time model as defined in Section 4.3.1, the ratio Sr_{ext}/Sr_{obs} can be used to obtain the expected dead time influence. This value can then be used as the dead time correction factor. This process can be repeated for different desired activity levels, and the results can be stored in lookup tables. However, a system-wide measurement of Sr_{obs} may not accurately reflect the counting rate differences between detector blocks. This can be solved by acquiring Sr_{obs} and Sr_{ext} at the detector level, generating a lookup table per block to provide a finer estimate of the dead time correction.

Although this method is conceptually simple, it is not without limitations. Yamamoto et al. (1986) have shown that the dead time depends on the size of the object. In their work, Vicente et al. (2013) have emphasised that dead time or pile-up corrections estimated from the acquisition of a specific phantom may only be an approximation when applied to another object. They focused on the simultaneous study of pile-up and dead time effects, referred to as 'effective dead time'. Their research revealed a linear relationship between effective dead time and the singles-to-coincidences ratio (SCR). Using this relationship, they proposed a method involving two separate acquisitions, one at low SCR and the other at high SCR, to accurately estimate the pile-up and dead time corrections, respectively. The resulting correction was shown to be valid over a wide range of activity levels, accounting for the fact that each acquisition has a different effective dead time.

7.7/ POINT-SPREAD FUNCTION

In clinical PET imaging, the spatial resolution of the scanner is limited by several physical factors. They have been discussed in the following sections: 4.1.1 Positron range, 4.1.2 Non-collinearity, 4.2.1 Crystal dimensions, 4.2.2 Crystal scattering, and 4.2.3 Depth-of-interaction. According to the system matrix defined in Equation 7.1, these effects are included in H_{range} and H_{blur}.

The estimation and modelling of the spatial resolution of PET systems has been extensively studied (see reviews by Rahmim et al. (2013) and Iriarte et al. (2016)). A common method used to account for the effects of spatial resolution degradation is point spread function (PSF) modelling. With a PSF model, the spatial resolution correction can be preformed in projection space (on the acquired projection data), or in image-space (during or after image reconstruction). Since the PSF of PET systems is non-uniform and degrades from the centre of the scanner to the periphery of the FOV, the spatial resolution at each point of the FOV should be considered in the PSF model.

Ideally, the factors that degrades the spatial resolution of the system would be empirically determined, modelled, and then corrected. However, some of these effects are very difficult or almost impossible to measure (Panin et al., 2006), making purely empirical methods impractical. Several approaches have been proposed in the literature to

estimate the spatial resolution of the system: experimentally, from a set of point or line source measurements (Panin et al., 2006; Alessio et al., 2008; Tohme et al., 2009; Rapisarda et al., 2010); mathematically, using analytical models (Staelens et al., 2004; Rahmim et al., 2008); statistically, using MC simulations (Qi et al., 1998; Alessio et al., 2006); or by hybrid methods (Johnson et al., 1995; Yamaya et al., 2005). As there is no single solution to PSF modelling, the observed performance is highly dependent on design choices and implementation.

The limited spatial resolution of the system results in a phenomenon often referred to as partial-volume effect (PVE), where spillover between neighbouring structures of different activity leads to qualitative and quantitative errors in the reconstructed images. As shown in Figure 7.2, for any small, high-activity source embedded in a low-activity background, PVE spreads the signal. Similarly, for small tumours, PVE can make the tumour appear larger and less aggressive than it actually is. PVE generally affects structures whose size is less than 2-3 times the FWHM of the system (Soret et al., 2007). There are no PVE correction methods directly implemented on clinical systems (for a review of PVE correction methods, see Bettinardi et al. (2014)), but PSF modelling mechanically helps to reduce this effect.

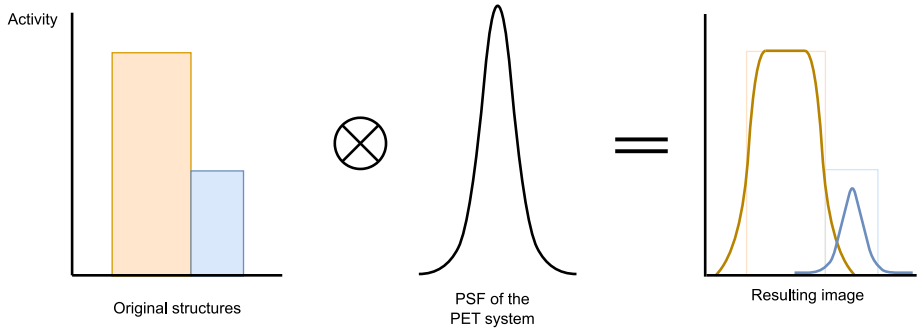

Figure 7.2: Illustration of the partial volume effect spillover between structures.

7.8/ DECAY

During a PET acquisition, the injected radiotracer will decay according to the decay constant, denoted λ:

$$\lambda = \frac{\ln 2}{T_{1/2}} \tag{7.11}$$

where $T_{1/2}$ is the half-life of the radionucleid. The activity measurement of the source is usually performed in a dose calibrator prior to administration to the patient. Knowing the calibration time, it is possible to calculate the decay-corrected activity at the start of the PET scan. Consider a known activity injection at time t_0 and a frame later acquired at time t_1 for a duration denoted Δt. The decay correction to the start of the acquisition, taking into account the decay before and during acquisition, denoted $C^{t_1}_{decay}$, is given by:

$$C^{t_1}_{decay} = \lambda \Delta t \frac{e^{\lambda(t_1 - t_0)}}{1 - e^{-\lambda \Delta t}} \tag{7.12}$$

7.9/ WELL-COUNTER

Up to this point, the reconstructed images reflect the relative concentration of the radiotracer in the scanned object in counts per second (*cps*). The absolute concentration of the radiotracer is needed to quantitatively characterise the amount of radionuclide that has been concentrated in a particular region of the object.

A calibration acquisition, called a well-counter calibration (WCC), can be performed to find the proportionality factor needed to obtain quantitative PET images in $kBq.mL^{-1}$. A uniform cylinder is filled with water, and a known activity is injected into the phantom. To accurately quantify the activity concentration in the phantom, the calibrated activity should be corrected for residual activity in the syringe or injector. The phantom is then imaged and the acquired data are reconstructed with all the available corrections. The radioactivity concentration in the central part of the phantom is then correlated with the reading from the dose calibrator (corrected for decay), and the calibration factor between *cps* and $kBq.mL^{-1}$ is extracted. This correction can be used directly in the reconstruction process or *a posteriori* on the reconstructed images.

8

Motivation of the thesis

PET is a nuclear imaging technique that provides functional information about the object being imaged. It is a medical and research tool used in both preclinical and clinical settings. It exploits the properties of radionuclides that decay by emitting positrons ($\beta+$) (Chapter 2). The instrumentation of a PET system is complex. PET detectors placed around the object being scanned convert photons into an electronic signal that is further processed into coincidence events (Chapter 3). However, the events acquired by PET systems are subject to biases induced by the physics of positron emission, and by the detection method itself (Chapter 4). The acquired data are organised into appropriate data structures (Chapter 5) so that they can be fed into reconstruction algorithms with appropriate corrections to obtain a quantitative PET image (Chapter 6). Over time, many correction methods have been developed to account for the various biases present in the acquired data (Chapter 7).

Nevertheless, PET imaging continues to evolve, as the last few decades have shown. The most notable advances are the use of Time-of-flight information, the Point-spread function correction, the switch from PMTs to Silicon photomultipliers, and the production of long axial FOV systems. A more recent development (enhanced by the advent of long axial FOV PET) is whole-body dynamic PET imaging, where multi-pass multi-bed PET data can be acquired to provide additional temporal information compared to current clinical protocols. Using this acquisition mode, tracer kinetics can be acquired at the voxel level and used to generate parametric images using kinetic modelling. Research is ongoing to improve reconstruction algorithms and correction, reduce system costs, optimise instrumentation, and improve patient safety and comfort through lower doses and shorter scans. Such research often represents a significant financial investment. Not all research groups have regular access to a clinical PET system, and the purchase of a dedicated research PET system is out of reach for the majority of research laboratories, especially for systems equipped with the latest technologies. For research carried out by PET system manufacturers, the immobilisation of prototypes, new detector materials, or structures can also lead to high financial expenditure.

The design, optimisation, and understanding of PET systems can be facilitated by the use of simulators. In nuclear medicine, simulators were initially used by manufacturers to design and optimise new PET systems. Outside an industrial environment, simulations have also been recognised as a valuable tool for a number of applications: evaluation of image reconstruction algorithms, correction techniques, dosimetry, and pharmacokinetic modelling (Zaidi, 1999). They also offer more flexibility than could be achieved with physical phantoms (Buvat et al., 2006), and require fewer resources and less cost. MC-based simulators are considered the gold standard in nuclear medicine because

they can adequately model the physical processes that occur during radiation transport in media (Rogers, 2006). Among the various MC simulators, Geant4 Application for Tomographic Emission (GATE) (Jan et al., 2011) is a well-known simulation toolkit based on Geant4, historically developed for nuclear imaging with specific layers for modelling sources, detection geometries, and detector electronic responses. GATE has been successfully used to validate the performance of several existing PET systems and to study the impact of different detector designs (Salvadori et al., 2020; Simon et al., 2004; Schmidtlein et al., 2006; Lamare et al., 2006; Delso et al., 2009; Sheen et al., 2014; Lu et al., 2016; Li et al., 2017; Kowalski et al., 2018; Teimoorisichani et al., 2019).

Once validated, the MC model of a PET system can be used to obtain various PET data. In recent years, deep learning (DL) has been successfully applied in medical imaging for image classification, segmentation and denoising tasks (Cai et al., 2020; Han, 2021). For medical imaging applications such as classification, segmentation, and denoising, the main challenge of DL is the need for large datasets. A MC model can be used to generate such datasets, enabling the design and training of DL architectures for PET imaging. One application could be the denoising of PET data for techniques such as dynamic imaging. Initiated in 2004 at the CGFL, the clinical research protocol TREN[1] aims to improve the value of PET imaging during neoadjuvant chemotherapy for newly diagnosed breast cancer patients. In this protocol, dynamic first-pass acquisitions are systematically performed to extract tumour blood flow. As these clinical data are extremely noisy, a Gaussian filter is often used to reduce the noise in the reconstructed PET image. However, such a filter can smooth out important structures in the image and affect quantification. The joint use of a denoising DL architecture and a MC model could provide an alternative method for denoising PET images. For data acquired during the TREN protocol, it could replace the Gaussian filtering of the images, potentially improving image-based analyses.

In July 2017, the CGFL became the first French establishment to be equipped with a digital PET/CT scanner: the Discovery MI (DMI) scanner, manufactured by GE HealthCare (GE HealthCare, Chicago, Il, USA). The purchase of this system was accompanied by a research collaboration agreement between GE HealthCare and the Nuclear Medicine department of the CGFL, which led to this thesis. The availability of a PET system equipped with the latest technological improvements (TOF, SiPMs) and the collaboration with the manufacturer was an opportunity to participate in research efforts aimed at improving PET imaging. At the beginning of this work (November 2019), no MC model of the DMI was proposed in the literature. In this thesis work, we aim to provide a complete MC model for the 4-ring DMI scanner, with the long-term view of obtaining a tool to improve image quality. The validation of the model is carried out according to the NEMA standard, including tests related to the image reconstruction of the simulated data and to the study of the TOF capabilities of the system.

[1] Tomographie par émission de positons au 18F-FDG pour évaluer précocement la REponse au traitement Néoadjuvant des cancers du sein.

II

CONTRIBUTIONS: DESIGN AND VALIDATION OF A MONTE CARLO MODEL OF THE GE DMI

9

CHARACTERISATION OF THE GE DMI 4-RING PET/CT SCANNER

The NEMA NU 2 standard, formally titled ”Performance Measurements of Positron Emission Tomographs”, is a widely recognised standard developed by the National Electrical Manufacturers Association (NEMA) consortium which specifies procedures for evaluating and reporting the performance characteristics of PET scanners. By providing standard guidelines, it aims to ensure consistency and comparability of performance measurements across different PET systems. This consistency allows practitioners, researchers, and manufacturers to evaluate and compare the capabilities of different PET scanners. PET manufacturers often provide a system-specific manual on how to perform the NEMA tests on their system (indicating procedures and recommendations), and a toolbox to perform the NEMA analyses. In its latest version, the NEMA NU 2-2018 codifies the measurement of various aspects of PET scanner performance, including sensitivity, count rate performance, spatial resolution, image quality, accuracy of corrections, and TOF resolution. It also provides guidelines for evaluating the accuracy of PET/CT co-registration. The aim of this chapter is fourfold: 1) to introduce and define the metrics commonly used to characterise PET systems; 2) to evaluate the performance characteristics of the General Electric (GE) 4-ring DMI scanner, using the tools provided by the manufacturer; 3) to compare our performance results with those available in the literature; and 4) to develop and validate our own performance analysis tool using the experimental data.

9.1/ 4-RING DMI SCANNER: INSTRUMENTATION AND DATA RECONSTRUCTION

The DMI is a SiPM-based PET/CT scanner manufactured by GE HealthCare (GE HealthCare, Chicago, Il, USA). It has a modular digital detector design in which three to six PET detector rings can be axially stacked to provide axial FOVs of 15 to 30 centimetres (5 cm per ring). A DMI with an axial FOV of 20 cm would therefore be referred to as a 4-ring DMI scanner, or DMI4 scanner for short.

DMI systems combine a TOF-capable PET tomograph and a multi-slice CT scanner. Table 9.1 summarises the geometric characteristics for a single PET ring of a DMI scanner. The PET ring diameter is 744 mm for a transaxial FOV of 700 mm, and the CTW width for the DMI4 is 4.9 ns. Energy discrimination is performed using an energy window, with lower and upper energy thresholds at 425 and 650 keV, respectively. A technological feature of this PET scanner is the compton scatter recovery (CSR) (Wagadarikar et al., 2014). This algorithm uses inter-block information to track events when an annihilation photon Compton scatters between adjacent blocks. Events for which the summed energy falls within the defined energy window are recovered. It has been shown that CSR improves the sensitivity of the system by 20% (Wagadarikar et al., 2014).

Table 9.1: Geometric characteristics of the 4-ring DMI scanner. For the SiPM array, only the active area (transaxial $\times$ axial) is given.

Structure	Contains	Size (transaxial x axial x length)	Number per ring
Crystal	LYSO	$3.95 \times 5.3 \times 25$ mm^3	4896
Block	4×9 crystals	$15.8 \times 47.7 \times 25$ mm^3	136
Module	4×1 blocks	$64.5 \times 47.7 \times 25$ mm^3	34
SiPM array	2×3 SiPM	12×12 mm^2	408

The DMI4 scanner can operate in 3D acquisition mode (see Section 5.1), and the data are stored in 3D sinograms of dimensions 415 (radial bins) $\times$ 1261 (planes) $\times$ 272 (projections). In the case of a 3D acquisition with TOF information, the 3D+TOF sinogram dimensions are 1261 (planes) $\times$ 29 (time) $\times$ 415 (radial bins) $\times$ 272 (projections). In addition, the data can be stored in list-mode, where the timestamp, energy, and detector identifiers are recorded for both photons of all coincidences. When time information is recorded, the acquisition is performed with a time sampling of 13.02 ps, and then the data are mashed by a factor of 13. The resulting sampling ($13 \times 13.02 = 169.26$ ps) does not penalise the reconstruction of TOF data (the Nyquist–Shannon sampling theorem is respected), since $1/169.26 \geq 2 \times 1/385$, where 385 is the temporal resolution (in ps) given in the manufacturer's datasheets for the DMI4 scanner GE Healthcare (2016b).

Reconstruction of PET data is performed using a proprietary offline reconstruction package implemented in MATLAB, hereafter referred to as the PET toolbox (GE HealthCare, Chicago, Il, USA). It includes reconstruction algorithms such as FBP, FORE, OSEM and Q.Clear, an implementation of the BSREM algorithm (Ross, 2014). Several correction methods are provided within the PET toolbox: normalisation, decay, WCC, attenuation (from CT data), deadtime, random (implementation of the SR method called randoms from singles (RFS)), and scatter (SSS method) corrections (Stearns et al., 2003; Iatrou et al., 2004, 2006; Polycarpou et al., 2011). In addition, iterative reconstructions can

incorporate TOF information and PSF modelling. Table 9.2 presents the three sets of reconstruction parameters used in this work. The VPFX parameter sets describe a TOF-OSEM reconstruction, where VPFX-DEF is the manufacturer's recommended set for the NEMA image quality standard. The VPFX-CLIN parameters are chosen to be identical to those used in clinical TOF-OSEM reconstructions of patient data. The VPHD set has been chosen to perform the NEMA accuracy of corrections test.

Table 9.2: Parameters of the VPHD, VPFX-DEF and VPFX-CLIN reconstructions.

Reconstruction name	VPHD	VPFX-DEF	VPFX-CLIN
Reconstruction algorithm	OSEM	OSEM	OSEM
TOF information	No	Yes	Yes
PSF correction	No	No	No
Iteration number	2	4	2
Subset number	34	34	17
Transverse filter type	Gaussian	Gaussian	Gaussian
Filter size (mm, FWHM)	5.0	2.0	6.4
3-point Z-filter	Heavy (2)	No	Medium (4)
Matrix size (pixel)	$128 \times 128 \times 66$	$384 \times 384 \times 71$	$256 \times 256 \times 71$
Pixel size (mm)	$1.04 \times 1.04 \times 2.79$	$1.04 \times 1.04 \times 2.79$	$2.73 \times 2.73 \times 2.79$
Transverse FOV size (mm)	180	400	700

9.2/ DMI PERFORMANCE EVALUATION

Measurements of the performance characteristics of the DMI scanner were carried out in 2017, 2020, 2021 and 2022 by the senior physicist of the Nuclear Medicine Department of the CGFL. Data acquisition was performed according to the manufacturer's guidelines, in compliance with the NEMA standard. These data were then analysed using the tools provided by the manufacturer, hereafter referred to as the "GE console", which is a MATLAB implementation of the NEMA NU 2-2012 standard. The implementation details of the NEMA tests in the GE console are not available.

In order to be independent of the NEMA analysis tool provided by the manufacturer, a software called **NE**MA **A**nalysis **T**ool (NEAT) was developed from scratch during this thesis. The analyses were implemented in NEAT according to the NEMA NU 2-2018 guidelines. Although the core of NEAT is written in Python, it is interfaced with code in other languages for specific NEMA-related tasks, in particular C++ for image analysis and segmentation using the Insight Toolkit (ITK).

Two components of NEAT are used in this chapter: the NEMA analysis methods and the data management interface called *SinoGenerator*. This interface, developed in Python, is based on look-up-tables (LUTs) provided by the manufacturer under a non-disclosure agreement (NDA), which link the axial and transaxial crystal indices of the DMI4 detectors to a 3D sinogram bin. The *SinoGenerator* can generate: a RFS sinogram from the experimental singles per detector; 3D and 3D+TOF sinograms from an experimental list-mode, and a SSRB sinogram from an experimental 3D sinogram. It was validated against the

expected sinograms obtained using the manufacturer's tools[1].

The raw acquisition data from each experiment were stored in Hierarchical Data Format (HDF) files (one file per frame). This format allows the storage of heterogeneous data (sinograms, injection time, acquisition parameters, etc.), and its structure is defined by the manufacturer. These files were used to analyse the data from each experiment with both the GE console and NEAT. In the following sections, all the methodology related to the NEMA analysis is described as implemented in NEAT. This software has been validated by comparing the produced NEMA analysis results with those of the GE console. The validation results are presented in Section 9.3, alongside the experimental results. When necessary, random sinograms were generated using the RFS method implemented in NEAT from the single event rates contained in the HDF files.

9.2.1/ Sensitivity

9.2.1.1/ Aim and associated metrics

The sensitivity of a PET system, denoted S, represents its ability to detect true coincidence photons. It is mainly determined by the solid angle of coverage of the imaged object and by the detection efficiency, denoted ϵ, of the system. The detection efficiency of a detector can be expressed as:

$$\epsilon = 1 - e^{-\mu_{\text{det}} x}, \tag{9.1}$$

where μ_{det} is the linear attenuation coefficient of the detector material (see Section 4.1.3) and x is the detector thickness encountered. In a PET system, since the recorded events are energy-discriminated, only a fraction of the detected events are retained. Therefore, Equation 9.1 can be modified as follows:

$$\epsilon = (1 - e^{-\mu_{\text{det}} x})\omega, \tag{9.2}$$

where ω is the fraction of events remaining after energy discrimination (with $\omega \in [0, 1]$). Since coincidences require the detection of two events, the detection efficiency of coincidences is given by ϵ^2, the probability of detecting the two annihilation photons.

For a point source placed at the centre of the FOV, the maximum geometric efficiency, denoted $\mathrm{H}_{\text{geom}}^{\text{CFOV}}$, is expressed as:

$$\mathrm{H}_{\text{geom}}^{\text{CFOV}} = \frac{\mathrm{A}_{\text{det}}}{4\pi \mathrm{R}^2}, \tag{9.3}$$

where R is the distance between the point source and the detector, i.e. the PET ring radius, and A_{det} is the area of the detector facing the source.

Finally, the sensitivity of a PET scanner for a positron-emitting point-source placed at the centre of the FOV and located in an absorbing medium of linear attenuation coefficient and total thickness denoted μ_{med} and T, respectively, can be expressed as follows:

[1] Only the RFS implementation in NEAT showed some slight differences compared to the experimental RFS sinogram. A relative difference of 0.5% was found between NEAT and GE console for the total random estimate, and up to 4% error across all bins of the sinograms.

$$S = H_{geom}^{CFOV} \epsilon^2 e^{-\mu_{med} T} \tag{9.4}$$

In practice, Equation 9.4 is more complex (Cherry et al., 2012). The detection efficiency may differ between pairs of detectors and will vary according to the position of the source in the FOV. In addition, the geometric efficiency depends on both the shape of the source and its position in the FOV.

9.2.1.2/ NEMA METHODOLOGY

Ideally, the sensitivity measurement would be made "in air", without any attenuating material. This would avoid the attenuation of the annihilation photon, thus avoiding count losses and the recording of scattered events caused by the presence of the absorbing medium. Under this condition, Equation 9.4 can be written as follows:

$$S = H_{geom}^{CFOV} \epsilon^2 \tag{9.5}$$

However, a significant amount of material is required to enable positron annihilation. In addition, this material attenuates the annihilation photons, leading to a bias in the measured count rate. The NEMA standard proposes the extrapolation of an absorber-free sensitivity from successive acquisitions made with a linear source of known activity and an absorber of known attenuation and varying thickness.

For each experiment, a 700 mm long line source with an internal diameter of 1 mm was filled with 2.9 ± 0.7 MBq of ^{18}F-FDG at the start of the acquisition[2]. The activity, denoted A_{cal}, was recorded at a time T_{cal} using a dose calibrator. This source was inserted into a 1.25 mm thick aluminium sleeve and placed in the centre of the transaxial FOV, aligned with the longitudinal axis of the scanner. Correct positioning of the source was ensured using a dedicated software provided by the manufacturer. The gantry required to support the source was placed outside the FOV (see Figure 9.1).

Five successive acquisitions were made, increasing the number of aluminium sleeves around the source for each acquisition, according to the dimensions given in Figure 9.2 and Table 8.3. The acquisitions were indexed by j, representing the number of aluminium sleeves ($j \in [\![1, 5]\!]$). For each acquisition, the start time T_j, the duration $T_{j,acq}$ (60 seconds for all acquisitions) and the number of counts were recorded. The acquired counts were organised into direct slices using SSRB (see Section 5.2.2.2), and the count rate $R_{j,i}$ was calculated for each slice i by dividing the number of counts in the slice i by the acquisition time $T_{j,acq}$. The values of $R_{j,i}$ were corrected for random counts using the SR method (see Section 7.4).

The global count rate R_j is given by the sum of all slices i of acquisition j ($R_j = \sum_i R_{j,i}$). Each R_j was corrected for radioactive decay before and during the acquisition to obtain $R_{corr,j}$, as follows:

$$R_{corr,j} = \frac{T_{j,acq} \ln 2 \cdot e^{\frac{T_j - T_{cal}}{T_{1/2}} \ln 2}}{T_{1/2} \left(1 - e^{\frac{T_{j,acq}}{T_{1/2}} \ln 2}\right)} R_j, \tag{9.6}$$

[2] Average and standard deviation of our four experiments.

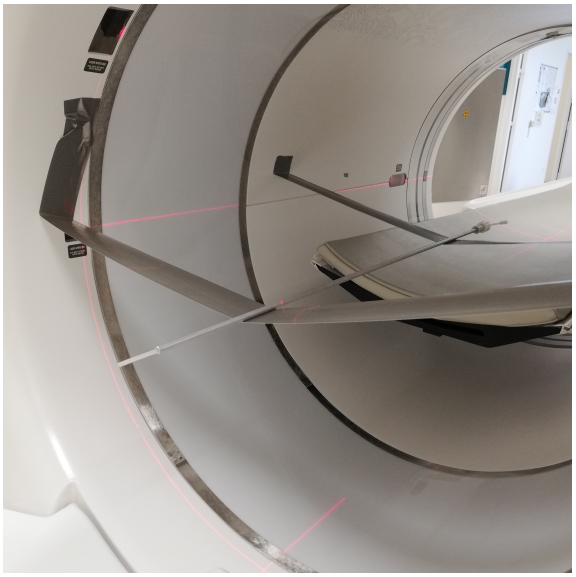

Figure 9.1: Image of an experimental NEMA sensitivity acquisition performed at the CGFL. The line source was placed in one aluminium sleeve, and the support gantry was placed outside the FOV.

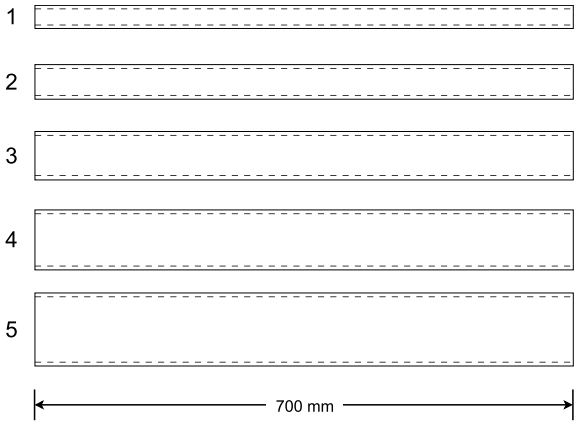

Sleeve number	Inside diameter (mm)	Outside diameter (mm)
1	3.9	6.4
2	7.0	9.5
3	10.2	12.7
4	13.4	15.9
5	16.6	19.1

Figure 9.2 & Table 9.3: Illustration of the NEMA sensitivity measurement phantom (sagittal plane) and dimensions of each aluminium sleeve.

where $T_{1/2}$ is the half-life of the radionuclide. Using the five corrected activities, the attenuation-free count rate, denoted $R_{\text{corr},0}$, was obtained by fitting the measured data (least-square fit) according to:

$$R_{\text{corr,j}} = R_{\text{corr},0} e^{-\mu_M \cdot 2X_j}, \tag{9.7}$$

where X_j is the thickness of the accumulated aluminium sleeves (2.5 mm per sleeve), and μ_M is the attenuation value in metal. It is set as an unknown in the fitting process to compensate for a small amount of scattered radiation. The system sensitivity, denoted S_{tot}, was then calculated as the ratio of the attenuation-free count rate to the calibrated activity:

$$S_{tot} = \frac{R_{corr,0}}{A_{cal}} \tag{9.8}$$

This procedure was then repeated at a radial offset of 10 cm from the centre of the field-of-view (CFOV). Furthermore, the sensitivity of each slice, denoted S_i, was calculated for $j = 1$ (only the smallest aluminium sleeve) using the measured count rate R_1 at 0 cm radial offset as follows:

$$S_i = \frac{R_{1,i}}{R_1} S_{tot} \tag{9.9}$$

9.2.2/ Count losses and scatter fraction

9.2.2.1/ Aim and associated metrics

A PET system records a prompt coincidence rate R_{prompt}, which includes true, random, and scatter coincidences, denoted R_{true}, R_{random}, and $R_{scatter}$, respectively (see Equation 7.9). The presence of scatter and random events adds noise to the true coincidence rate. The NECR is commonly used to characterise the dependence between true, random, and scatter coincidences. In the case of a uniform phantom reconstructed with an analytical algorithm (FBP), it has been shown that there is a proportional relationship between the SNR on the image and the NECR (Dahlbom et al., 2005). Lets consider a real system in which the measurement of prompt coincidences would be corrected for random and scatter events. Then, the NECR can be defined as the equivalent count rate of an ideal system that would produce the same level of statistical noise as this real system. It is formulated as follows:

$$NECR = \frac{{R_{true}}^2}{R_{true} + R_{scatter} + kR_{random}}, \tag{9.10}$$

where k is a constant of value 1 or 2, depending on the noisiness of the random estimation. $k = 1$ is used for DW with variance reduction techniques and SR, while $k = 2$ is used for DW with the direct subtraction method (see Section 7.4). The value of the NECR is usually reported as a function of activity to identify the linearity range of the scanner. This function can be used to find the NECR peak, which represents the maximum SNR achievable in the acquired data for a given system. Any increase in activity beyond this point would be detrimental to the SNR.

The NECR is a metric often used to compare the performance characteristics of different PET systems. Since its evaluation is highly dependent on the source distribution and the attenuating material, the NECR of different systems can only be compared if highly standardised measurement guidelines are followed. To this end, the NEMA standards define a procedure based on the work of Strother et al. (1990).

9.2.2.2/ NEMA Methodology

A 700 mm-long linear source with a diameter of 3.2 mm was inserted into a polyethylene phantom with an outer diameter of 203 mm and a length of 700 mm. The line source was

placed at a radial distance of 45 mm from the centre of the phantom, in the source insert designed for this purpose. The source was filled with a solution of ^{18}F and the activity at the start of the acquisition, denoted A_{cal}, was between 719 and 791 MBq for all years. This activity allows the measurement of the peak noise equivalent count rate, denoted $R_{NEC,peak}$, and peak true count rate, denoted $R_{t,peak}$.

The phantom was placed on the patient's bed, parallel to the scanner axis, with the line source insert closest to the patient's bed (as shown in Figure 9.3).

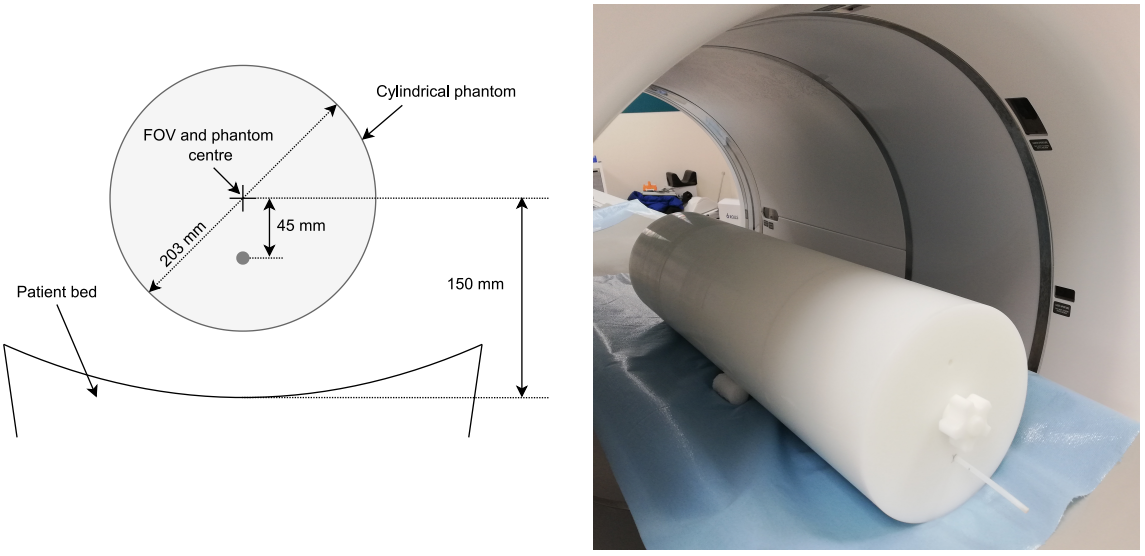

(a) **(b)**

Figure 9.3: (a) Illustration of the positioning of the cylindrical phantom according to the patient bed and to the system CFOV. **(b)** Image of the cylindrical phantom placed in the DMI4 scanner.

The patient bed was positioned 150 mm below the centre of the transverse FOV. The phantom was then centred on the FOV using positioning lasers to place the line source at 45 mm from the centre of the FOV. A total of 24 frames were acquired over ten hours: 17 contiguous acquisitions of 15 min, followed by seven acquisitions of 25 min, each separated by 25 min. Random events were estimated using the SR method ($k = 1$ in Equation 9.10). The resulting prompt and random 3D sinograms were first rebinned into 2D sinograms using SSRB. Then, for each 2D sinogram, all slices were summed to obtain a single slice. The analysis described below was applied to each single-slice sinogram of the 24 frames, but the frame index is not included in the following equations to make this rection easier to read.

All coincidences more than 120 mm from the transaxial axis of the scanner were removed from both prompt and random single-slice sinograms. Total event counts, denoted C_{tot}, and random counts, denoted C_r, were calculated as the respective sum of these sinograms. The centre of the line source response was determined for each projection by finding the maximum pixel value in the prompt sinogram. Using the location of this maximum, each projection was shifted to align the maximum with the centre of the radial axis of the sinogram (see Figure 9.4). The resulting aligned sinogram was then summed on the projection axis to obtain $C(r)$, a 1D profile of the coincidences arranged according to their distance from the line source response in millimetres, denoted r.

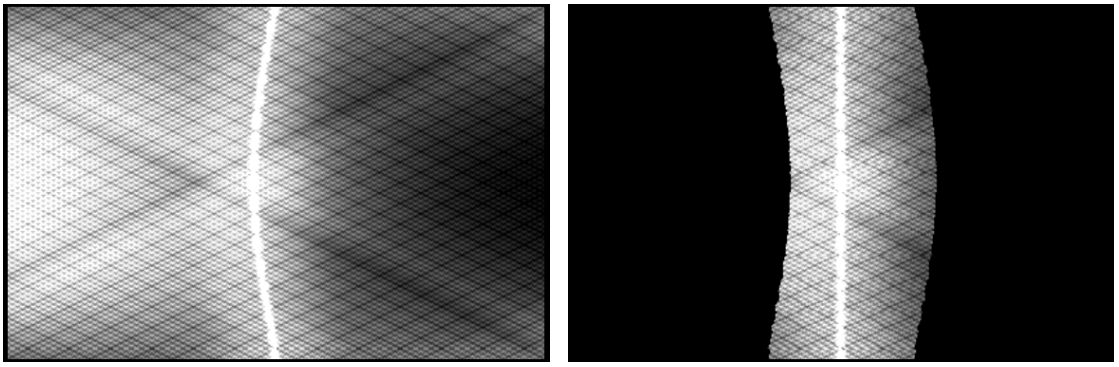

Figure 9.4: Line source shift during the NECR analysis, with **(a)** the original single-slice prompts and **(b)** the maximum-shifted line source with the 120 mm band applied.

Given the size of the line source and the shape of the phantom, it can be assumed that true coincidences can only occur within a 40 mm band centred on the line source. Therefore, any coincidence registered outside this 40 mm band is considered to be either a scatter or a random coincidence. However, as the profile is sampled in pixels, the edges of the band may not fall directly on a pixel centre, as shown in Figure 9.5. To overcome this, the counts per pixel at the left and right edges of the 40 mm band, denoted C_L and C_R, respectively, were obtained by linear interpolation using the pixels adjacent to the ± 20 mm marks (shown in red). The pixels containing the -20 mm and +20 mm marks are denoted P_L and P_R, respectively (outlined in bold font). The position of the band within these pixels is defined by continuous indices, denoted $P_{-20.0}$ and $P_{20.0}$ (represented by blue dots). The partial pixel counts of the left and right edges outside the band are denoted C_L^{out} and C_R^{out} (represented in green).

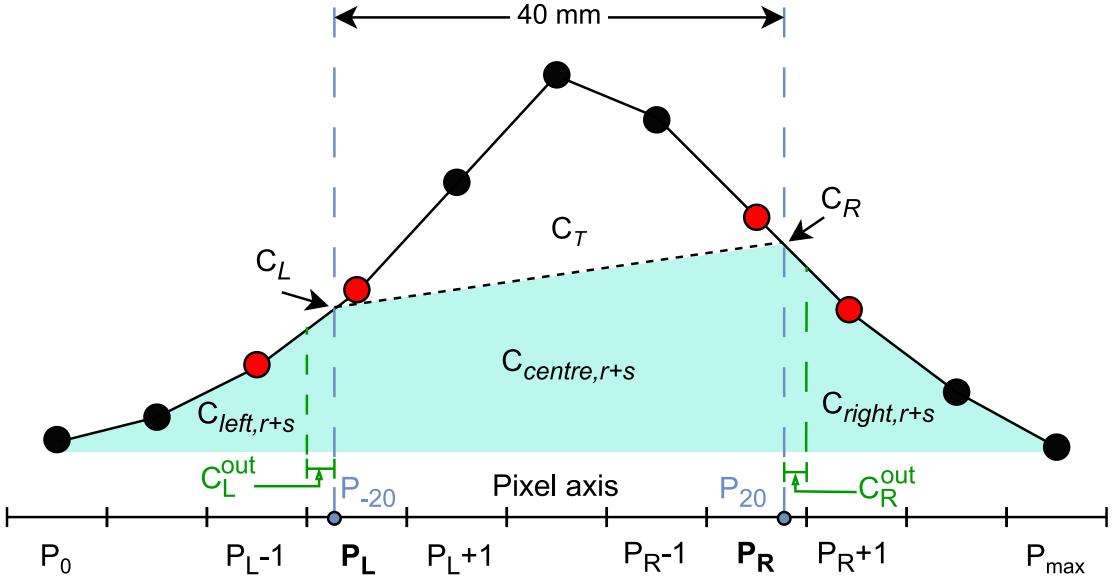

Figure 9.5: Illustration of the 1D profile of coincidences arranged according to their distance from the line source. A 40 mm band is placed around the maximum value, and the values for C_L and C_R are interpolated from the values of neighbouring pixels. The total random and scattered counts can then be estimated (in cyan).

The number of random plus scatter counts on the outer left part of the -20 mm edge, denoted $C_{left,r+s}$, can be calculated as:

$$C_{left,r+s} = C_L^{out} + \sum_{P=0}^{P_L-1} C(P) \tag{9.11}$$

Similarly, considering P_{max} as the rightmost pixel of the 1D profile, $C_{right,r+s}$ can be calculated as:

$$C_{right,r+s} = C_R^{out} + \sum_{P=P_R+1}^{P_{max}} C(P) \tag{9.12}$$

The random and scattered counts located within the 40 mm band, denoted $C_{centre,r+s}$, can then be obtained by calculating the area of the trapezoid defined by the values C_L, C_R, and the size of the band defined by the continuous index of the partial pixels:

$$C_{centre,r+s} = (C_L + C_R) \times (P_{20.0} - P_{-20.0})/2 \tag{9.13}$$

The total random and scatter counts C_{r+s} is defined as:

$$C_{r+s} = C_{left,r+s} + C_{centre,r+s} + C_{right,r+s} \tag{9.14}$$

Equation 9.14 is used to obtain the system scatter fraction, denoted SF, and the true and scatter event counts, denoted C_t and C_s, respectively:

$$SF = \frac{C_{r+s} - C_r}{C_{tot} - C_r} \tag{9.15}$$

$$C_t = C_{tot} - C_{r+s} \tag{9.16}$$

$$C_s = C_{r+s} - C_r \tag{9.17}$$

From the different event counts mentioned above, the respective count rates, denoted R, can be obtained by normalising by the duration of the frame. Finally, the NECR, denoted R_{NEC}, was calculated as follows:

$$R_{NEC} = \frac{{R_t}^2}{R_{tot}} \tag{9.18}$$

All calculated rates (including NECR) were calculated for each frame and reported according to the average activity, denoted A_{ave} of each frame starting at time T and of duration T_{acq}:

$$A_{ave} = A_{cal} \frac{T_{1/2}}{T_{acq} \ln 2} \exp\left(\ln 2 \frac{T_{cal} - T}{T_{1/2}}\right) \left[1 - \exp\left(\ln 2 \frac{T_{acq}}{T_{1/2}}\right)\right], \tag{9.19}$$

where A_{cal} is the source activity at the calibration time, and $T_{1/2}$ is the half-life of the radionuclide.

9.2.3/ SPATIAL RESOLUTION

9.2.3.1/ AIM AND ASSOCIATED METRICS

In Section 7.7, the various detrimental effects on spatial resolution were introduced, where a PSF can be used to describe the system response to a point source as a function of its position in the FOV. Assuming that all these effects have a Gaussian shape, we can calculate the spatial resolution of the system (FWHM in millimetres), denoted RS, as a function of the radial distance r of the source from the centre of the FOV Moses (2011):

$$\mathrm{RS} = C\sqrt{\left(\frac{d}{2}\right)^2 + s^2 + (0.0044R)^2 + b^2 + \frac{12.5r}{\sqrt{r^2+R^2}}}, \tag{9.20}$$

where d is the crystal width, s is the positron range, R is the radius of the scanner ring, b is the decoding factor. C is a multiplicative factor that is used to account for errors induced by the reconstruction algorithm. In the square root, the first term $(d/2)^2$ is due to the detector size (see section 4.2.1) and has the most significant impact on the spatial resolution of clinical PET systems. The second and third terms, s^2 and $(0.0044R)^2$ respectively, are related to the positron range (see section 4.1.1) and the photon non-collinearity (see section 4.1.2). Since the effects of these two terms cannot be reduced, they are considered fundamental limits of spatial resolution in PET. The fourth term b^2 is due to the optical multiplexing used for crystal identification (see section 3.3). In the case of a (1:1) coupling between photodetectors and crystals, this term is set to 0. The last term $12.5r/\sqrt{(r^2+R^2)}$ represents the error due to by the lack of information about the DOI (see section 4.2.3). The value of this term depends on the scintillation material used (BGO, LSO or LYSO crystals), and its effect is reduced by the use of DOI techniques. Finally, the global multiplicative factor C accounts for the sampling error induced by the non-uniform distribution of LORs in image space.

9.2.3.2/ NEMA METHODOLOGY

The methodology proposed in the NEMA NU 2-2018 standard was followed to characterise the intrinsic spatial resolution of the DMI4 scanner along its three axes (axial, radial, and tangential). A set of three ^{18}F-FDG point sources was placed at 1, 10, and 20 cm from the CFOV in the radial direction. To obtain point sources, capillaries were filled so that only one of their extremities contained the radiotracer solution. The source set was first positioned in the central transverse plane of the scanner, and then at an offset of three-eighths of the axial FOV, i.e. 76 mm from the CFOV. Each set position was imaged separately, and the correct source positioning was ensured using the alignment tool provided by the manufacturer (see Figure 9.6).

Image reconstruction was performed using the FBP algorithm provided in the PET toolbox, with a ramp filter and a cut-off at the Nyquist frequency (no smoothing). The reconstruction was centred on the sources with a transverse FOV of 250 mm to obtain a voxel size of $0.65 \times 0.65 \times 2.79$ mm^3.

For each of the six known point source positions, small region of interest (ROI) were used to find the location of the maximum pixel value. Using this maximum, three 1D profiles (one per scanner axis) were extracted for each of the six point source to determine their

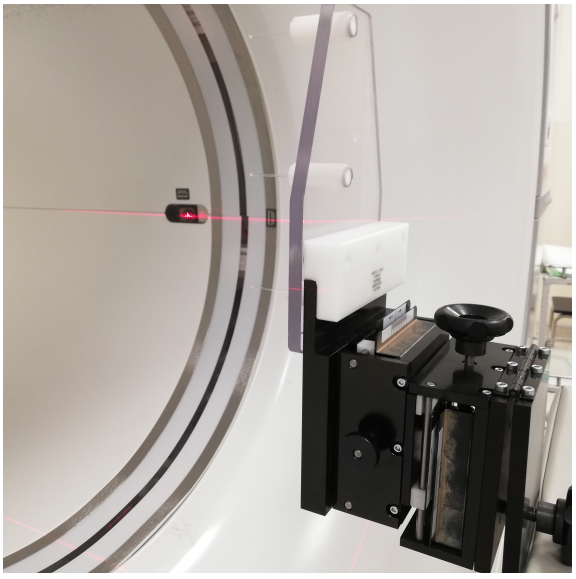

Figure 9.6: Image of the NEMA spatial resolution test performed experimentally on the DMI4 scanner at the CGFL. A set of three point sources is positioned using the patient bed and lasers.

3D response function. The response functions had radii of 10.73, 10.73 and 12.56 mm when set in the radial, tangential and axial directions, respectively. The peak value of each profile was determined using a three-point parabolic fit. The spatial resolution in each measurement direction was calculated in terms of FWHM and full width at tenth maximum (FWTM), in millimetres. Values were obtained by linear interpolation based on the two points adjacent to half and tenth of the maximum value.

9.2.4/ IMAGE QUALITY

9.2.4.1/ AIM AND ASSOCIATED METRICS

The assessment of image quality (IQ) in PET is a challenging task influenced by biological and physical factors. In addition, the IQ of PET images is highly dependent on the reconstruction algorithm and its parameters. The contrast recovery coefficient (CRC) can be used to quantify the contrast between high and low activity regions. In the NEMA 2018 report, the general formulation of the CRC, expressed as a percentage, is:

$$\mathrm{CRC} = \frac{\mathrm{C_{meas}} - 1}{\mathrm{C_{cal}} - 1} \times 100, \tag{9.21}$$

where $\mathrm{C_{meas}}$ is the measured contrast and $\mathrm{C_{cal}}$ is the expected contrast derived from the known activities in the phantom for the hot spheres and the background.

The NEMA 2018 report also defines background variability (BV) to quantify the variability between different background ROIs. Similarly, image roughness (IR) can be used as an additional metric (non-NEMA) to quantify the noise in all the background ROIs considered as a single large background region Tong et al. (2010). Both metrics are evaluated over K ROIs of the same size, each containing P pixels. The BV and the IR are expressed as

follows:

$$BV = \frac{\sqrt{\frac{1}{K-1}\sum_{k=1}^{K}(\mu_k - \overline{\mu_K})^2}}{\overline{\mu_K}} \tag{9.22}$$

and

$$IR = \frac{1}{K}\sum_{k=1}^{K}\frac{\sqrt{\frac{1}{P-1}\sum_{p\in ROI_k}(I_p - \mu_k)^2}}{\mu_k}, \tag{9.23}$$

where I_p is the intensity of the pixel p, and μ_k is the average value of all pixels inside the ROI k:

$$\mu_k = \frac{1}{P}\sum_{p\in ROI_k} I_p, \tag{9.24}$$

and $\overline{\mu_K}$ is the average of the ROIs means (μ_k) over all K ROIs:

$$\overline{\mu_K} = \frac{1}{K}\sum_{k=1}^{K}\mu_k \tag{9.25}$$

9.2.4.2/ NEMA METHODOLOGY

The image quality test was performed on the DMI using an International Electrotechnical Commission (IEC) body phantom containing four (NEMA NU 2-2012) or six (NEMA NU 2-2018) hot lesions in an activity-filled background. The lesions are represented by six spheres of 10, 13, 17, 22, 28 and 37 mm diameter. The background was filled with 5.3 ± 0.1 kBq.mL^{-1} of ^{18}F, and the activity of the hot sphere was chosen to give a sphere-to-background ratio (SBR) close to 4:1. The body phantom was centred in the FOV so that the centre of the spheres was in the central plane of the axial FOV. The noise equivalent count (NEC) phantom (see section 9.2.2) was placed on the patient's bed outside the imaging FOV, aligned with the body phantom (see Figure 9.7), and the line source was filled with approximately 120 MBq of ^{18}F. Three acquisitions were performed. To obtain the same number of counts for the three acquisitions, their duration was adjusted according to the decay of ^{18}F (see Section 7.8).

The acquired data were reconstructed using the VPFX-DEF reconstruction (see Table 9.2) with all available corrections except the PSF modelling (see Section 9.1). When this NEMA standard is performed with the GE console, the source and background ROIs have been placed automatically. However, if an error occurs during this process, the user can manually change the ROIs locations. The GE console is an implementation of the NEMA NU 2-2012 standard, where only the four smallest spheres are hot. The NEAT implementation of this NEMA analysis has been performed as described below.

Using the axial image slice passing through the centre of each sphere, a disc ROI was defined for each sphere. The centre of each ROI was set manually and the diameter of the ROI was set according to the inner diameter of the sphere in quesion. To account

Figure 9.7: Image of the NEMA IEC phantom on the DMI patient bed. The NEC phantom was placed on the patient bed outside the FOV.

for the discrete nature of the image, the discrete ROI was constructed so that the area of each ROI was as close as possible to the theoretical value obtained using the inner diameter of the sphere. The ROIs were then used to determine the average counts in each disc.

On this central slice, twelve 37 mm discs were manually positioned in the background, away from both the hot spheres and the phantom outer boundaries. Five concentric ROIs of diameters 10, 13, 17, 22 and 28 mm were placed in the centre of the twelve 37 mm ROIs. The resulting 12×6 ROIs were then duplicated on four axial slices located at -2, -1, $+1$, and $+2$ cm from the central slice. A total of 60 background spheres were defined per disk size. The average counts in each of these ROIs were calculated.

In NEAT, the placement of all ROIs (source and background) was constant over the three acquisitions of a given experiment. In addition, NEAT is an implementation of the NEMA NU 2-2018 standard, where all spheres are hot.

9.2.5/ Accuracy: corrections for count losses and randoms

9.2.5.1/ Aim and associated metrics

In Chapter 7, the corrections associated with PET image reconstruction were described in detail. Their accuracy is of paramount importance for obtaining quantitative PET images, and some become increasingly important with increasing activity (see Sections 7.4 and 7.6). The accuracy of corrections can be computed over a ROI placed at a location where the activity and source distributions are known:

$$\Delta r_{i,j} = \left(\frac{R_{ROI,i,j}}{\hat{R}_{i,j}} - 1\right) \times 100, \tag{9.26}$$

where, for all slices i of a frame j, $\Delta r_{i,j}$ is the correction accuracy (in percent), $\hat{R}_{i,j}$ is the expected true count rate, and $R_{ROI,i,j}$ is the reconstructed true count rate (corrected image).

9.2.5.2/ NEMA METHODOLOGY

This test uses the data obtained in the NECR test (see section 9.2.2.2). All 24 frames were reconstructed using the OSEM algorithm with the VPHD reconstruction parameter set, as defined in Table 9.2. All corrections (attenuation, normalisation, randoms, dead time, scatter) were applied, except the decay correction. The average activity of each frame j, denoted $A_{ave,j}$, was calculated according to Equation 9.19, and divided by the volume of the NEC phantom (about 22 000 mL) to obtain the effective activity concentration, denoted $A_{eff,j}$. A circular ROI of 180 mm diameter centred on the transverse FOV was defined on each slice of the reconstructed images to obtain the true count rate $R_{ROI,i,j}$ for each slice i of each frame j. The expected true count rate $\hat{R_{i,j}}$ was then extrapolated as:

$$\hat{R}_{i,j} = \frac{A_{ave,j}}{J} \sum_{k=1}^{J} \frac{R_{ROI,i,k}}{A_{ave,k}}, \tag{9.27}$$

where J is the total number of acquisitions below the peak NECR. The relative count rate error $\Delta r_{i,j}$ was then calculated using Equation 9.26, and reported as a function of the effective activity concentration $A_{eff,j}$.

9.2.6/ ENERGY AND TIMING RESOLUTIONS

9.2.6.1/ AIM AND ASSOCIATED METRICS

The energy resolution of a PET system is its ability to precisely measure the energy of the detected photons and therefore to distinguish scatter events from true events. It depends on several factors that cause amplitude variations in the detected energy, such as the light yield of the crystal and the QE of the photodetector. The energy resolution, denoted ΔE, is determined as the FWHM of the photopeak, denoted E_{FWHM}, expressed as a percentage of the expected energy (0.511 MeV in PET):

$$\Delta E = \frac{E_{FWHM}}{0.511} \times 100 \tag{9.28}$$

The upper threshold of the energy discrimination method is often chosen to be slightly higher than the photopeak energy plus the uncertainty introduced by the energy resolution of the system. This ensures that all photons depositing their complete energy are collected and also limits the number of piled-up events. For the lower threshold, the value chosen is often close to the photopeak energy minus the energy resolution error to limit the number of scatter events recorded.

The temporal resolution of a PET system is quantified by its CTR, which is its ability to precisely measure the TOF difference between two photons (see section 3.5). The CTR is influenced by the properties of the scintillation crystal, such as its decay time and photon

yield, and by the properties of the detection electronics, including the detection efficiency and the signal processing implementation (Gundacker, 2014). When considering a linear source placed along the axial axis of the scanner, the expected TOF difference between the two photons of a true coincidence is expected to be zero. Ideally, the data from this linear source should have minimal scatter and random rates (little attenuating medium and low activity) to maximise the prompt-to-true coincidence ratio. This ratio can be further improved by keeping only LORs passing though the source position. The resulting temporal information can then be histogramed, and the temporal resolution can be quantified as the FWHM of this histogram.

9.2.6.2/ METHODOLOGY

Measurement of energy resolution is not standardised by the NEMA guidelines. The time resolution measurement for the PET system has only been added in the latest NEMA NU 2-2018 report and is not implemented in the GE console[3]. In the absence of a standardised methodology, the energy and time resolution tests were performed according to the manufacturer's guidelines.

The analysis was carried out using the manufacturer's tools and is based on the work of Uribe et al. (2013). Both resolutions were evaluated using the sensitivity line source described in section 9.2.1. The line source was placed into a single aluminium sleeve and placed in the centre of the FOV, parallel to the scanner axis. The source was filled with a low-activity solution of ^{18}F, and the energy and time resolutions were calculated for each module of the PET system. For these tests, only the experiment of year 2020 is presented.

9.2.7/ STATISTICAL ANALYSIS

For readability of the following sections, the average (Avg), standard deviation (SD) and coefficient of variation (CV) ($\mathrm{CV} = \mathrm{SD}/\mathrm{Avg} \times 100$) of our experiments are mostly reported in the form "Avg ± SD (CV%)". For the NEMA Image quality standard, three acquisitions were made for each experiment. In this case, the SD was obtained by propagating the $\mathrm{SD}_{\mathrm{year}}$ of each experiment:

$$\mathrm{SD} = \sqrt{((\mathrm{SD}_{2017})^2 + (\mathrm{SD}_{2021})^2 + (\mathrm{SD}_{2022})^2)/3} \tag{9.29}$$

Our results were compared with those in the literature, where Hsu et al. (2017), Wagatsuma et al. (2017) and Chicheportiche et al. (2020) reported results of NEMA analyses obtained on four different DMI4 systems[4], analysed with the GE console provided with their system. For a given metric M, this comparison is expressed as the relative difference (%), denoted RD, between our value, denoted $\mathrm{M}_{\mathrm{ref}}$, and a value from the literature, denoted $\mathrm{M}_{\mathrm{study}}$:

$$\mathrm{M}_{\mathrm{RD}}(\%) = \frac{\mathrm{M}_{\mathrm{study}} - \mathrm{M}_{\mathrm{ref}}}{\mathrm{M}_{\mathrm{ref}}} \times 100 \tag{9.30}$$

[3] See Chapter 11 for the NEAT implementation of this standard.
[4] Hsu et al. (2017) reported NEMA analysis for two systems, one at Uppsala and one at Stanford.

These N values (one per result in the literature) were then averaged to obtain the mean relative difference between the literature data and our own, denoted $\mathrm{M_{RD,\mu}}$, and the standard deviation of the relative differences, denoted $\mathrm{SD_{RD}}$, was calculated.

The standard error of the mean (SEM), denoted $\mathrm{SEM_{RD}}$, was then calculated according to Equation 9.31, and the results were reported in the form "$\mathrm{M_{RD,\mu} \pm SEM_{RD}}$".

$$\mathrm{SEM_{RD}} = \frac{\mathrm{SD_{RD}}}{\sqrt{N}} \tag{9.31}$$

In addition, the following sections contain the validation results of NEAT. For each metric, the value calculated with NEAT ($\mathrm{M_{study}}$) is compared with the value obtained with the GE console ($\mathrm{M_{ref}}$) for year 2021 by means of relative difference (see Equation 9.30). The values obtained with NEAT for the year 2021 are used later in Chapter 10. Validation results for other years are available in Annex III.

9.3/ RESULTS

9.3.1/ NEMA SENSITIVITY

Table 9.4 contains the extrapolated values obtained for a zero-absorber sensitivity, for sources placed at the CFOV and at a radial offset of 10 cm. The results from the literature are reported, as well as the average of our four experiments (years 2017, 2020, 2021, and 2022). For a source at the CFOV, our experiments differed from the literature by 2.97± 2.18%.

Table 9.4: Mean sensitivity results (in cps/kBq) obtained over years for our experiments (evaluated with the GE console). Detailed results from the literature are also given (Hsu et al., 2017; Wagatsuma et al., 2017; Chicheportiche et al., 2020).

Source Position	Literature					This work	Relative difference (%)
	HSU Stanford	HSU Uppsala	Wagatsuma	Chicheportiche	Avg ± SD (CV%)	Avg ± SD (CV%)	$\mathrm{M_{RD,\mu} \pm SEM_{RD}}$
CFOV	14.00	13.40	12.62	13.30	13.33 ± 0.57 (4.24%)	12.95 ± 0.16 (1.22%)	2.97% ± 2.18%
10 cm radial offset	13.80	13.10	12.65	13.40	13.24 ± 0.49 (3.67%)	13.00 ± 0.16 (1.22%)	1.77% ± 1.87%

Regarding the validation results, Figure 9.8 shows the measured sensitivities for the year 2021, for all aluminium thicknesses, for a source placed at the CFOV (Figure 9.8a) and at a radial offset of 10 cm (Figure 9.8b), analysed with the GE console and NEAT. The relative difference between the GE console and NEAT system sensitivities was less than 0.01% for the year 2021.

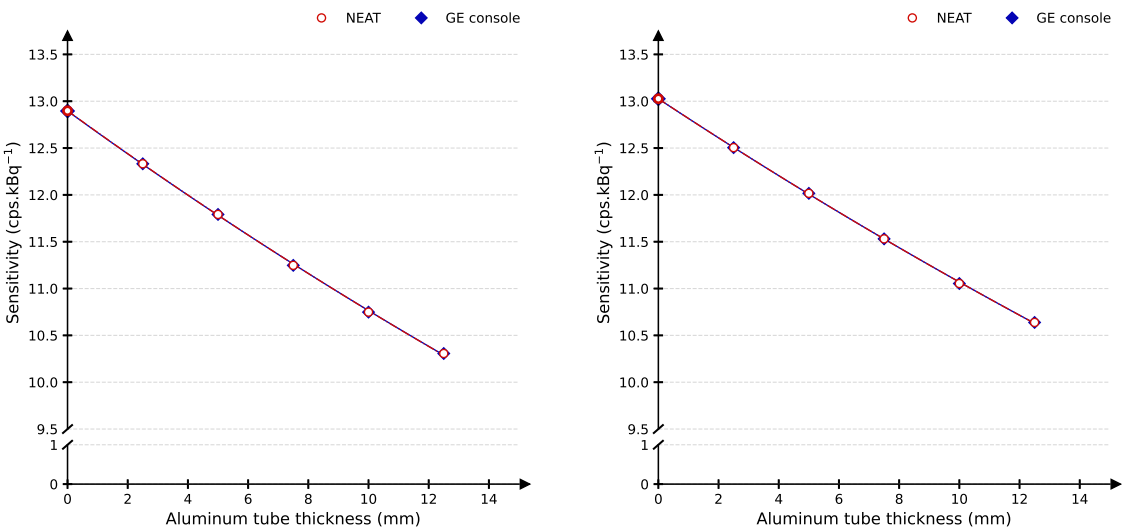

Figure 9.8: Comparison of sensitivity results for NEAT (in red) and the GE console (in blue) for the year 2021. In Figure **(a)**, the source has been placed at the CFOV. In Figure **(b)**, it has been placed at a radial offset of 10 cm.

Figure 9.9 shows the axial sensitivity profile for the year 2021 for a source placed at the CFOV, analysed with the GE console and NEAT. For this experiment, the maximum relative difference between the GE console and NEAT was 4.86% across all slices.

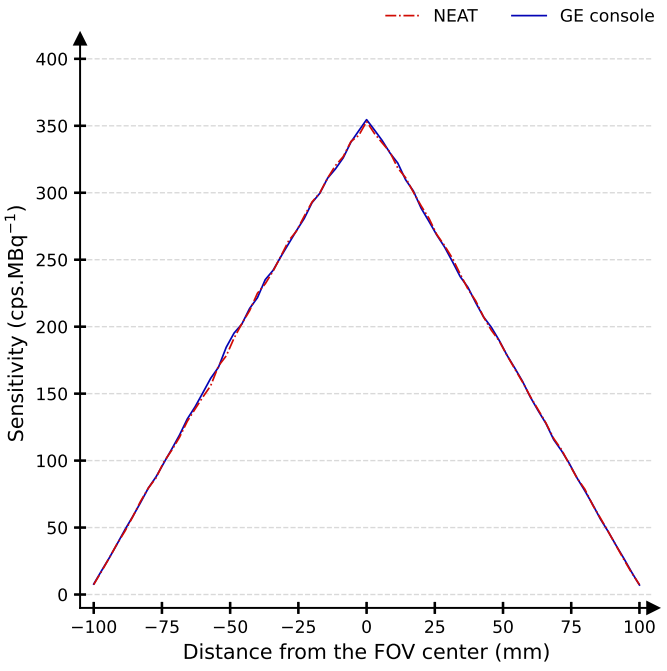

Figure 9.9: Comparison of axial sensitivity profiles obtained at the CFOV for NEAT (in red) and the GE console (in blue) for the year 2021.

9.3.2/ NEMA COUNT LOSSES AND SCATTER FRACTION

Table 9.5 shows the peak NECR value and activity, the peak true count rate value and activity, and the scatter fraction at the peak NECR for the years 2017, 2020, and 2021. When available in the literature, the values of these metrics have also been reported. The scatter fraction of our system was found to be slightly higher than that of the literature (-2.72± 0.93%). For all reported data, the peak true count rate was observed at an activity corresponding to the first frame of the acquisition.

Table 9.5: Metrics for the NEMA count losses and scatter fraction test. Detailed results of our experiments are reported for the years 2017, 2020, and 2021, as well as detailed data from the literature (Hsu et al., 2017; Wagatsuma et al., 2017; Chicheportiche et al., 2020).

Measurement	Literature				This work			Relative difference (%)
	HSU Stanford	HSU Uppsala	Chicheportiche	Wagatsuma	2017	2020	2021	$M_{RD,\mu} \pm SEM_{RD}$
NECR								
Peak (kcps)	201.1	185.7	185.6	175.6	184.0	174.6	168.9	6.38% ± 2.99%
Activity (kBq.mL^{-1})	22.1	21.7	22.5	20.1	22.6	23.5	23.5	−6.84% ± 2.27%
True count rate								
Peak (kcps)	875.9	827.0		789.2	812.7	787.3	743.0	6.36% ± 3.21%
Activity (kBq.mL^{-1})	35.4	34.8		35.5	33.0	34.3	31.2	7.32% ± 0.67%
Scatter fraction								
At peak NECR (%)	40.4	40.8	42.1	40.5	41.3	42.4	42.5	−2.72% ± 0.93%

The experimental count rates obtained using the GE console and NEAT for the year 2021 are shown in Figure 9.10. Figure 9.11 shows the same curves but with emphasis on activity concentrations within a clinical range (≤ 10 kBq.mL^{-1}). The NECR and scatter fraction are shown in Figures 9.12a and 9.12b, respectively. The prompt, random, scatter, true, and noise equivalent count rates obtained with NEAT and the GE console differed by a maximum of 2.52%, 3.20%, 3.65%, 0.28%, and 3.01%, respectively. With NEAT, the NECR peak was 164 kcps at 23.5 kBq.mL^{-1}, and the scatter fraction at this peak was 44.4%.

9.3.3/ NEMA SPATIAL RESOLUTION

Table 9.7 shows the detailed results from the literature (see Section 9.2.3.1) and the average values of our experiments calculated over the years 2017, 2020, 2021, and 2022. The FWHM and FWTM values have been averaged over both axial positions (CFOV and 1/8 of CFOV) for each experiment/result. Detailed values for each year are given in Annex A.3.

The maximum CV in our experiments was 6.03% for the axial FWHM with a source placed at a radial offset of 10 cm. A similar value (6.32%) was found in the literature for the same position. The largest average relative difference between our results and the literature was 4.14% FWHM in the tangential direction for a source placed at a radial offset of 10 cm.

Table 9.6 shows the validation of NEAT for the spatial resolution data obtained in 2021. The maximum observed relative difference was 6.38%, for the FWTM in the radial direction with a source placed at a radial offset of 10 cm.

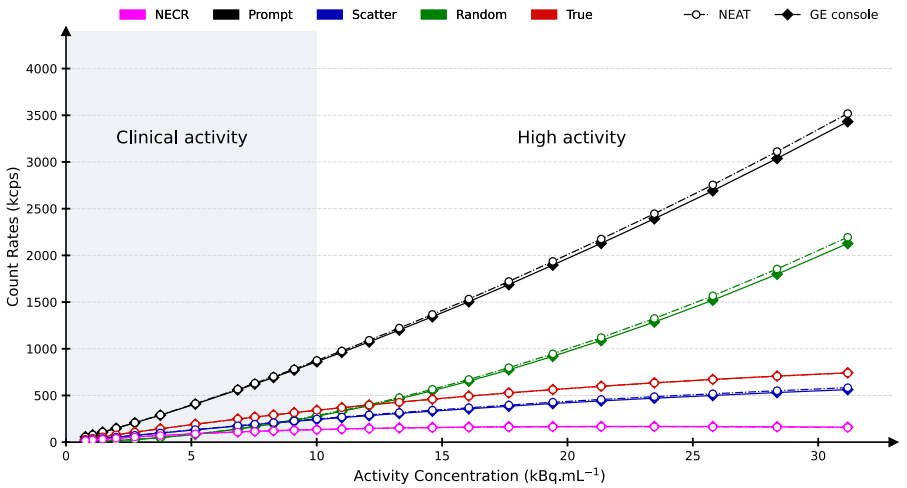

Figure 9.10: NEMA count losses test for the year 2021. Prompt (black), random (green), scatter (blue) and true (red) count rates (kcps) from the GE console (continuous) and from NEAT (dash-dotted) as a function of activity concentration (kBq.mL^{-1}). The NECR is shown in purple.

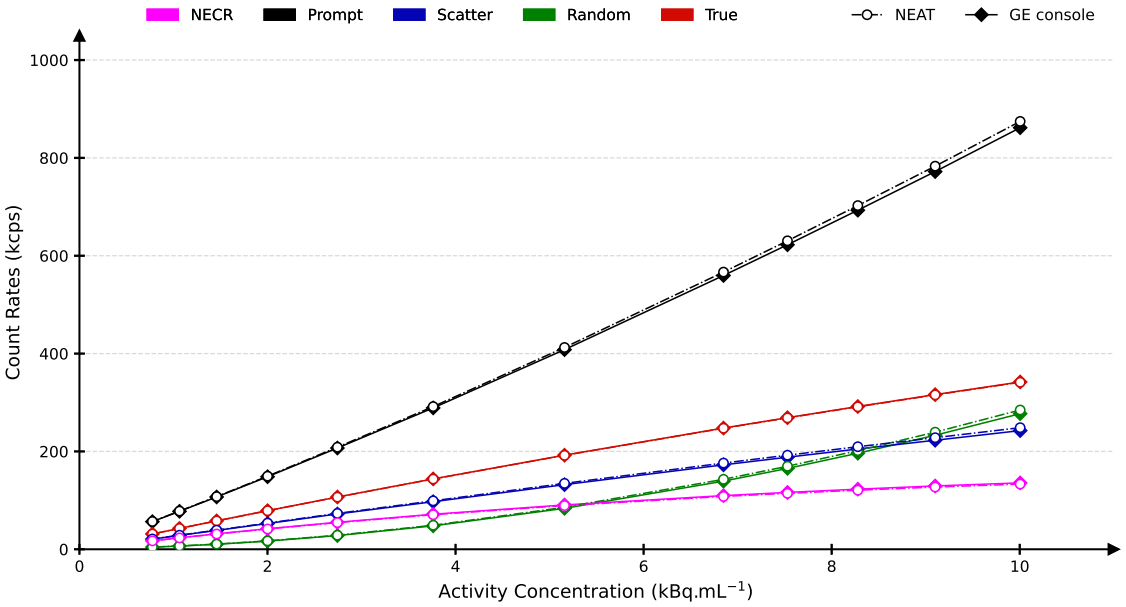

Figure 9.11: Focus on the clinical range ($\leq$ 10kBq) of the data shown in Figure 9.10. Prompt (black), random (green), scatter (blue) and true (red) count rates (kcps) from the GE console (continuous) and from NEAT (dash-dotted) as a function of activity concentration (kBq.mL^{-1}). The NECR is shown in purple.

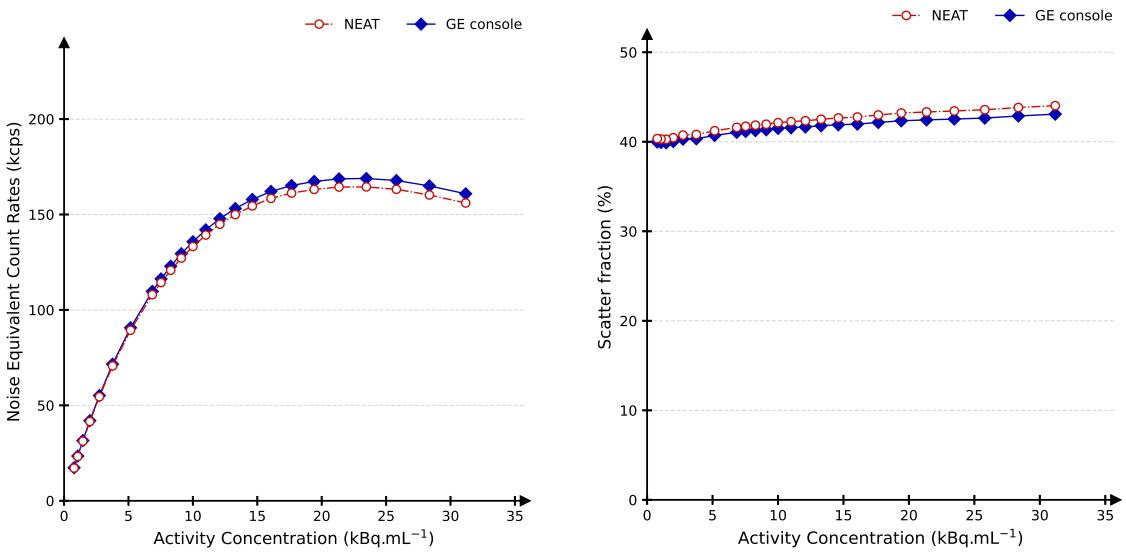

Figure 9.12: Comparison of the results between the GE console and NEAT using the experiment of the year 2021. Figure **(a)** shows the noise equivalent count rates in kcps, and Figure **(b)** shows the system scatter fraction expressed as a percentage, both as a function of activity concentration (kBq.mL^{-1}).

Table 9.6: Validation of NEAT against the GE console, using the experiment of the year 2021. The largest obeserved relative difference was 6.38%.

Resolution	**GE console**		**NEAT**		Relative difference (%)	
Direction	FWHM	FWTM	FWHM	FWTM	FWHM	FWTM
1 cm radial offset						
Radial	4.47	8.86	4.34	8.48	−2.91 %	−4.29 %
Tangential	4.29	8.57	4.17	8.20	−2.80 %	−4.32 %
Axial	4.63	10.29	4.49	10.07	−2.92 %	−2.09 %
10 cm radial offset						
Radial	5.58	10.65	5.67	11.33	1.70%	6.38%
Tangential	4.53	9.76	4.40	9.78	−2.76 %	0.26%
Axial	6.28	11.98	6.21	11.79	−1.04 %	−1.59 %
20 cm radial offset						
Radial	7.40	14.14	7.27	14.35	−1.76 %	1.49%
Tangential	5.18	9.72	5.10	9.88	−1.45 %	1.65%
Axial	6.27	12.24	6.29	12.45	0.40%	1.76%

Table 9.7: FWHM and FWTM (in mm) values for the NEMA spatial resolution test, averaged over both axial source positions. Average values (with SD and CV) of our experiments are reported. Detailed results found in the literature are also presented (Hsu et al., 2017; Chicheportiche et al., 2020).

Resolution Direction	Literature						This work		Relative difference (%)	
	HSU Stanford		HSU Uppsala		Chicheportiche		Avg ± SD (CV%)		Avg ± SD (CV%)		Avg ± SEM	
	FWHM	FWTM	FWHM	FWTM	FWHM	FWTM	FWHM	FWTM	FWHM	FWTM	FWHM	FWTM
1 cm radial offset												
Radial	4.17	9.14	4.02	8.52	4.62	8.95	4.27 ± 0.31 (7.31%)	8.87 ± 0.32 (3.58%)	4.38 ± 0.14 (3.10%)	8.91 ± 0.04 (0.50%)	−2.48% ± 4.12%	−0.41% ± 2.06%
Tangential	4.40	9.17	3.97	8.19	4.18	8.65	4.18 ± 0.22 (5.14%)	8.67 ± 0.49 (5.66%)	4.30 ± 0.06 (1.30%)	8.64 ± 0.09 (1.05%)	−2.63% ± 2.89%	0.36% ± 3.28%
Axial	4.57	10.38	4.39	10.12	4.57	10.42	4.51 ± 0.10 (2.30%)	10.31 ± 0.16 (1.58%)	4.55 ± 0.08 (1.81%)	10.24 ± 0.03 (0.32%)	−0.96% ± 1.32%	0.65% ± 0.92%
10 cm radial offset												
Radial	5.65	10.36	5.28	9.95	5.56	10.58	5.50 ± 0.19 (3.51%)	10.30 ± 0.32 (3.11%)	5.57 ± 0.02 (0.41%)	10.58 ± 0.06 (0.60%)	−1.34% ± 2.00%	−2.66% ± 1.75%
Tangential	4.74	9.68	4.23	8.83	4.69	9.32	4.55 ± 0.28 (6.17%)	9.28 ± 0.43 (4.60%)	4.66 ± 0.09 (1.89%)	9.46 ± 0.20 (2.15%)	−2.21% ± 3.49%	−1.89% ± 2.61%
Axial	6.39	12.34	5.63	11.80	6.05	11.70	6.02 ± 0.38 (6.32%)	11.95 ± 0.34 (2.88%)	5.90 ± 0.36 (6.03%)	11.78 ± 0.19 (1.63%)	2.18% ± 3.73%	1.44% ± 1.69%
20 cm radial offset												
Radial	7.52	13.88	7.54	13.38	7.39	14.23	7.48 ± 0.08 (1.09%)	13.83 ± 0.43 (3.09%)	7.42 ± 0.03 (0.43%)	14.18 ± 0.05 (0.38%)	0.87% ± 0.63%	−2.43% ± 1.74%
Tangential	5.13	10.14	4.67	9.04	5.08	9.28	4.96 ± 0.25 (5.09%)	9.49 ± 0.58 (6.10%)	5.18 ± 0.01 (0.16%)	9.64 ± 0.06 (0.58%)	−4.15% ± 2.82%	−1.57% ± 3.46%
Axial	6.50	13.01	5.70	12.57	6.05	12.00	6.08 ± 0.4 (6.59%)	12.53 ± 0.51 (4.04%)	6.12 ± 0.16 (2.63%)	12.14 ± 0.08 (0.63%)	−0.60% ± 3.78%	3.22% ± 2.41%

9.3.4/ NEMA IMAGE QUALITY

For this NEMA standard, experiments were carried out in 2017, 2021, and 2022 according to the NEMA NU 2-2012 standard (the 28 and 37 mm spheres were filled with non-radioactive water). The CRC, BV and lung error (expressed as percentages) are presented in Table 9.8 for all spheres and compared with those reported in the literature. For each result, the experiment consisted of three acquisitions (see Section 9.2.4.2) reconstructed with VPFX-DEF (see section 9.2). The values reported are the average, SD and CV of these three acquisitions. For our experiments, the mean results over the years were further calculated to obtain the column "Avg ± SD (CV%)" in Table 9.8, propagating the individual SDs (see Section 9.2.7).

With respect to CRC and BV measurements, and taking into account the uncertainties, the average of our experiments was in good agreement with the literature values. However, the lung error observed in our experiments was consistently lower (6.34%) than that reported in the literature (7.4%).

Another experiment was carried out in 2021, according to the NEMA NU 2-2018 report (all spheres were filled with radioactivity). The three acquisitions of this experiment were reconstructed using the VPFX-DEF and VPFX-CLIN reconstruction parameters (see Table 9.2), and analysed using both the GE console and NEAT. The corresponding results are presented in Table 9.9 and Figure 9.14, together with the VPFX-DEF results for the initial 2021 experiment (four hot spheres only). The IR evaluated with NEAT is also reported.

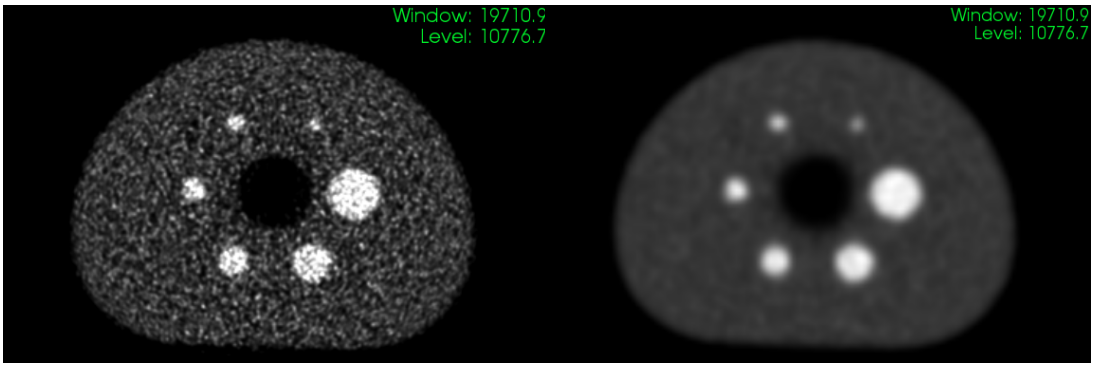

(a) **(b)**

Figure 9.13: Central slices of the reconstructed data of the IEC phantom using **a)** the VPFX-DEF reconstruction and **(b)** the VPFX-CLIN parameters (see Table 9.2).

For the VPFX-DEF reconstruction, the lung errors calculated in the GE console and in NEAT were 6.6% and 6.0% respectively. For the VPFX-CLIN reconstruction, lung errors calculated in the GE console and NEAT were 11.4% and 11.3%, respectively. Figure 9.13 shows the central slice of an acquisition reconstructed with VPFX-DEF (9.13a) and VPFX-CLIN (9.13b), respectively. It is clear from this figure that VPFX-DEF and VPFX-CLIN produce different levels of noise. This difference is particularly evident in the IR values of Table 9.9.

Table 9.8: Image quality results for our experiments (years 2017, 2021, 2022), and for Wagatsuma et al. (2017). The average, SD and CV are reported for CRC, BV, and lung error for each experiment and for each sphere size.

Sphere	**This Work**				**Literature**
diameter (mm)	2017	2021	2022	Avg ± SD (CV%)	Wagatsuma
			Contrast Recovery Coefficient (%)		
10	51.83 ± 3.29 (6.35%)	56.87 ± 4.20 (7.39%)	52.83 ± 2.71 (5.12%)	53.84 ± 3.45 (6.42%)	51.8 ± 3.5 (6.76%)
13	65.23 ± 6.31 (9.68%)	64.20 ± 3.22 (5.01%)	55.73 ± 5.41 (9.71%)	61.72 ± 5.15 (8.34%)	61.0 ± 1.9 (3.11%)
17	73.30 ± 2.91 (3.96%)	70.20 ± 2.17 (3.09%)	58.30 ± 2.36 (4.06%)	67.27 ± 2.50 (3.72%)	67.5 ± 4.0 (5.93%)
22	80.57 ± 2.95 (3.66%)	74.97 ± 2.05 (2.73%)	69.97 ± 4.83 (6.91%)	75.17 ± 3.48 (4.63%)	72.3 ± 3.7 (5.12%)
28	86.00 ± 0.87 (1.01%)	81.87 ± 0.74 (0.90%)	86.00 ± 1.28 (1.48%)	84.62 ± 0.99 (1.17%)	86.4 ± 0.4 (0.46%)
37	88.83 ± 1.85 (2.08%)	87.40 ± 0.53 (0.61%)	89.73 ± 0.76 (0.84%)	88.66 ± 1.19 (1.35%)	89.0 ± 2.0 (2.25%)
			Background Variability (%)		
10	10.07 ± 0.60 (5.99%)	10.67 ± 0.38 (3.55%)	11.53 ± 0.61 (5.30%)	10.76 ± 0.54 (5.04%)	9.7 ± 0.5 (5.15%)
13	7.57 ± 0.21 (2.75%)	7.43 ± 0.40 (5.44%)	8.90 ± 0.66 (7.37%)	7.97 ± 0.46 (5.78%)	7.4 ± 0.8 (10.81%)
17	5.53 ± 0.29 (5.22%)	5.70 ± 0.66 (11.50%)	6.77 ± 0.23 (3.41%)	6.00 ± 0.43 (7.24%)	5.6 ± 0.6 (10.71%)
22	4.53 ± 0.31 (6.74%)	4.37 ± 0.35 (8.04%)	4.97 ± 0.21 (4.19%)	4.62 ± 0.29 (6.37%)	4.3 ± 0.5 (11.63%)
28	3.73 ± 0.32 (8.61%)	3.53 ± 0.12 (3.27%)	3.60 ± 0.35 (9.62%)	3.62 ± 0.28 (7.75%)	3.6 ± 0.3 (8.33%)
37	2.93 ± 0.06 (1.97%)	2.63 ± 0.25 (9.56%)	2.70 ± 0.10 (3.70%)	2.76 ± 0.16 (5.80%)	3.0 ± 0.4 (13.33%)
			Lung Error (%)		
	6.47 ± 0.31 (4.72%)	6.43 ± 0.25 (3.91%)	6.13 ± 0.25 (4.10%)	6.34 ± 0.28 (4.46%)	7.4 ± 0.2 (2.70%)

Table 9.9: Validation of NEAT against the GE console using a NEMA NU2-2018 acquisition with all six spheres filled to achieve a 4:1 activity concentration with the background. CRC, BV, and lung error are reported for the VPFX-DEF and VPFX-CLIN reconstructions. The relative difference (%) is calculated for the CRC and BV obtained with the GE console and NEAT.

Sphere	**GE console**		**NEAT**			**Relative difference**	
diameter (mm)	CRC (%)	BV (%)	CRC (%)	BV (%)	IR (%)	CRC (%)	BV (%)
VPFX-DEF							
10	58.10 ± 7.98 (13.73%)	10.90 ± 1.42 (13.01%)	53.22 ± 7.11 (13.36%)	10.47 ± 0.51 (4.83%)	34.88 ± 0.88 (2.51%)	−8.40 %	−3.98 %
13	62.67 ± 0.72 (1.15%)	7.80 ± 0.82 (10.49%)	56.93 ± 4.15 (7.29%)	7.67 ± 0.48 (6.21%)	36.02 ± 0.69 (1.91%)	−9.16 %	−1.67 %
17	73.50 ± 3.70 (5.04%)	5.73 ± 0.70 (12.25%)	70.59 ± 2.55 (3.62%)	6.07 ± 0.79 (13.08%)	36.54 ± 0.38 (1.04%)	−3.95 %	5.93%
22	77.50 ± 1.42 (1.83%)	4.33 ± 0.47 (10.91%)	75.04 ± 1.59 (2.11%)	4.38 ± 0.30 (6.85%)	36.83 ± 0.43 (1.18%)	−3.17 %	1.15%
28		3.30 ± 0.36 (10.93%)	78.20 ± 3.69 (4.72%)	3.68 ± 0.22 (5.96%)	36.67 ± 0.30 (0.81%)		11.52%
37		2.57 ± 0.21 (8.11%)	81.45 ± 4.12 (5.06%)	2.60 ± 0.16 (6.19%)	36.63 ± 0.28 (0.75%)		1.30%
LE (%)	6.60 ± 0.00 (0.00%)			6.03 ± 0.33 (5.40%)		-8.69%	
VPFX-CLIN							
10	30.17 ± 1.55 (5.14%)	3.27 ± 0.06 (1.77%)	31.14 ± 1.64 (5.27%)	3.42 ± 0.36 (10.52%)	3.20 ± 0.21 (6.59%)	3.24%	4.80%
13	45.10 ± 0.52 (1.15%)	2.87 ± 0.12 (4.03%)	41.00 ± 0.35 (0.86%)	2.90 ± 0.36 (12.33%)	3.68 ± 0.23 (6.25%)	−9.10 %	1.28%
17	57.90 ± 2.95 (5.10%)	2.37 ± 0.12 (4.88%)	57.86 ± 2.65 (4.59%)	2.39 ± 0.25 (10.53%)	4.05 ± 0.18 (4.56%)	−0.07 %	0.99%
22	66.30 ± 0.89 (1.34%)	1.97 ± 0.12 (5.87%)	65.12 ± 0.79 (1.21%)	1.97 ± 0.16 (7.93%)	4.31 ± 0.12 (2.88%)	−1.78 %	0.17%
28		1.63 ± 0.15 (9.35%)	70.67 ± 0.55 (0.78%)	1.66 ± 0.06 (3.87%)	4.43 ± 0.08 (1.76%)		1.84%
37		1.33 ± 0.12 (8.66%)	77.55 ± 0.83 (1.06%)	1.35 ± 0.01 (0.86%)	4.52 ± 0.07 (1.57%)		1.00%
LE (%)	11.43 ± 0.12(1.01%)			11.30 ± 0.13(1.19%)		-1.14%	

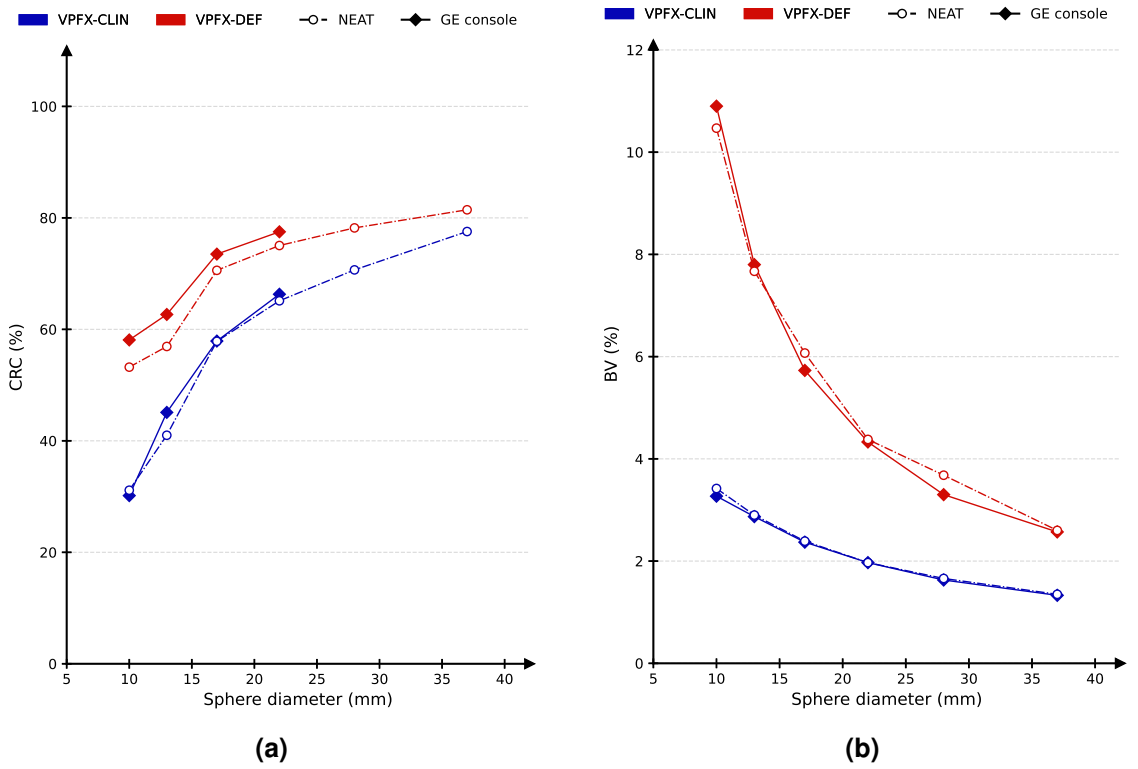

Figure 9.14: Comparison between **(a)** the CRC and **(b)** the BV obtained with the GE console (continuous) and NEAT (dash-dotted) for the NEMA image quality test, using data obtained in 2021. The data data were reconstructed using the VPFX-DEF (red) and VPFX-CLIN (blue) reconstruction parameters.

9.3.5/ NEMA ACCURACY OF CORRECTIONS

Across all our experiments (see Table 9.10), the maximum relative deviation from the expected true count rate was 2.54% for year the 2017 at 0.90 kBq.mL^{-1}. Similarly, Hsu et al. (2017) reported values of 2.43% (at 35.44 kBq.mL^{-1}) and 3.86% (at 1.19 kBq.mL^{-1}) forthe systems installed at Standford and Uppsala, respectively. A maximum relative error below the NECR peak of 3.41% was reported by Wagatsuma et al. (2017).

Table 9.10: Experimental data for the NEMA accuracy of corrections standard. The NECR peak activity is reported with the maximum absolute value and the mean of the errors below the NECR peak activity.

Measurement	GE console			
	2017	2020	2021	Avg ± SD
Activity at NECR peak (kBq.mL^{-1})	22.6	23.5	23.5	23.2 ± 0.4 (1.8%)
Maximum absolute (%)	2.54	2.44	2.36	2.40 ± 0.07 (3.0%)
Maximum absolute mean (%)	1.55	1.79	1.49	1.61 ± 0.12 (8.1%)

Figure 9.15 shows the true count rate and the fitted true count rate as a function of activity for the year 2021, calculated using the GE console and NEAT. Figure 9.16 shows the mean, minimum, and maximum relative differences (in %) between the true count rate

and the fitted true count rate as a function of activity, for the year 2021. The differences observed between the results of NEAT and those of the GE console were inferior to 1% for all years.

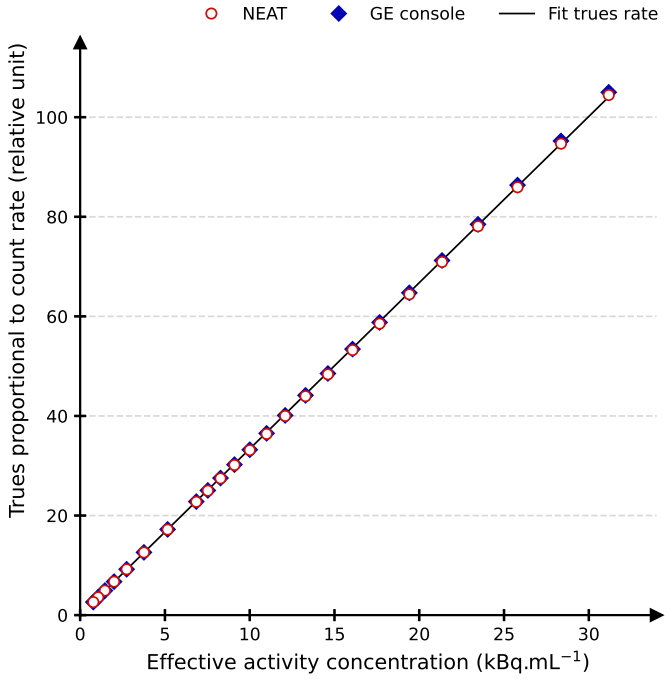

Figure 9.15: Validation of the NEMA accuracy of corrections test in NEAT (red) against the GE console (blue), using data acquired in 2021. The expected true count rate extrapolation (identical between NEAT and GE console) is given by the black line.

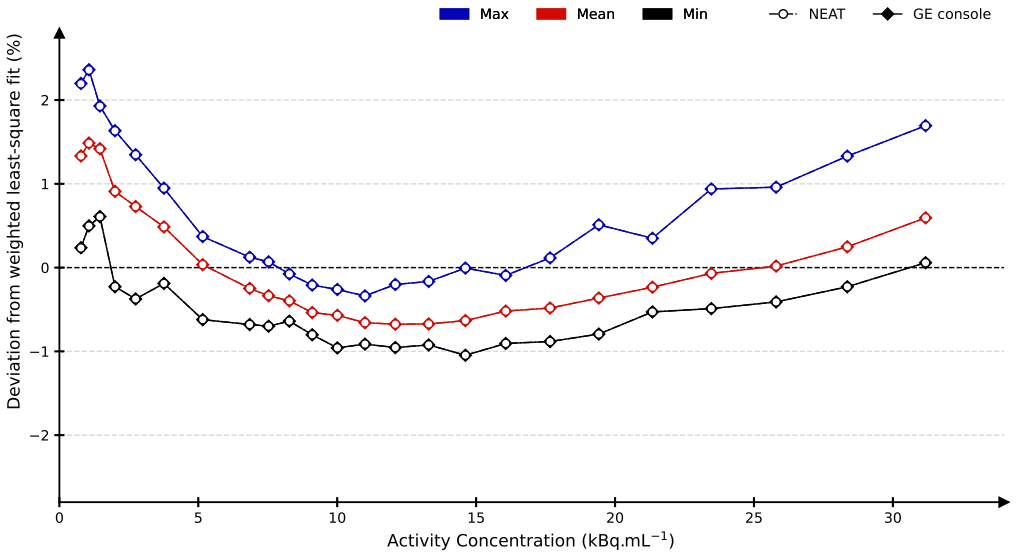

Figure 9.16: Comparison between the NEMA accuracy of the correction test, calculated with NEAT (dash-dotted) and the GE console (continuous). The minimum (black), maximum (blue), and mean (red) deviations from the expected true count rates (%) are shown as a function of the activity concentration (kBq.mL^{-1}).

9.3.6/ ENERGY AND TIMING RESOLUTIONS

Table 9.11 shows the energy and timing resolution for our experiments and the data reported in the literature. The resolutions observed in our experiment are very similar to those reported in the literature, with relative differences in energy and timing resolution of 0.26% and 0.49%, respectively. As this test is outside the scope of the NEMA standard, it has not been implemented in NEAT.

Table 9.11: Energy (%) and timing (ps) resolution for year 2020 and for Hsu et al. (2017); Chicheportiche et al. (2020)

Measurement	Literature				This work	Relative difference (%)
	HSU Stanford	HSU Uppsala	Chicheportiche	Avg ± SD (CV%)	2020	$M_{RD,\mu} \pm SEM_{RD,\mu}$
Energy resolution (%)	9.44 ± 0.07 (0.74%)	9.35 ± 0.05 (0.53%)	9.63 ± 0.08 (0.83%)	9.47 ± 0.07 (0.72%)	9.52 ± 0.09 (0.95%)	−0.49% ± 0.87%
Timing resolution (ps)	374.10 ± 2.60 (0.70%)	376.70 ± 2.70 (0.72%)	377.26 ± 2.62 (0.69%)	376.02 ± 2.64 (0.70%)	375.05 ± 3.79 (1.01%)	0.26% ± 0.26%

9.4/ DISCUSSION

All measurements were similar to the specifications in the manufacturer's datasheet (GE Healthcare, 2016b) and were also within their performance tolerances. In general, good agreement was found between our results and those in the literature, showing that differences are most likely due to variability between systems and operators.

In terms of sensitivity, the mean values of our experiments (12.95 ± 0.16 cps.kBq^{-1} at CFOV and 13.00 ± 0.16 cps.kBq at 10-cm radial offset) were in good agreement with the manufacturer's specification (13.50 cps.kBq^{-1} for the average of the two axial positions). Furthermore, our measurements at the CFOV differed from the literature by 2.97± 2.18% cps.kBq^{-1}, demonstrating the good stability of the measurement of this metric under different conditions. For the validation of NEAT, the calculated sensitivity was almost identical to that obtained with the GE console, with relative differences always below 0.01%. Small differences were found between the axial sensitivity profiles (4.86% for the year 2021), which can be explained by slight differences between the GE console and NEAT in the implementation of the random estimation. As mentioned in Section 9.1, the implementation of the RFS is not strictly identical in NEAT and the GE console . This does not affect the measurement of system sensitivity, as random events are corrected using the total random estimate value (not the sinogram) contained in the experimental HDF files. However, as the random sinogram was used in the sensitivity profile analysis, small differences were found for this metric.

For count losses (Table 9.5), the manufacturer's specifications for the Gen1 DMI4 scanner were 180 kcps (at 20 kBq.mL^{-1}) for the peak NECR and 41% for the scatter fraction (GE Healthcare, 2016b). For the peak NECR, our measurements were in good agreement with an average of 176 kcps at 23-24 kBq.mL^{-1}. However, we found an average relative difference of 6.38% ± 2.99% kcps with peak NECR values reported in the literature, indicating that the literature values were slightly higher than ours. Similar trends to the literature were observed for the peak true count rate (6.36% ± 3.21% kcps) and the associated activity concentration (7.32% ± 0.67% kBq.mL^{-1}). In contrast, our measured scatter fractions were slightly higher those reported in the literature (RD of -2.72 ± 0.93%). For the NEMA count losses and scatter fraction test, inter-observer variability can be particularly significant: filling the capillary is a critical step that must be mastered

to comply with NEMA conditions and to guarantee the activity actually present in the capillary. In addition, the positioning of the phantom (particularly with respect to the bed) can be more or less advantageous for certain metrics, such as the scatter fraction. For the validation of the NEMA count losses and scatter fraction test in NEAT, only slight differences were observed between NEAT and the GE console (up to 3.6% for the scatter count rate). As for the sensitivity test, these differences can be partly explained by the small differences in the implementation of the random estimation method.

For the NEMA spatial resolution (Table 9.7), slight variations in FWHM and FWTM values (maximum 4.15% ± 2.82%, see Table 9.7) were found between our experiments and the literature, showing a rather good reproducibility of the results over several experiments and systems. Although it is difficult to prepare point sources experimentally, this good reproducibility could be a consequence of using a source placement tool provided by the manufacturer. Nevertheless, the axial spatial resolution was often the most variable, probably due to the difficulty (in the GE procedure) of obtaining a Z-point source with capillaries. Regarding the validation of this test in NEAT, good agreement was generally achieved for all metrics, with relative differences in FWHM and FWTM values of up to 6.38% across all years (for 2021, see Table 9.6). The small differences observed between the GE console and NEAT can be explained by differences in the implementation of the point-source profile analysis (profile radius, 3-point parabolic fit, linear interpolation).

For the NEMA image quality test (Table 9.8), since our scanner is a 2017 model, the performance characteristics were first evaluated according to the NEMA NU 2-2012 report, where only four spheres were filled with radioactivity. Images were reconstructed using the default reconstruction parameters (VPFX-DEF) recommended by the manufacturer. In the literature, Wagadarikar et al. (2014) was the only study that strictly used the same reconstruction parameters, allowing a comparison with our results. Small differences in CRC and BV were observed across all sphere sizes, with maximum relative differences of up to 3.81% and 9.81% for CRC and BV, respectively. A notable difference between their results and ours is the reported lung error, with their value (7.4± 0.2%) being noticeably higher than ours (6.3± 0.3%). As the residual lung error is calculated in relation to the concentration in the background compartment of the phantom, these differences could be explained by experimental discrepancies in the accuracy of the background activity concentration (phantom filling, calibration of dose calibrator accuracy).

Regarding the validation of NEAT using the new acquisition of 2021 performed according to the NEMA NU 2-2018 standard, the reconstruction using VPFX-DEF parameters showed relative differences of 9.16%, 11.52%, and 8.69% for CRC, BV, and lung error, respectively. Smaller differences were observed with the VPFX-CLIN reconstruction for BV (4.80%) and lung error (1.14%), probably due to the fact that ROI positioning has less influence on the results when image noise is lower. In fact, the differences between the two packages are mainly due to differences in the definition and positioning of the ROIs for the NEMA analysis. In the GE console, the ROIs of a given experiment are placed automatically (and sometimes manually) for each of the three acquisitions. In contrast, in NEAT, all three acquisitions had exactly the same ROIs placement which was done manually. In addition, the ROI area was optimised against the matrix sampling grid in NEAT to favour area over shape. A similar approach might not have been used in the GE console.

In this chapter, IR has been introduced as another noise metric that is better suited to measuring pixel-to-pixel variations. Its benefits can be easily assessed by looking at the

differences between the VPFX-DEF and VPFX-CLIN reconstructions in Table 9.9. On the other hand, BV is more representative of the homogeneity between averages calculated in the regions defined in the NEMA analysis. In this sense, IR will be used to mainly compare simulations with experiment in the next chapter.

The accuracy of the corrections was evaluated in Section 9.3.5. The residual error of the corrections was similar to that reported in the literature for the whole activity range ($< 4\%$). The results of the test obtained with NEAT were very close to those of the GE console, with relative differences of less than 1%.

9.5/ CONCLUSION

In this chapter, the performance characteristics of our DMI4 scanner have been evaluated and tracked over several years. The reliability of our results has been checked by comparing them with NEMA analyses found in the literature for other DMI4 scanners. The performance characteristics of our system were stable over the years and close to the literature results. The experimental data were used to develop NEAT, our own NEMA analysis tool. NEAT includes data management methods (list-mode, prompt, random, and SSRB sinograms) to organise list-mode data and sinograms obtained with the DMI4 scanner into prompt, random, and SSRB sinograms. It also includes an implementation of the NEMA NU 2-2018 tests. By comparing the results obtained with the GE console and NEAT, our independent software has been validated for the following NEMA analyses: sensitivity, count losses and scatter fraction, spatial resolution, image quality, and accuracy of corrections.

10

Design, implementation and validation of a Monte Carlo model of the 4-ring GE DMI PET/CT scanner

The use of simulations in PET has long been recognised as a valuable tool for many applications (see section 2.3). There are several PET imaging simulators in the scientific community, which differ in their level of complexity and computational resource requirements (for a complete review, see Pfaehler et al. (2018); Salvadori et al. (2020)). Among them, GATE (Jan et al., 2004, 2011) is a well-known simulation toolkit, historically developed for nuclear imaging, with specific layers for modelling sources, detection geometries, and detector electronic responses. Initially used by PET scanner manufacturers to design PET systems, GATE is now widely used by the scientific community for research purposes. GATE has been successfully used to validate the performance of several existing PET systems or to study the impact of different detector designs (extensive review of validated GATE models by Sarrut et al. (2021)). The implementation and validation of a GATE model is usually done in several (sometimes simultaneous) steps. To model a PET scanner in GATE, the two main tasks are the reproduction of the geometry of the real system (Section 10.1) and the modelling of the electronic chain of this system, called digitizer in GATE (Section 10.4). In order to optimise the parameters of this digitizer, it is common to reproduce the experimental NEMA acquisitions, as they can provide insights into the performance of the GATE model (Section 10.3). These simulated NEMA acquisitions are also used to validate the performances of the final GATE model (Section 10.2). Once both the geometry and the electronic chain of the real PET system have been modelled in GATE, the model is validated by comparing its NEMA performance (Section 10.5.1 and Chapter 11) with that of the experimental system (Chapter 9). As the simulated data cannot be analysed directly using the manufacturers' tool (GE console), the previously validated NEAT software is used to analyse both simulated and experimental data.

10.1/ DMI GEOMETRY

GATE 9.0 and Geant4 10.5 were used to model the DMI. The DMI geometry was implemented according to the data presented in section 9.1. In GATE, the rsector[1] is the largest geometry within the cylindricalPET. Figure 10.1 illustrates the structure of a rsector. Each rsector contained four modules, which were adjacent in the axial direction. In each module, four blocks were stacked, following the curvature of the ring. Each block contained a 4 $\times$ 9 array of LYSO crystals of dimensions 5.3 (axial) $\times$ 3.95 (transaxial) $\times$ 25 (length) mm^3. Finally, a total of 34 rsectors were arranged to form a scanner ring. To obtain a complete 4-ring DMI scanner, this single scanner ring was duplicated four times along the axial axis.

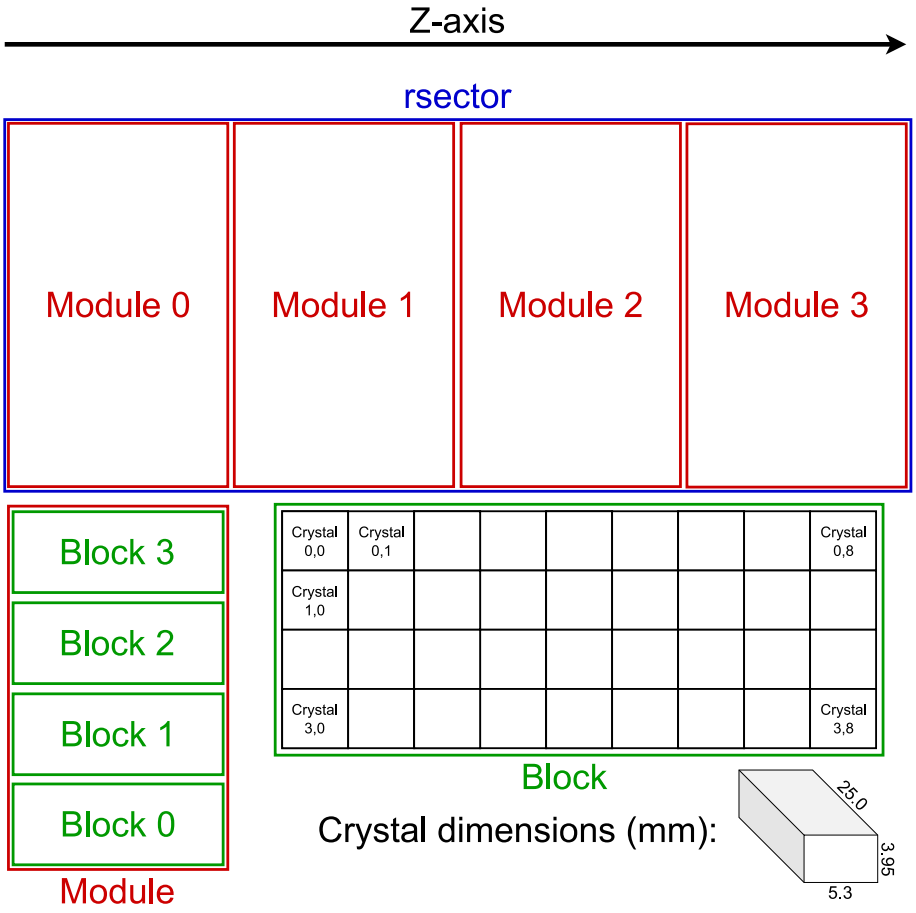

Figure 10.1: Illustration of the structure of a rsector (in blue), containing four modules (in red), each divided into four blocks (in green). The dimensions of the crystals (in black) are given. Extra spacing between structures has been added for display purposes.

The patient bed and inner plastic cover were modelled. In addition, the lead shielding of the rsectors was also modelled (as designed in the real DMI4 scanner), mitigating the effect of activity outside the FOV. Figure 10.2 shows the visual representation of the final DMI geometry in GATE, without the patient bed. In the referential of the model (centred on the FOV), the Z-axis points towards the back of the gantry, the Y-axis points towards the floor, and the X-axis would be on the left side of a patient lying on the bed.

[1] All GATE-related structures, commands and parameters are outlined in orange.

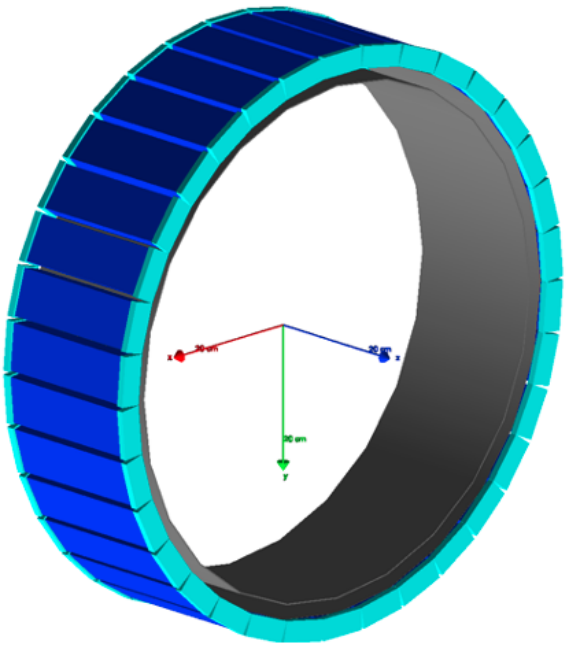

Figure 10.2: GATE representation of the DMI 4-ring with the rsectors in blue, the lead shield in cyan and the detector covers in grey.

10.2/ FRAMEWORK IMPLEMENTATION

10.2.1/ SIMULATION FRAMEWORK

During the development and optimisation phase, the GATE physics list was set to emstandard_opt3. For the NEMA test results in this chapter, the physics list has been set to emstandard_opt4, as it provides the best set of electromagnetic physics models. No custom cuts or variance reduction techniques were used in any of the simulations, i.e. all particles were generated and tracked according to the default behaviour defined in Geant4.

For the NEMA simulations, the radioactive source was set to $\beta+$ emission. The setForcedUnstableFlag was used to ensure source decay with setForcedHalfLife to 6586.2 s. As the source is set directly to positron emission (rather than an ion source), the ^{18}F branching ratio to $\beta+$ was reproduced by multiplying the desired ^{18}F source activity by 0.969 (see section 2.1). The energy of the $\beta+$ source was set according to the Landolt-Börnstein tables available in GATE.

For specific simulations (see Chapter 11), a backtoback source was used, where the two annihilation photons are emitted directly from the source. The two backtoback particles were set to gamma (particle gamma) and to the expected mono-energetic value (mono 511 keV). This source type has three main differences with a $\beta+$ source: 1) the positron generation and tracking is skipped, reducing the simulation time needed for a given acquisition time and source activity; 2) the effect of the positron range is removed (see section 4.1.1); and 3) the non-collinearity of the photons is removed by default (it can be re-modelled with setAccolinearityFlag True).

The simulations were run on the Centre de calcul de l'Université de Bourgogne (CCUB)

using computers with Intel Xeon Gold CPUs 6126 @ 2.60 GHz and 64 GB of memory. To speed up the GATE simulations, each simulation was equally divided into N sub-simulations of duration $t = T/N$, with $N \in \mathbb{N}^*$, $T \in \mathbb{R}^+$, where T is the simulation duration. The GATE parameter setStartTime, denoted $T_0 \in \mathbb{R}^+$, was used to set the start time of a sub-simulations n, denoted S_n, as follows:

$$S_n = nt + T_0, \ \forall n \in [\![0, N-1]\!] \tag{10.1}$$

Our simulations were run with $200 \leq N \leq 400$, depending on the expected simulation time. The random seed of each sub-simulation was determined automatically using the MersenneTwister generator.

For each sub-simulation, singles and coincidences were stored in Numpy format. At the end of the simulation, all sub-results were merged (concatenation of the Numpy arrays). Since each sub-simulation was run independently (no shared memory or calculus), the coincidence processing of the n^{th} and $(n+1)^{\text{th}}$ sub-simulations was independent. In other words, a single event registered at the very end of the n^{th} sub-simulations can never be paired with another single event registered at the very beginning of the $(n+1)^{\text{th}}$ sub-simulations, even if they would fall into the same CTW. Therefore, this simulation splitting method leads to count losses, especially when T is low and N is high. For a simulation where the source decay can be assumed to be null (T is small according to the source half-life), the total count loss percentage, denoted ΔC, is given by:

$$\Delta C = (N-1)\frac{0.5CTW}{T} \tag{10.2}$$

In our simulation, all combinations of T and N used satisfied $\Delta C < 1\text{e}{-6}$ %. However, for applications where the value of ΔC is considered to be high, it is possible to use the digiGATE tool to prevent count losses. In this case, each sub-simulation should only store Hits (detected events before electronic processing). All N Hits files are then merged and used as input to a single digiGATE instance to obtain coincidences. However, this method only speeds up particle generation and tracking, as the pulse processing and coincidence sorting are done by a single instance of digiGATE, rather than by N sub-simulations.

10.2.2/ ANALYSIS FRAMEWORK

This section detailes the management of GATE data. The single and coincidence events simulated by GATE were stored in a Python Numpy array (i.e. list-mode). In GATE, each event of this list-mode contains dozens of fields, each dedicated to a particular piece of information. For example, the eventID field is an identifier assigned to every particle generated during the simulation. Particles produced by the source have identifiers ranging from 0 to infinity, ordered by production time. Two annihilation photons produced by the same positron have matching eventIDs, and all events produced by the noise digitizer module have the identifier -2. Other examples are the binary fields comptonPhantom and comptonCrystal, which encodes the presence of Compton scattering in the phantom and crystal, respectively.

An important concept in the validation of a MC model is the use of ”clinical-like” simulated data. The aforementioned fields are not considered clinical-like because the event properties they contain cannot be obtained in a clinical setting. Using these fields, it would

be possible to perfectly separate true, random and scatter coincidences from a list of N events, as described in Algorithm 1[2]. They could be used to obtain the NECR described by Equation 9.10 (without following the NEMA Methodology for the Count losses and scatter fraction performance evaluation), and to extract true events for the Image quality evaluation, eliminating the need for accurate random and scatter corrections.

Algorithm 1: Simple method for separating coincidence events according to their type (random, scatter or true)

```
n.eventType ← "Prompt";
while n ≤ N do
    if (n.eventID1 not n.eventID2) or n.eventID1 == -2 or n.eventID2 == -2 then
        n.eventType ← "Random";
    else
        if n.comptonPhantom1 or n.comptonPhantom2 or n.comptonCrystal1 or
          n.comptonCrystal2 then
            n.eventType ← "Scatter";
        else
            n.eventType ← "True";
        end
    end
end
```

In this work, only clinical-like fields were used to perform NEMA-analyses. In the previous chapter, NEAT was validated, and the *SinoGenerator* interface was presented, allowing experimental data to be processed by various methods to obtain 3D, 3D+TOF, RFS, and SSRB sinograms. By properly interfacing these validated methods with GATE-simulated data, NEAT could perform the performance evaluation on both experimental and simulated data, using only clinical-like GATE fields as well as the previously validated NEMA analyses. Two additional Python interfaces were developed for this purpose.

First, the *projectConstants* contains stable information about the experimental system. Below is an example of initial information "hard coded" to later determine additional structural information (number of crystals per block, number of modules per scanner, number of crystals per module, etc.):

- Number of rsector per scanner: 34
- Number of module per rsector: 4
- Number of block per module: 4
- Number of horizontal crystal per block: 9
- Number of vertical crystal per block: 4

Similarly, data on the experimental 3D+TOF sinogram (size, resolution, and shape) were stored and used to calculate similar information for other sinograms (SSRB, RFS, 3D).

[2] Additional fields could be used to define stricter conditions (such as Rayleigh scattering) according to the intended application.

With this design, the DMI 4-ring were to be upgraded to a DMI 5-ring, only few initial variables would need to be changed to keep the entire interface working.

The *lutGenerator* interface then manages the transition from GATE detector identifiers to clinical-like detector indexes. To enable the use of the *SinoGenerator* on simulated data, the indexes generated by the *lutGenerator* must be strictly equivalent to the indexes used by the real system. Information on the detector indexing of the DMI4 was obtained during a privileged information with the manufacturer (NDA). Experimentally, each detected photon is assigned an axial crystal index and a transaxial crystal index (according to the crystal of interaction). In GATE, the detector recording the first[3] part of a coincidence can be identified using the following GATE fields: rsectorID1, moduleID1, submoduleID1, crystalID1[4]. The value of these fields depends on the initial placement of the structures and their direction of duplication, which have been carefully chosen to provide a convenient indexing of the aforementioned GATE fields.

From this point, methods have been developed to allow the transition between different indexing representations (unique detector number, detector spatial coordinates, etc.). For example, the axial crystal index of a given event can be obtained using these fields in combination with the information contained in the *projectConstants*:

$$\text{axialID} = \text{moduleID} \times (\text{horizontal crystal per block}) + \text{crystalID}//(\text{vertical crystal per block}), \tag{10.3}$$

where // is the Euclidean division operator. The combination of the *SinoGenerator*, the *projectConstants*, and the *lutGenerator* interfaces provides a complete pipeline for generating clinical-like sinograms from GATE-simulated data.

10.2.3/ RECONSTRUCTION FRAMEWORK

10.2.3.1/ INTRODUCTION

A reconstruction interface, hereafter referred to as the ”simulation package”, was developed in MATLAB to allow the reconstruction of GATE-simulated data using the manufacturer’s reconstruction software (PET toolbox). The first version of this interface was provided by the manufacturer, but it was designed for a different MC simulator (SimSET), and all the reconstruction parameters and corrections were not interfaced. In this thesis, we have redesigned this skeleton to allow reconstruction and correction of GATE data.

As described in Chapter 7, several correction methods should be applied to the data to be reconstructed. Some do not require any additional information, such as the model-based scatter correction implemented in the PET toolbox. However, other methods may require additional files: calibration files for normalisation correction, a RFS sinogram for random correction, and an attenuation map for attenuation correction. As the reconstruction is to be performed by the PET toolbox, these files must be properly interfaced in the simulation package. The generation of these files is described in the following sections. In addition, methods have been developed to manage the reconstruction of 3D+TOF sinograms using the TOF-OSEM algorithm of the PET toolbox.

[3] In Gate, the two events forming a coincidence are ordered according to their detection time.
[4] rsectorID2, moduleID2, submoduleID2, and crystalID2 for the second part of the coincidence.

10.2.3.2/ Random, scatter and attenuation corrections

A straightforward implementation was the random correction, which requires a random sinogram of clinical shape. In this case, a RFS sinogram (see Section 7.4) is generated from the simulated single events using the *SinoGenerator* interface. The scatter correction was performed by the model-based method implemented in the PET toolbox, based on the prompt sinogram to reconstruct.

An attenuation map is then required to perform the attenuation correction. As the CT component of the DMI4 was not modelled in GATE, this map was generated using the GATE MuMap actor. The output of this actor is a CT-like image, centred on the PET CFOV (user defined). Its size and resolution were $256 \times 256 \times 71$ pixels and $2 \times 2 \times 3$ mm^3, respectively. It contained the spatial distribution of the linear attenuation coefficients at 511 keV of the imaged area.

10.2.3.3/ Additional simulations for normalisation correction

To determine the geometric factors and individual detector efficiencies (see Section 7.2), two simulations were run at very high statistics. This work was part of the master thesis of Sayah (2021).

In the first simulation, a cylindrical water phantom with a radius of 10 cm radius and a height of 22 cm was positioned at the centre of the FOV (see Figure 10.3a). The phantom was filled with a positron source of 50 MBq activity. Data were acquired during a 1200 second simulation, and a total of 562 million true counts were collected. This simulation took 137 CPU days to complete.

The second simulation used a ring source with an outer radius of 32 cm, a thickness of 1 mm, and a length of 20 cm, centred on the FOV of the scanner, with the plastic cover of the gantry removed (see Figure 10.3b). As no scattering medium was included (no geometrical phantom), the source was set to back-to-back emission (annihilation photons), with an activity of 38.7 MBq (corresponding to 40 MBq of ^{18}F). For this calibration file, a total of 3.2 billion true events were collected for a simulated duration of 1080 seconds, which took more than 250 CPU days.

For both simulations, true coincidences were extracted (see Algorithm 1) and later stored in 3D sinograms. These sinograms were used as calibration files to perform the normalisation correction in the simulation package.

10.2.3.4/ Validation of the normalisation correction

In order to assess the correct simulation and implementation of the normalisation correction, an experimental acquisition was performed using a flood phantom of 10 cm radius and 22 cm height, positioned at the centre of the FOV. The experimental data were then reconstructed using the PET toolbox with a parameter set similar to the VPFX-CLIN reconstruction defined in Table 9.2, but without the use of TOF information. All available corrections have been applied.

This acquisition has been reproduced in GATE (see Figure 10.4) using a 40 MBq positron source. The simulated data were reconstructed in the simulation package, using recon-

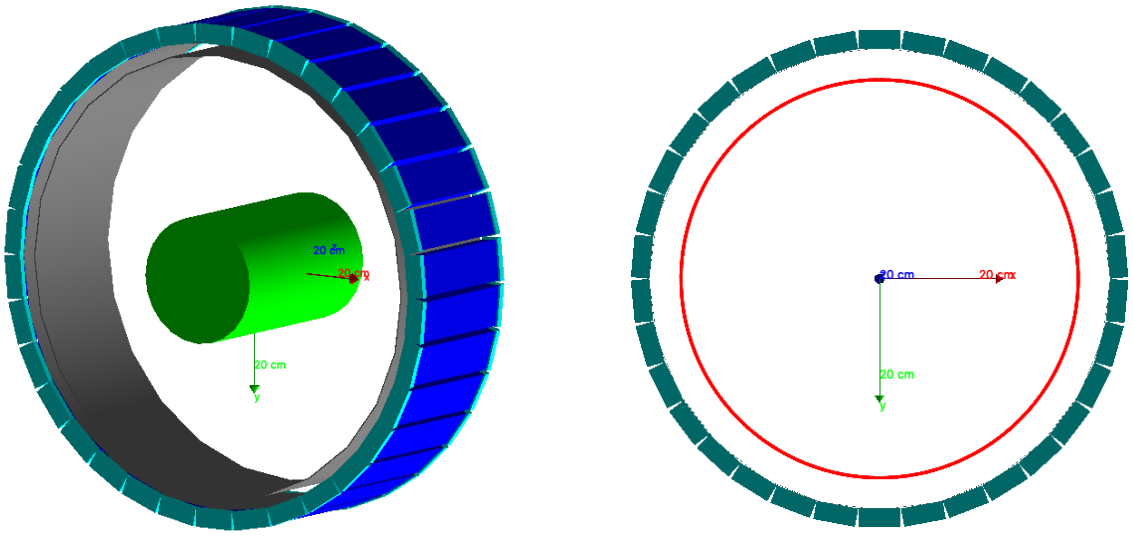

(a) (b)

Figure 10.3: (a) GATE representation of the cylindrical phantom (in green), placed at the CFOV. **(b)** The 32 cm radius ring source (in red) inside the DMI4 scanner model, without the gantry cover. The source thickness has been increased for display purposes.

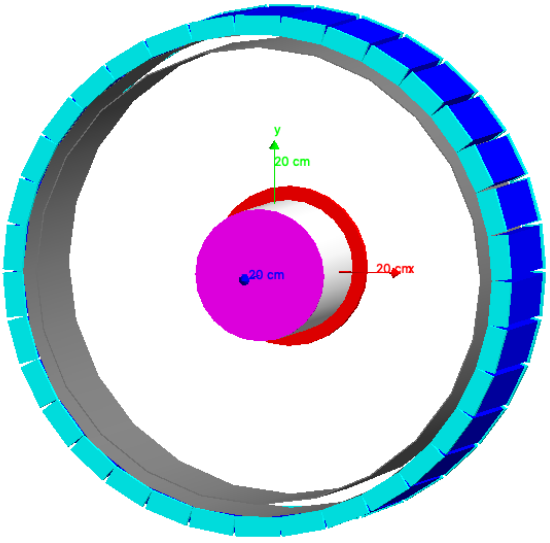

Figure 10.4: GATE view of the flood phantom. The central cylinder (in white) was filled with activity, placed at the CFOV, and closed by a front lid (in magenta). Experimentally, the back lid (in red) would be used by a support gantry to hold the phantom without the need for the patient bed.

struction parameters identical to those of the experimental reconstruction. In the simulation package, random, scatter and attenuation corrections were applied as described in Sections 10.2.3.1 and 10.2.3.2. In addition, the calibration files generated in Section 10.2.3.3 were used to perform the normalisation correction, according to a component-based method as described in Section 7.2 Badawi et al. (1999); Pépin et al. (2011).

To compare the experimental and simulated reconstructed images, horizontal and vertical profiles (of size 22.7 cm and centred on the source) were extracted from the central

reconstructed axial slices. As all corrections were applied for the reconstruction of the experimental image, the result was a calibrated image, where each pixel contains a value in Bq.mL^{-1}. For the simulated image, as no quantitative corrections were not applied, the data are expressed in counts per pixel. However, for comparison purposes, the profiles extracted from both images were normalised to their respective maximum pixel values. Figure 10.5a and 10.5b show the normalised horizontal and vertical profiles, respectively.

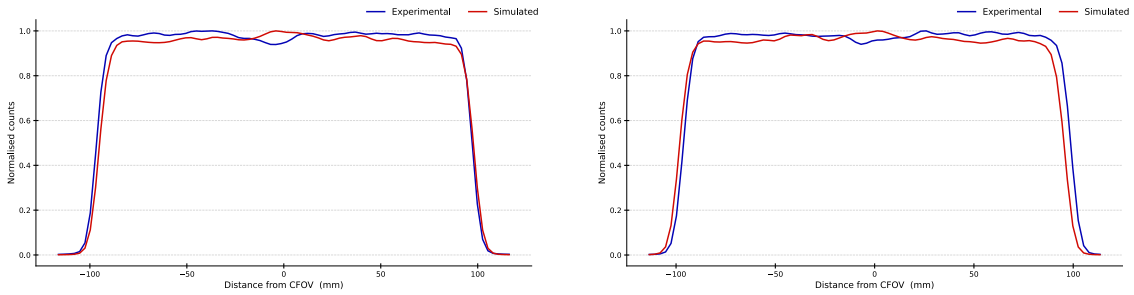

(a) **(b)**

Figure 10.5: (a) Horizontal and **(b)** Vertical profiles for experimental (in blue) and simulated (in red) reconstructed data. The profiles were extracted from the central axial slice of each reconstructed image.

Considering the central 160 mm portion of these profiles (thus excluding the border of the phantoms), the maximum relative difference between the experimental and simulated images was 6.5% and 5.2% for the horizontal and vertical profiles, respectively. Larger differences are observed on both sides of the profile, representing data at the boundary of the flood phantom. This is due to small differences in the placement of the phantom for the experimental and simulated acquisitions. Indeed, while the simulated phantom was placed exactly at the CFOV, the placement of the phantom during the experimental acquisition may not have been perfectly at the CFOV. In addition, the CV (see Section 9.2.7) was calculated on the central axial slice of both reconstructed images, using a large disc ROI (70 mm radius) centred on the flood phantom. The CV was 1.5% for both images.

10.2.3.5/ NORMALISATION ARTEFACTS REMOVAL

Although the normalisation correction has been validated, artefacts were observed at the border of the FOV when reconstructing simulated data. An example is shown in Figure 10.6, where a NEMA image quality acquisition was simulated (IEC phantom) and reconstructed in the simulation package using the VPFX-CLIN parameters.

Additional experiments showed that the position of the ring source induced the artefacts, which were specifically located in the area between the source (32 cm radius) and the extremity of the FOV (35 cm radius). These artefacts also affected the reconstructed image around the CFOV, in particular leading to BVs higher than that of the experimental data on the NEMA phantom/model.

To avoid these ring artefacts, other ring source radii were tested (e.g. 35 cm, the FOV extremity). However, the resulting calibration files did not provide satisfactory image quality on reconstructed images according to the metrics of the NEMA IQ test. Instead, to remove the artefacts induced by the 32 cm ring source, modifications were made to the

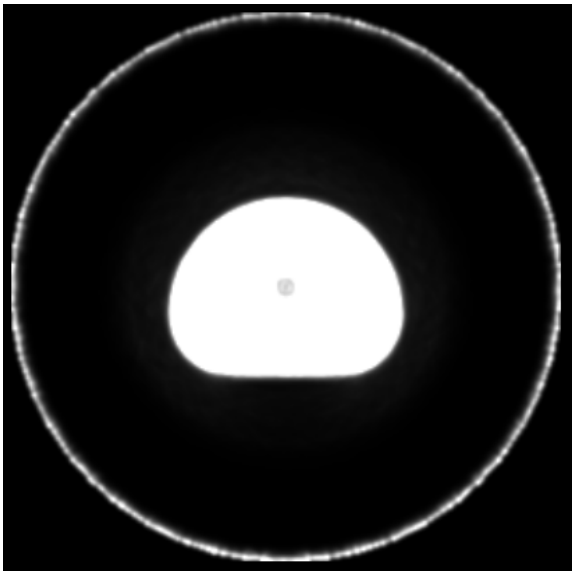

Figure 10.6: The ring artefact observed in the IEC phantom reconstruction. The window and level were chosen to show the ring, and intensity values of the ring artefact were four times lower than the IEC phantom background.

input data of the simulation package. The prompt and random sinograms of the data to be reconstructed, as well as the two normalisation calibration sinograms (ring and cylindrical sources), were modified to remove all data at a radial distance from the CFOV greater than 32 cm.

This means that the maximum achievable reconstructed FOV is 64 cm with the simulation package, compared to 70 cm when using the PET toolbox with experimental data. A comparison between experimental (PET toolbox) and simulation (simulation package) image quality results is presented in Section 10.5.4. This reduction in the reconstructed FOV does not affect other performances of the model (evaluated according to the NEMA standard). Furthermore, most PET-imaging applications rely on imaging an object centred in the CFOV.

10.3/ NEMA TESTS IMPLEMENTATION IN GATE

10.3.1/ NEMA SENSIBILITY

The dimensions of the aluminium sleeves strictly followed the NEMA guidelines (see Figure 9.2). The sleeve material was set to aluminium and the source container was modelled by a plastic hole cylinder. The hole radius was 0.5 mm and the container thickness was 0.5 mm. Figure 10.7 shows the source centred in the FOV with five aluminium sleeves.

For this simulation, the information contained in the experimental HDF data files was extracted to closely mimic the experimental conditions. The experimental source calibration time and activity were used to define T_0 and the initial activity in GATE. Then, for each simulated acquisition (one per sleeve per position), the start and stop times of the experimental acquisitions were used to exactly reproduce the source decay between

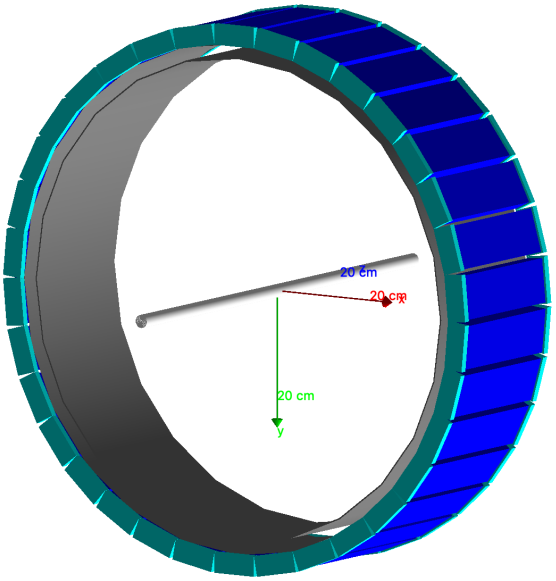

Figure 10.7: Model of the NEMA sensitivity source in GATE. Five aluminium sleeves (in white) are centred in the FOV.

acquisitions.

The 3D sinograms were processed using NEAT: they were first rebinned into 2D sinograms using SSRB and then analysed according to NEMA specifications. The system sensitivity (counts.sec^{-1}.MBq^{-1}) and the axial sensitivity profile were reported for both source positions.

10.3.2/ NEMA COUNT LOSSES AND SCATTER FRACTION

The phantom was geometrically defined and placed as described in Section 9.2.2.2, with the source insert and the container reproduced. In GATE, the material was set to polyethylene, and the source container to plastic. The GATE model of the patient bed was included in this simulation, as shown in Figure 10.8.

The experimental acquisition consists of 24 frames acquired over ten hours, where the initial activity is very high (see Section 9.2.2.2). This very long and high activity acquisition could not be fully simulated in GATE, as the CPU time and computing power required would have been excessive. Therefore, the duration of each simulated frame was set to obtain at least ten million prompts per frame, while maintaining the same number of frames and average activities as the experimental acquisition.

10.3.3/ NEMA SPATIAL RESOLUTION

Radioactive water spheres of 0.5 mm radius were used to simulate the six point sources. The duration of the simulated acquisition was 60 seconds, and the activity was set to 5 MBq for each source. Image reconstruction was performed with the simulation package, using the PET toolbox implementation of the FBP algorithm. In accordance with NEMA, a ramp filter and a cut-off at the Nyquist frequency (no smoothing) were used. The recon-

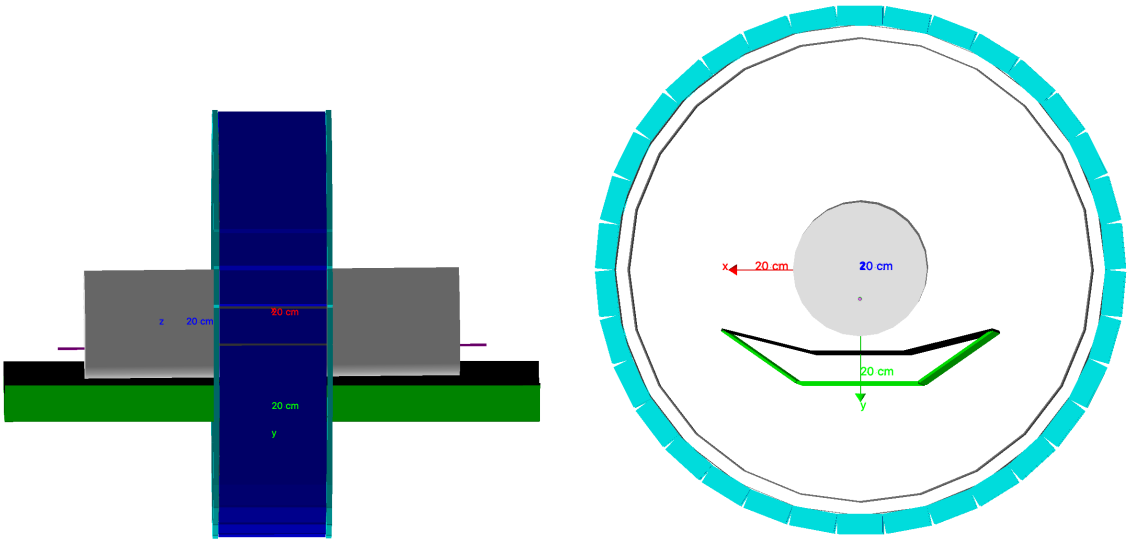

(a) (b)

Figure 10.8: Illustration of the cylindrical model (in grey) used for the NEMA count losses and scatter fraction test. The source insert is shown in magenta, and the patient bed in black and green. **(a)** shows a side view of this model in the DMI4 scanner, and **(b)** a front view of the same model.

struction was centred on the sources with a transverse FOV of 250 mm to obtain a voxel size of $0.65 \times 0.65 \times 2.79$ mm^3. These reconstruction parameters resulted in a reconstruction of the simulated data that was identical to the experimental data.

10.3.4/ NEMA IMAGE QUALITY

In GATE, an IEC NEMA body model was geometrically defined according to the NEMA specifications (see Section 9.2.4.2). The patient bed and the 700 mm long cylindrical phantoms used in Section 10.3.2 were included in this simulation (see Figure 10.9a). The initial activity used in the simulation was strictly replicating the experimental activity. All containers used a plastic material, and they were filled with water. The simulated data were collected over a single simulation of 271 seconds, reproducing the data acquisition setup of the first experimental acquisition of the year 2021.

Due to the geometric complexity of this phantom, the spheres and background source were overlapped in GATE (see Figure 10.9b). At the sphere location, this leads to cumulative emission of both the background and source activity. This problem has been solved by using the Forbid command for background regions to prevent the emission of background activity in the sources.

Since the background consisted of several compartments (see Figure 10.9b), and since the background activity must be constant, an activity value was set for each compartment. This activity was chosen according to the expected uniform background activity concentration (5.3 kBq.mL^{-1}) and the volume of each compartment. Each volume was analytically determined according to the shape and size of the compartment. If source spheres were present in a compartment, their volume was subtracted from the volume of that compartment.

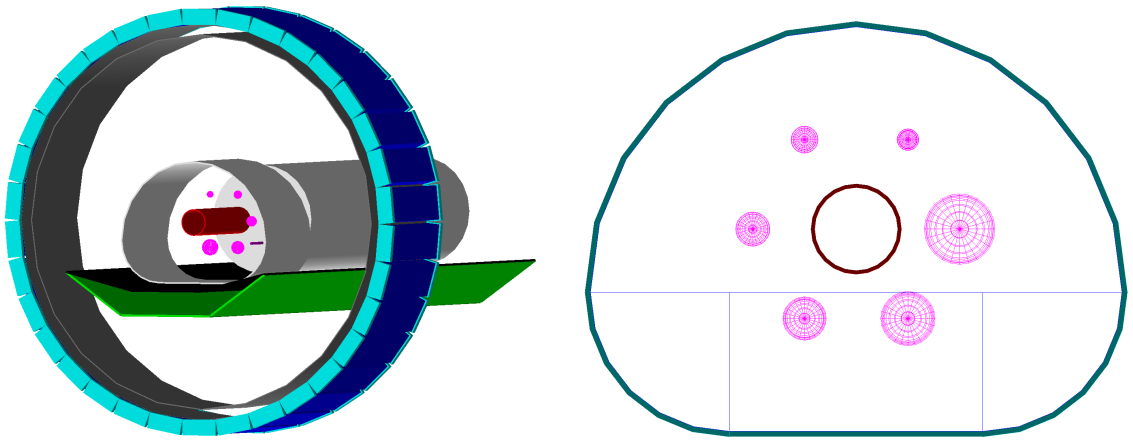

(a) (b)

Figure 10.9: (a) The complete NEMA IQ model viewed from the rear of the gantry, including the patient bed and the NECR phantom shown in Figure 10.8. In the IEC phantom, the lung insert is shown in red, and the source containers (spheres) are shown in magenta. **(b)** Front view of the IEC phantom, where the plastic outer shell of the phantom is shown in cyan, the source compartments in red, and the lung insert in red. The blue lines represent the boundaries of the four compartments of the phantom: upper (half cylinder), lower left and right (quarter cylinders), and the lower central part (rectangle).

The data were reconstructed using the simulation package algorithm with the VPFX-CLIN parameters (see Table 9.2). In order to assess the impact of the corrections on the simulated data, an additional reconstruction was performed and analysed in which the prompts were perfectly corrected for random and scatter counts (i.e. only true counts were reconstructed).

10.4/ ELECTRONICS MODELLING AND SIGNAL PROCESSING

In GATE, the digitizer handles the signal processing of events. For PET systems, it is used to process Hits (interactions) in crystals into Coincidences. It consists of several modules that can be tuned by their associated parameters to model the electronic chain of a PET system. The modules are connected in series, with the output of one module being passed on to the next. The order in which the modules are implemented is therefore important. Hits in crystals (also called sensitive detectors) are added and integrated into Pulses. These Pulses are then processed by other digitizer modules to form Single events. Finally, Coincidences are obtained by pairing Singles using the coincidence sorter. In general, a digitizer chain is organised in the following order: 1) adder, 2) readout, 3) background noise, 4) detection efficiency, 5) energy resolution, 6) temporal resolution, 7) pile-up, 8) dead time, 9) energy windowing, and 10) coincidence sorting. The following sections describe the digitizer modules and the methods used to determine their optimal parameter values. Figure 10.10 shows the signal processing chain (module parameters and values) formed by the different modules of the GATE model of the DMI4.

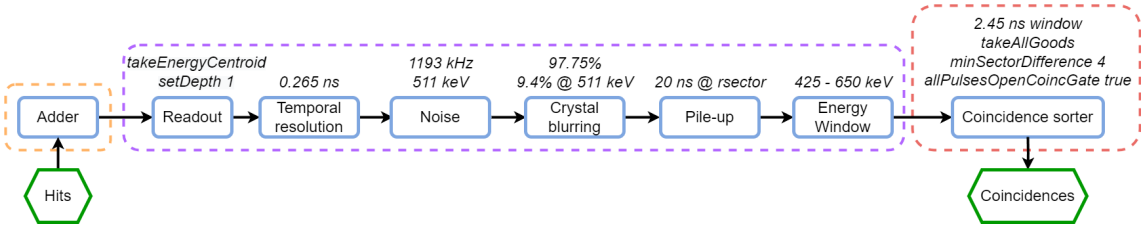

Figure 10.10: The complete digitizer model of the DMI4 scanner. In blue are the different modules with their associated parameter values. The orange dashed box encapsulates the processing of hits, the purple box the processing of pulses, and the last red box the processing of singles into coincidences.

10.4.1/ ADDER AND READOUT

The Adder is the first module of the digitizer and is used to model the fact that PET electronics do not have the time or energy resolution necessary to distinguish between the individual interactions of a particle within a crystal. The Adder groups the Hits occurring in a crystal and sums the deposited energy to compute the energy-weighted centroid position.

Tthe Readout module is then used to model the coupling between scintillation crystals and photodetectors (see section 3.3) by defining an artificial geometry, usually associated with a group of sensitive detectors. In effect, the Readout module regroups Hits per group of sensitive detectors and computes the output position of the combined Hits at the geometric level of the sensitive detectors. The output of this module is called a Pulse and has an energy equal to the sum of the grouped Hits.

To place the pulse in the sensitive detectors, the Readout module can use two different policies: TakeEnergyWinner, considered as a (1:1) coupling with photodetectors, and TakeEnergyCentroid, considered as a multiplexing between a small number of crystals and a larger number of photodetectors.

With the TakeEnergyCentroid policy, the final interaction position is obtained by calculating the energy-weighted centroid position of the hits. With the TakeEnergyWinner policy, the interaction position is set according to the position of the crystal with the maximum energy deposited.

In their work, Khalif et al. (2016) outlined the strong influence of the readout depth of the TakeEnergyWinner policy on the sensitivity of the modelled system. They showed that a readout at the highest structural level, i.e. at the rsector, provided the highest sensitivity. This result is to be expected, since the lower the readout, the more likely it is that an event undergoing inter-crystal scattering will be rejected. Furthermore, the recovery of scattered events with methods such as the CSR (see section 9.1) is not available in GATE. The use of a high structural readout level can help to emulate the sensitivity increase provided by such methods. The use of the TakeEnergyWinner policy combined with a readout at the rsector level is widely accepted by the GATE community as the best setup for modelling PET systems (Sarrut et al., 2021).

In our DMI model, the TakeEnergyCentroid was used, as it is better suited than TakeEnergyWinner to reproduce the experimental Anger logic[5]. Contrary to what is reported in the

[5] In the actual DMI4 scanner, signal readout is performed at the block level, providing a readout area of 16

GATE documentation, (TakeEnergyCentroid implies setDepth 3), our tests with a simple digitizer have shown that different values of setDepth result in different count rates (see Figure 10.11).

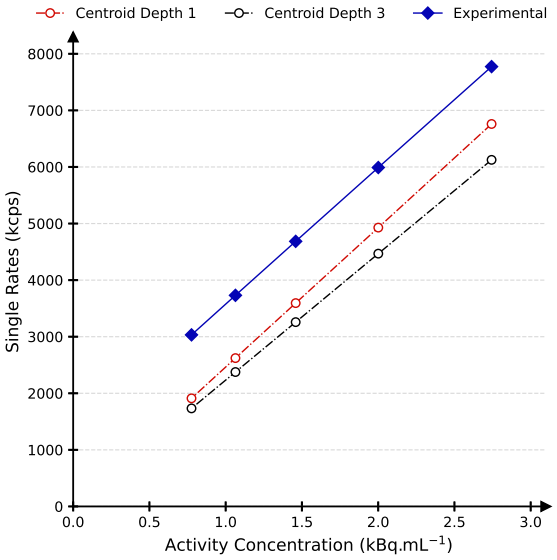

Figure 10.11: Low activity frames of the NEMA count losses test for an experimental acquisition (in blue), and simulations TakeEnergyCentroid with a setDepth value of 1 (in black) and a value of 3 (in red).

This behaviour is similar to that reported by Khalif et al. (2016) but for TakeEnergyWinner. Experiments on both policies have shown similar count rates between TakeEnergyWinner with setDepth 1 and TakeEnergyCentroid with setDepth 1, allowing our DMI4 model to match experimental single rates at low activities (see Section 10.4.3).

10.4.2/ Energy window and resolution, temporal resolution

The energy resolution was set to 9.4%, the value obtained experimentally using the method described in Section 9.2.6. In GATE, the temporal resolution of singles events has to be defined in terms of STR (see Section 3.5). According to Equation 3.5 and a CTR value of 376 ps, the value used in the digitizer was $\mathrm{STR} = 0.265$ ns. Energy thresholding is the final step in the signal processing of Pulses. According to the manufacturer's specifications, the lower and upper thresholds of the energy window were set at 425 and 650 keV, respectively.

10.4.3/ Background noise and detection efficiency

The background noise represents the count rate detected by the system when there is no activity in the FOV. This noise can come from the detection electronics, the natural radioactivity of the scintillation crystals (^{176}Lu for LYSO and LSO crystals), or dark counts inherent to SiPM-based detection systems (Gundacker et al., 2020).

$\times$ 48 mm^2 (Hsu et al., 2017).

The detection efficiency module is a multiplicative factor, denoted ϵ, used to account for detection losses unaddressed by other digitizer modules, and to compensate for inaccuracies in geometry and material composition.

Experimentally, a background-noise acquisition of the NEMA count losses cylindrical phantom was performed for 20 hours, without any activity placed inside or outside the FOV, and the single rate (here background noise single rate) was 1149 kcps. However, this value cannot be used directly in our model as it represents the experimental background-noise rate at the end of the detection chain, after the unknown detection efficiency value and after energy discrimination. To obtain λ_{sim} and ϵ_{sim}, the values of background noise and detection efficiency to be used in GATE, the methodology proposed by (Salvadori, 2020) was followed.

The experimental single count rate, denoted S_{exp}, acquired during the NEMA count losses test was used. As the source decayed, the activity of the last five frames was below 5 kBq.mL^{-1}. It is therefore safe to assume that the five lowest-activity experimental frames are free of dead time effects. These five experimental frames were compared with simulated single count rates, denoted S_{sim}, acquired under the same conditions, with simulation dead time, pile-up, background noise (λ_{sim}), and detection efficiency (ϵ_{sim}) ignored, i.e. removed from the digitizer. Using the previous assumption, it can be deduced that the experimental and simulated data differ only due to the effects of background noise and detection efficiency. Therefore, a linear fit was used (see Equation 10.4) to determine ϵ_{sim} and λ_{sim}.

$$S_{exp} = \epsilon_{sim}(S_{sim} + \lambda_{sim}) \tag{10.4}$$

Using this method, a background noise rate of 1193 kHz and a detection efficiency of 97.75% were found (see Figure 10.12). The experimental noise (1149 kcps) was compared with $\lambda_{sim} \times \epsilon_{sim}$ (1166 kcps) by means of relative difference (1.5%) to verify the noise value obtained.

Since λ_{sim} represents the background noise contribution at the end of the electronic chain (i.e. energy-qualified), the energy distribution of the background events was modelled by a Gaussian distribution centred at 511 keV with no standard deviation (see Figure 10.10). This setup ensured that all the generated background noise would fall within the limits of the energy discrimination module.

10.4.4/ Coincidence sorting

After energy thresholding, singles are grouped into coincidences using the coincidence sorter (Strydhorst et al., 2016). In GATE, two methods are available to define the opening of a CTW, depending on the value (binary) of the parameter allPulseOpenCoincGate. In *single-window* mode (allPulseOpenCoincGate False), only a single CTW can be opened at any given time. Therefore, the maximum coincidence rate achievable with this method is limited and proportional to the width of the CTW. In contrast, allPulseOpenCoincGate True defines the *multiple-window* mode, where each single opens its own CTW, regardless of whether a CTW is already open or not. Intuitively, the use of *multiple-window* will lead to prompt rates at least equal to those of *single-window*. At high activity, where the single event rate is high, the *multiple-window* mode will provide a much higher prompt rate than the *single-window* mode. In our model the *multiple-window* mode was used.

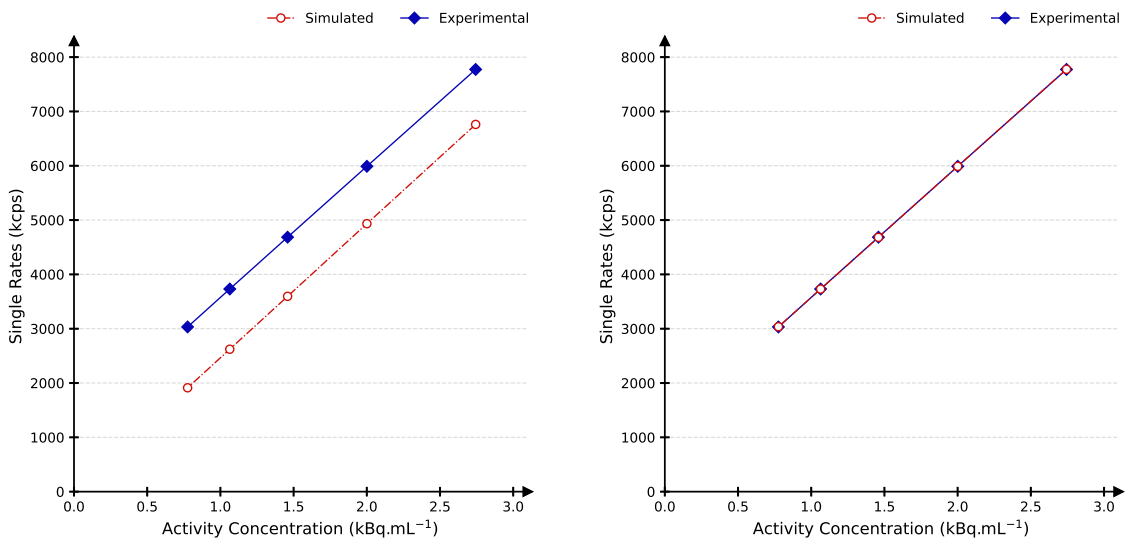

Figure 10.12: (a) Single rates obtained using the NEMA count losses methodology for experimental data (in blue) and simulated data (in red). **(b)** Fit of the simulated data to the experimental data using ϵ_{sim} and λ_{sim} as parameters.

According to the DMI CTW value of $2\tau = 4.9$ ns, the value of τ (2.45 ns) was used in the digitizer.

In a real PET system, the transaxial FOV size is smaller than the distance between two opposite crystals in a given detector ring. For the DMI, the transaxial FOV is 70 cm, while the face-to-face distance of strictly opposed detectors is about 74 cm. Using an experimental list mode, it can be observed that the minimum transaxial index difference of the detectors is 65. According to Figure 10.1, a rsector contains $4 \times 4 = 16$ transaxial crystals. Therefore, a rsector index difference of at least 65 // 16 = 4 (Euclidean division) is required for events to be in-coincidence. In GATE, the parameterminSectorDifference is used to define this geometric condition. As this parameter is based on the calculation of the rsector index difference for the two in-coincidence events, the found value of 4 was used in the digitizer. Only coincidence events that met this geometric condition were processed further.

Then a multiple coincidence policy is used to handle the system behaviour when more than two singles are found in coincidence in a given CTW. The selection of the *good* coincidence(s) can be defined according to one of the nine policies available in GATE (see Table 10.1), where:

- at least one coincidence registered in the output (takeAllGoods, takeWinnerOfGoods, takeWinnerIfIsGood, takeWinnerIfAllAreGoods)
- the result is **not recorded**, but will participate to the electronics dead time and bandwidth occupancy (keepIfOnlyOneGood, keepIfAnyIsGood, keepIfAllAreGoods)
- the result is or may be totally discarded, triggering no dead time and not being recorded (killAllIfMultipleGood, killAll)

From Table 10.1, we can see that the takeAllGoods policy will provide a higher prompt

Table 10.1: Description of the nine different multiple coincidence policies. The minimum and the number of registered events are given for n singles in the considered CTW.

Parameter	Definition	Min registered	Max registered
takeAllGoods	Each good pairs are considered	1	C_n^2
takeWinnerOfGoods	Only the good pair with the highest energy is considered	1	1
takeWinnerIfIsGood	If the pair with the highest energy is good, take it, otherwise, kill the event	0	1
takeWinnerIfAllAreGoods	If all pairs are goods, take the one with the highest energy	0	1
keepIfOnlyOneGood	If exactly one pair is good, keep the multicoincidence	0	0
keepIfAnyIsGood	If at least one pair is good, keep the multicoincidence	0	0
keepIfAllAreGoods	If all pairs are goods, keep the multicoincidence	0	0
killAllIfMultipleGoods	If more than one pairs is good, all events are killed	0	0
killAll	No multiple coincidences are accepted	0	0

rate than any other policy. The takeAllGoods policy was used with the aim of achieving the real sensitivity of the system (especially without a CSR method in GATE). Finally, it is possible in the coincidence sorter to apply an electronic dead time to the processed coincidences. No coincidence dead time was used in this work.

10.4.5/ SINGLES DEAD TIME AND PILE-UP

10.4.5.1/ INTRODUCTION

Up to this point, the proposed digitizer (associated with the geometry defined in Section 10.1) can be used to reproduce experimental single rates at low activity (see Section 10.4.3). At high activity, count rates are affected by two main non-linear effects: dead time and pile-up (see Sections 4.3.1 and 4.3.2).

The photon detection loss induced by pile-up is related to energy thresholding. On the one hand, the stacking of two single events can shift the signal of a photon within a true coincidence outside the energy window (decreasing the rate of true coincidences). On the other hand, it can also move the signal of a scattered photon inside the energy window (increasing the rate of scattered coincidences). Therefore, the pile-up value affects the true-to-scatter ratio, and must be modelled before energy discrimination.

The dead time can be modelled either before or after the energy window, with no subsequent effect on the true-to-scatter ratio. If modelled after the energy window, an experimentally determined value can be used. If modelled before the energy window, an optimisation process is required. While increasing the pile-up values will reduces the the true-to-scatter ratio and the prompt rate, increasing the dead time will only reduce the prompt rate.

Finding suitable values for these two digitizer parameters is complex and, as a result, it is common for GATE models to be designed to reproduce experimental count rates only at low activity. In this case, the NEMA standard for count losses and scatter fraction is ignored during the validation of the model. In this work, an optimisation process was followed to determine values for the dead time and pile-up digitizer modules, resulting in matching experimental and simulated count rates over a wide activity range.

10.4.5.2/ VALUE OPTIMISATION

The first step is to find the values that allow a match between the simulated and experimental single count rates obtained using the NEMA count losses test 9.2.2. This can be done using pile-up only, dead time only, or a combination of both. As it is easier to optimise a single parameter value than a pair of values, the first step was to consider the exclusive use of dead time or pile-up. In this section, the experimental data of the NEMA count losses and scatter fraction standard acquired in 2021 were used (see Section 9.3.2), and the associated simulations followed the methodology described in 10.3.2.

To determine which module to use, the trues count rate provided by the GATE model should be compared with the experimental trues count rate. During the design of the digitizer, the simulated trues and scatter count rates were always higher and lower than the experimental ones, respectively. As mentioned in Section 10.4.5.1, only the pile-up can affect the true-to-scatter ratio. Therefore, only the pile-up value needs to be tuned. It has been empirically optimised by minimising the relative difference between the simulated and experimental single event rates through multiple simulations at the highest activities. The structural level at which the pile-up is applied is chosen by the user. For consistency with the depth of the readout level, the pile-up was applied at the rsector level in our model. For this first step, a value of 16 ns was found to be optimal for matching single rates, giving a maximum relative difference between experimental and simulated single rates of 1.3%. These single rates are shown in Figure 10.13.

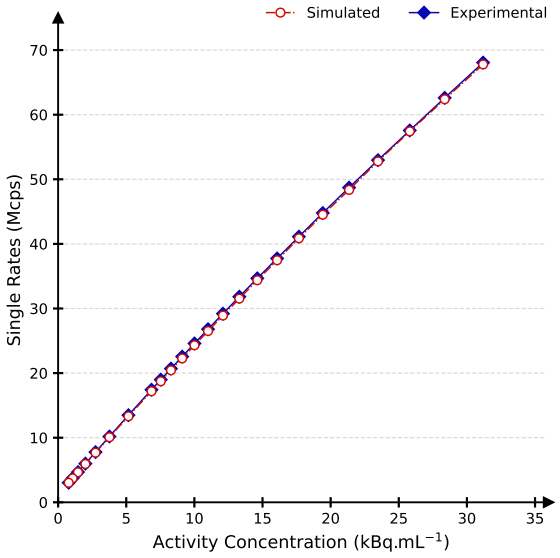

Figure 10.13: Optimisation process for the pile-up module, where simulated single rates were matched to experimental single rates.

The experimental and simulated event rates, analysed in NEAT according to the NEMA count losses and scatter fraction standard, are shown in Figure 10.14. As can be seen, the simulated true rate is still higher than the experimental rate (up to 23% relative difference). As a result, the GATE model provides a much better simulated NECR than the experimental one (up to 45.2% relative difference). The NECR is one of the most important metrics for characterising a PET system, and the higher the value the better. Although our model provides a very high NECR, it is not representative of the real DMI4 scanner.

A second optimisation step was therefore carried out. A reduction in simulated NECR can be achieved by reducing the true rate, but also by reducing the prompt rate. According to the data presented in Figure 10.14, the simulated prompt rate was higher than the experimental one after the first optimisation step. Therefore, in this second step, the relative difference between the simulated and experimental prompt event rates was optimised. After optimisation, a value of 20 ns was found optimal for the pile-up module, giving a maximum relative difference in prompt rates of 1.6% . The resulting event rates are shown in detail in the NEMA count losses section (see Section 10.5.2). Naturally, this higher pile-up value leads to a small loss in simulated single event rates, resulting in a relative difference of 3.3% for the highest activity frame. As random events were estimated using the RFS method, this difference also affected the random event rates (up to 7.2% relative difference).

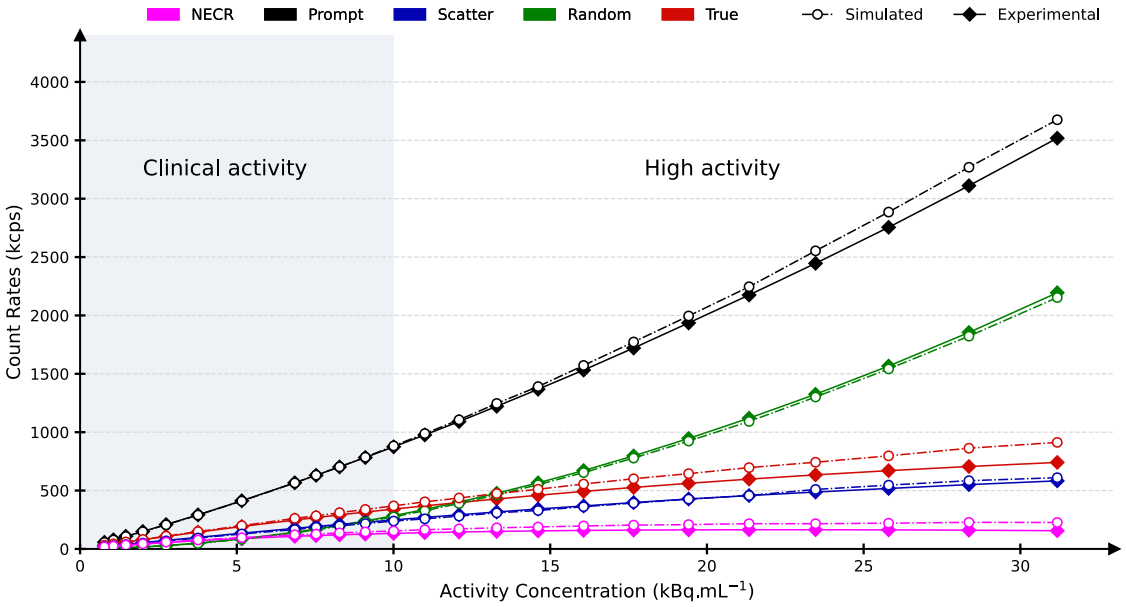

Figure 10.14: Experimental (continuous) and simulated (dash-dotted) count rates with an optimisation process on singles event (16 ns pile-up). Prompt (black), random (green), scatter (blue) and true (red) count rates (kcps) for experimental (continuous) and simulated (dash-dotted) data relative to the activity concentration (kBq.mL^{-1}) are shown. The NECRs are shown in purple.

10.5/ RESULTS

10.5.1/ NEMA SENSIBILITY

Figure 10.15a shows the experimental and simulated sensitivities for all aluminium thicknesses, as well as the extrapolated value obtained for zero absorber sensitivity. The experimental and simulated calculated absorber-free sensitivities at the CFOV were 12.90 cps.MBq^{-1} and 13.37 cps.MBq^{-1}, respectively, showing an agreement of 3.6%. At 10 cm from the CFOV, the experimental and simulated sensitivities were 13.00 cps.MBq^{-1} and 13.38 cps.MBq^{-1}, respectively. Figure 10.15b shows a good agreement between

the experimental and simulated sensitivity profiles, with the largest relative difference in slice-wise sensitivity being 9.9%. Seven CPU days were required for this simulation.

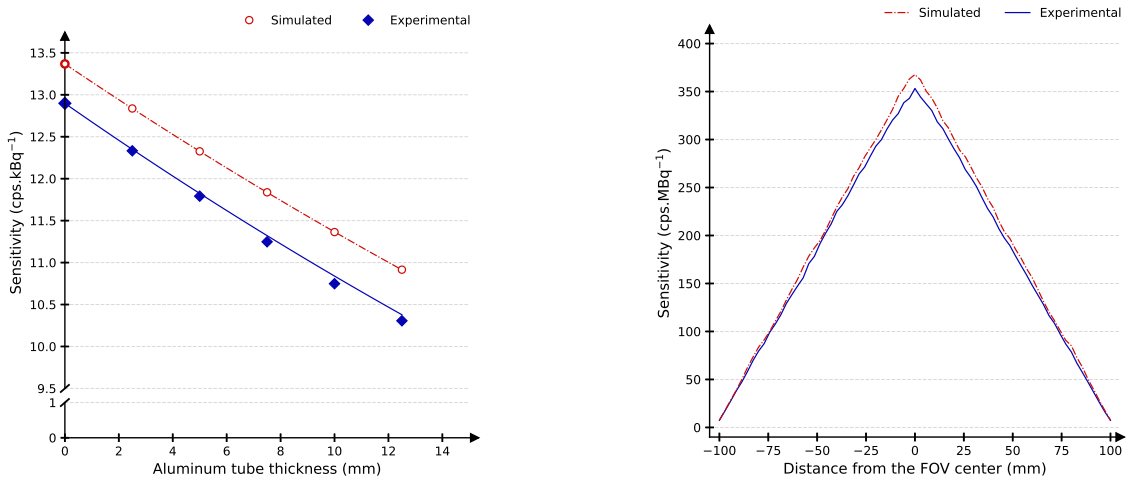

Figure 10.15: (a) The system sensitivity at the CFOV for all aluminium thicknesses and the extrapolated sensitivity as a function of the aluminium sleeve thickness. **(b)** The axial slices sensitivity as a function of the distance from the CFOV. For both figures, experimental (blue) and simulated (red) data are represented.

10.5.2/ NEMA COUNT LOSSES AND SCATTER FRACTION

Figure 10.16 shows count rates calculated according to the NEMA count losses test for experimental and simulated data. Over the full activity range, the maximum relative differences between the prompt, random, scatter, and true coincidences rates were 1.6%, 7.2%, 6.6%, and 15.1%, respectively.

When considering activities closer to clinical activity concentrations (below 10 kBq.mL^{-1}), the maximum relative difference for true count rates was 6.6% (see Figure 10.17). The experimental and simulated NECRs are in agreement by 16.5% within a clinical activity range and by 33.1% over the entire activity range. The peak NECR was at 23.5 kBq.mL^{-1} (164 kcps) and 25.8 kBq.mL^{-1} (208 kcps) for the experimental and simulated data, respectively. The scatter fraction is shown in Figure 10.18, and its values at the peak NECR are 44.4% and 41.3% for the experimental and simulated data, respectively. In total, 157 CPU days were needed to simulate the 24 frames with at least ten million coincidences.

10.5.3/ NEMA SPATIAL RESOLUTION

Table 10.2 shows the spatial resolution in terms of FWHM and FWTM for both simulated and experimental data analysed in NEAT, averaged over both axial positions. The absolute differences ranged from 0.16 mm to 1.24 mm and from 0.65 mm to 1.82 mm for the FWHM and FWTM, respectively. For all positions, the simulated spatial resolution values

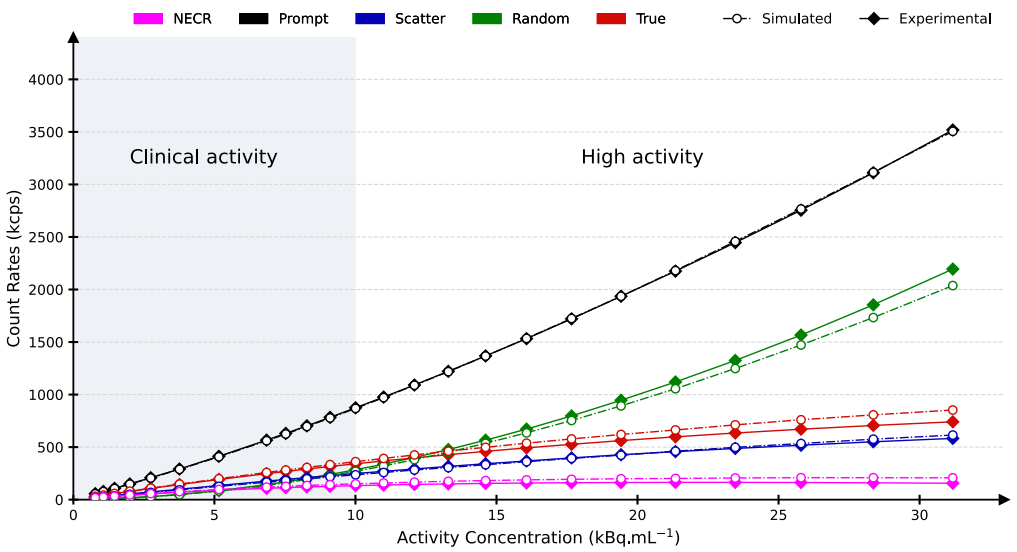

Figure 10.16: Prompt (black), random (green), scatter (blue) and true (red) count rates (kcps) for experimental (continuous) and simulated (dash-dotted) data relative to the activity concentration (kBq.mL^{-1}). The NECRs are shown in purple. The clinical activity range (activity concentration < 10 kBq.mL^{-1}) is outlined.

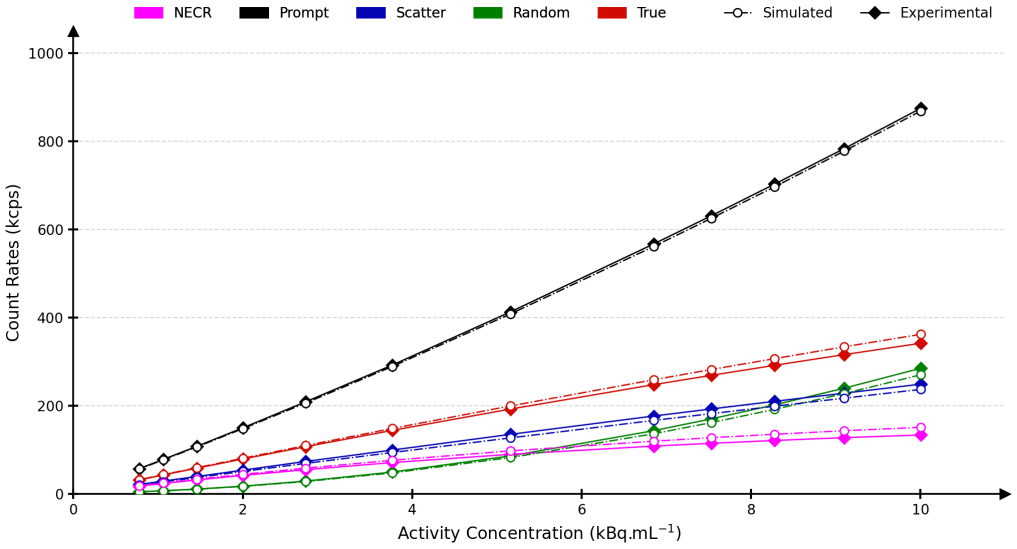

Figure 10.17: Focus on the count rates in the clinical activity range (below 10 kBq.mL^{-1}) shown in Figure 10.16. The legends are identical to this figure.

were systematically smaller than their experimental counterparts. A total of 34 CPU days were used to generate this spatial resolution simulation.

10.5.4/ NEMA IMAGE QUALITY

The CRC, BV and IR for the experimental and simulated VPFX-CLIN reconstructions are shown in Figure 10.19. A visual comparison of the central axial slice for the experimental

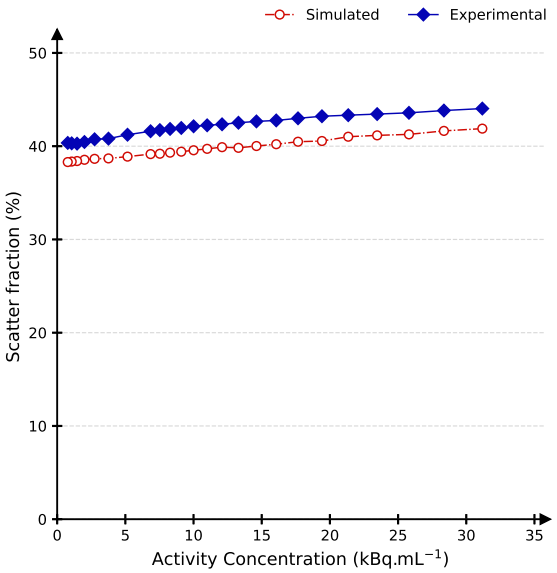

Figure 10.18: The scatter fraction (%) for experimental (continuous) and simulated (dash-dotted) data relative to the activity concentration (kBq.mL^{-1}).

Table 10.2: Spatial resolution in terms of FWHM and FWTM (mm) for experimental and simulated data.

Resolution	**Experimental**		**Simulated**		Difference (mm)	
Direction	FWHM	FWTM	FWHM	FWTM	FWHM	FWTM
1 cm radial offset						
Radial	4.34	8.48	3.37	7.53	−0.98	−0.96
Tangential	4.17	8.20	3.64	7.47	−0.54	−0.73
Axial	4.49	10.07	4.25	8.26	−0.24	−1.82
10 cm radial offset						
Radial	5.66	11.30	5.18	9.97	−0.49	−1.37
Tangential	4.40	9.77	4.10	8.15	−0.31	−1.64
Axial	6.21	11.79	4.98	10.78	−1.24	−1.01
20 cm radial offset						
Radial	7.27	14.35	7.11	13.02	−0.16	−1.34
Tangential	5.10	9.88	4.67	9.21	−0.43	−0.68
Axial	6.29	12.45	5.82	11.81	−0.47	−0.65

and simulated reconstructions is shown in Figure 10.20. The CRC for the experimental and simulated reconstructions showed a maximum relative difference of 14.9% across all spheres. From the smallest to the largest sphere, the background variability ranged from 3.4% to 1.4%, and from 4.0% to 1.6% for the experimental and simulated reconstructions, respectively. A maximum relative difference of 5.7% was found when comparing IR in the background. The experimental lung error was 11.4% while the simulated lung error was 7.5%. When comparing experimental and perfectly corrected (trues only) reconstructions,

maximum relative differences of 17% and 10% were found for CRC and BV, respectively. For the IR, differences of less than 5% were observed and a lung error of 5.4% was measured. This simulation took 161 days of CPU time.

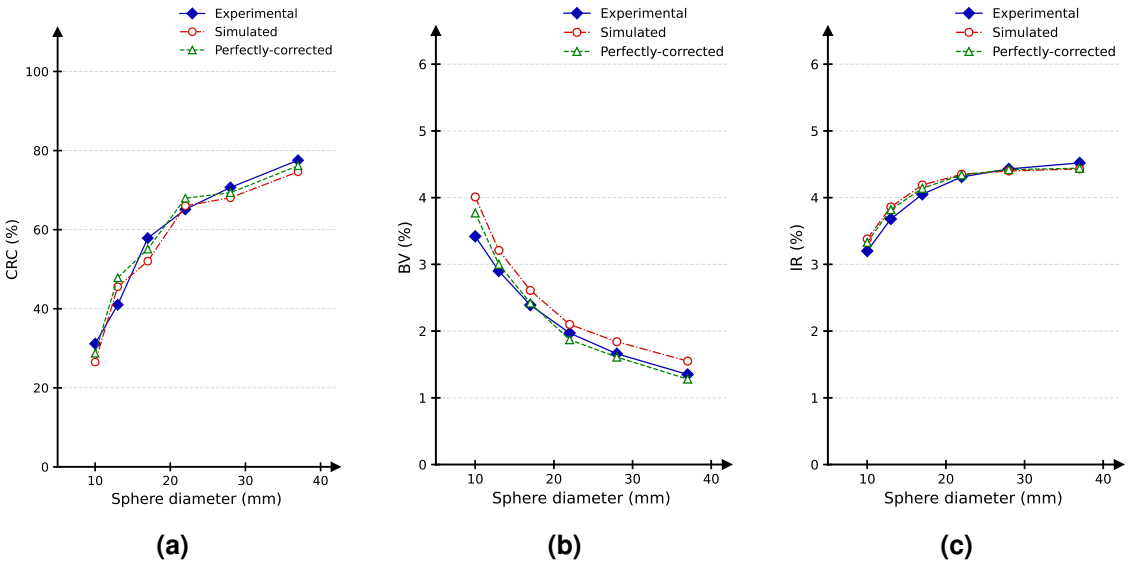

Figure 10.19: Comparison between experimental (blue continuous), simulated (red dash-dotted) and perfectly-corrected (green dashed) contrast recovery coefficient (a), (b) background variability and (c) image roughness for the six hot spheres of the NEMA phantom/model.

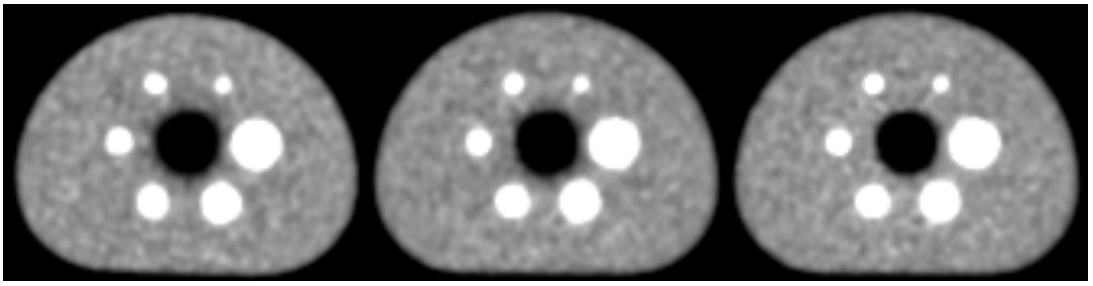

Figure 10.20: Visual comparison between the central slices of the VPFX-CLIN reconstruction of (a) experimental data, (b) simulated data with clinical-like corrections, and (c) simulated data with perfect corrections (trues only). All slices were normalised to their maximum and displayed with the same window and level.

10.6/ DISCUSSION

In this chapter, a Monte Carlo model for the DMI4 scanner was presented, and its performance characteristics were evaluated using the NEMA NU2-2018 standard. This GATE model is capable of mimicking experimental count rates over a wide range of activity, as well as generating clinical-like images through the use of the PET toolbox. During the development of the model, special care was taken to use only clinical-like information from

the GATE simulated data, resulting in realistic processing of these data. Simulated sinogram data were generated using the methods previously developed for experimental data (see Chapter 9.2), and the NEMA analyses were performed using NEAT for both experimental and simulated data. Whenever possible, the simulations strictly reproduced the experimental acquisition conditions, using the information contained in the experimental HDF files.

The knowledge acquired in Chapter 9 was used to design the GATE model. In particular, the geometry of the system, including detector indexing, lead shielding, and block covers, was reproduced with fidelity. Furthermore, some parameters of the digitizer could be set using the previously obtained experimental data (temporal and energy resolution), while others were determined using specific methods: Salvadori et al. (2020) for background noise and detection efficiency, and a trial-and-error optimisation process to obtain the pile-up value. Finally, some parameters (readout depth, multiple coincidence policy) were chosen to obtain the best match between experimental and simulated count rates. The final digitizer was summarised in Figure 10.10.

To recover inter-block Compton scatter, GE systems use the CSR method, which is able to identify scatter events from neighbouring blocks and combine them into a true event to improve sensitivity (Wagadarikar et al., 2014). As this approach is not currently implemented in GATE, Khalif et al. (2016) proposed to emulate the sensitivity gain by using the TakeEnergyWinner readout policy set at the highest level (setDepth 1) in the digitizer. In our system, the TakeEnergyCentroid readout policy with setDepth 1 was used to match the experimental and simulated sensitivities, resulting in a maximum relative difference of 3.6% between the experimental and simulated system sensitivities.

After optimising count rates at high activity, good agreement was achieved in terms of single events (2.0%) and random counts (7.2%) for activity concentrations up to 31.2 kBq.mL^{-1}. In a clinical range taken pejoratively of less than 10 kBq.mL^{-1} (Renaud et al., 2017), simulated prompt, random, true, and scatter rates, obtained from the NEMA count losses test closely matched the experimental rates, with maximum relative differences of 1.6%, 5.3%, 7.8%, and 6.6%, respectively. At higher activities, the true rates were shown to be in poorer agreement between experimental and simulated data, with an absolute relative difference of 15.1%. Therefore, our model is not able to improve the NECR at very high activities. This could also highlight the limitations of the current version of GATE's digitizer, including its inability to emulate the CSR module.

The spatial resolution of our GATE model was found to have lower nominal values for all sources compared to the DMI 4-ring values, with differences between experimental and simulated FWHM ranging from -0.16 mm to -1.24 mm. This trend is common to all GATE-simulated PET (Schmidtlein et al., 2006; Lamare et al., 2006; Li et al., 2017; Khalif et al., 2016) as there is no digitizer module that allows spatial blurring for general PET scanner models. This less important spatial blurring (in the simulation) arises from effects that are not properly accounted for in the simulation, such as Anger logic and crosstalk between crystals. This digitizer shortcoming is often corrected by applying blur to the radial axis of the prompt and random sinograms (Schmidtlein et al., 2006; Li et al., 2017; Khalif et al., 2016) to achieve a closer match between experimental and simulated spatial resolution.

Our reconstruction framework is based on the manufacturer's clinical software, which allows the use of similar reconstruction and correction methods between experimental and simulated data, resulting in good visual similarity when comparing reconstructions (see Figure 10.20). When using clinical-like corrections (normalisation, attenuation, random

and scatter), CRC and BV were relatively close between experimental and simulated reconstructions. However, the trend for the simulated CRC as a function of sphere size is not as stable as the experimental one. This might be due to the use of a single simulated image for the analysis, whereas three images were used for the experimental study. When investigating the perceived image noise in an image, IR is usually more appropriate than the NEMA BV metric, as IR measures pixel-to-pixel variation rather than homogeneity between regions (Tong et al., 2010). Regarding IR, a better agreement (5.7%) was found between simulated and measured images. Although the reconstruction kernel is the same, small discrepancies are expected due to the use of GATE-generated data to perform the normalisation and attenuation correction on the simulated data. For example, the use of different attenuation maps could contribute to the observed differences in lung error (Kalaitzidis et al., 2022). Furthermore, when reconstructing the simulated true counts (mimicking perfect random and scatter corrections), CRC, BV and IR were found to be in better agreement with the experimental measurements (see Figure 10.20), suggesting that some small improvements could still be achieved when applying these two clinical-like corrections (RFS and model-based scatter) to simulated data. Finally, decay (during acquisition), well-counter, and dead time corrections for simulated data have not yet been implemented in the current version of the reconstruction framework. Therefore, the model is capable of producing realistic but not quantitative images in kBq.mL^{-1}.

At the beginning of this thesis (2019), no model of the DMI scanner was proposed in the literature. However, two DMI 4-ring GATE models were published after 2019. Firstly, Tiwari et al. (2022) focused on establishing a GATE model of the DMI4 scanner to then investigate virtual DMI models with extended axial FOVs, up to two metres. To evaluate their DMI4 model, the NEMA sensitivity and count losses standards were simulated and compared with experimental results published in another study (Hsu et al., 2017). Reconstructions were performed using the Software for Tomographic Image Reconstruction (STIR) software only to evaluate the spatial resolution of their model. They found good agreement between simulated and experimental results (less than 8% relative errors up to 25 kBq.mL^{-1} for count rates and 6.4% for sensitivity). The detailed configuration of their digitizer is not shown in this publication and therefore cannot be fully compared with ours. However, it should be noted that there is no background noise in their digitizer and no patient bed in their geometry. Some comparisons can also be inferred from their sensitivity and count rate results. Firstly, our modelled slice-based sensitivity profile shows no inter-ring offset, just like the experimental one. Secondly, the general shape of our simulated count rate curves is similar to the measured curves over the entire activity range and never crosses.

The second DMI4 GATE model is proposed by Kalaitzidis et al. (2022). In their study, they focused on a pipeline to allow reconstruction of GATE data using Customizable and Advanced Software for Tomographic Reconstruction (CASToR). They compared their simulated CASToR reconstruction with experimental data reconstructed using the PET toolbox and CASToR. Their GATE digitizer is detailed and quite similar to ours in the clinical range, except that they followed the approach given by Khalif et al. (2016) to take into account the CSR method. The optimisation of their digitizer leads them to different values of noise and detection efficiency. They did not consider dead time effects in their model, which prevented accurate simulations at high activity. Their image quality acquisition was simulated outside NEMA NU 2-2018 specifications, i.e. without the NECR phantom abutting the IEC phantom, with a SBR of nine, and with a scan time of ten minutes. Their reconstruction parameters were different from ours. It is difficult to

comment on their results because their graph of NEMA metrics (CRC, BV) as a function of sphere size is presented on a very compressed scale. Nevertheless, their simulated CRC seems to be close to the experimental one (within 10%) and their simulated BV also seems to be close when the experimental reconstruction is performed with CASToR, but relatively higher when performed with the PET toolbox. The authors attribute the differences between CASToR and PET Toolbox to the different axial filtering between the two reconstruction packages.

The aim of this work was to provide a general framework for generating realistic PET images from simulated data. The proposed GATE model is able to mimic the count rates of a DMI4 scanner over a wide range of activities, which allows a certain margin for medical applications requiring high activity bolus administration (Renaud et al., 2017). We have also shown that it is possible to reconstruct simulated data using the manufacturer's reconstruction toolbox, provided that adequate calibration data are simulated to calculate the corrections used by the manufacturer. The expected advantages of this method are the ability to use the same reconstruction kernel as that used in clinic, and the simpler implementation of the different corrections required for quantification.

10.7/ CONCLUSION

In this chapter, we detailed the methodology followed to design and implement a GATE model of the DMI4 that mimics the scanner available at the CGFL. The performance of this model was evaluated using the NEMA NU 2-2018 standard and validated against experimental performance. The evaluation framework (data management, analysis, reconstruction) has been designed and developed to allow almost identical processing of experimental and simulated data. This complete framework can be used to generate both perfectly corrected and clinical-like images, and to optimise imaging parameters in several clinical situations.

11

Study of the NEMA NU-2 2018 TOF resolution standard

With the increasing availability of TOF-capable PET systems, the latest version of the NEMA standard (NU 2-2018) introduced the TOF resolution test, based on the work of Wang et al. (2016). As the Gen1 DMI4 scanner available at the CGFL was installed before the release of this NEMA version, the GE console does not include the TOF resolution test. In addition, as the DMI4 is a Gen1 scanner, the TOF data acquired by the system are mashed when recorded, resulting in a loss of precision of the TOF information (see Section 9.1). Nevertheless, this NEMA standard has been implemented in NEAT, and a data pre-processing step is proposed to recover the CTR loss induced by this mashing. To validate the implementation of this test, experimental results were compared with published NEMA TOF resolution results for a second generation (Gen 2) DMI6 scanner, obtained with their GE console. This test was then reproduced in GATE, and the simulated CTR was compared with the experimental one. During the development of the NEAT code for this NEMA standard, several tests were carried out to ensure that the CTR values obtained were correct for both experimental and simulated data. These tests are presented in this chapter.

11.1/ NEMA METHODOLOGY

To perform this test, the data acquired during the NEMA count losses test (see Section 9.2.2.2) shall be used. The count losses acquisitions analysed in Section 9.3.2 were obtained using the manufacturer's acquisition protocol, which recorded each of the 24 frames in a distinct 3D sinogram. For the NEMA TOF resolution standard, the location of each interaction in the system and the TOF information of each coincidence must be accurately known; therefore, a dedicated list-mode acquisition was performed in 2022, following the phantom and source preparation methodology of Section 9.2.2.2. It consisted of a single static list-mode scan recorded for approximately 20 hours, resulting in a very large file (234 GB in compressed format). In order to analyse this file, it was decompressed and exported from the console disk to an external hard drive. This process took over three days and resulted in an even larger file (435 GB). The list-mode acquisition was then rebinned into 24 frames using the event timestamps to match the multi-frame format defined for the NEMA count losses test (see Section 9.2.2.2). During the analysis, 20 million coincidences were retained for each frame. When this test was performed on GATE-simulated data, 10 million prompts were generated per frame in order to obtain a reasonable computation time.

The first step in this analysis was to determine the position of the line source. To do this, the first experimental frame below the NECR peak was reconstructed using the VPHD reconstruction defined in Table 9.2. The centroid of each reconstructed axial plane (excluding those within 10 mm of either end of the axial FOV) was then calculated and a 3D line fitted (least-squares) to these centroids. Using the intersection of this fit with the first and last kept axial planes to define points $\vec{P_1}$ and $\vec{P_2}$, the unit vector, denoted $\vec{v}$, was calculated using Equation 11.1 (see Figure 11.1). For the simulated data, $\vec{v}$ was determined directly from the source position as defined in GATE.

$$\vec{v} = \frac{\vec{P_2} - \vec{P_1}}{\left|\vec{P_2} - \vec{P_1}\right|} \tag{11.1}$$

Once the source position was determined, the following analysis was performed on each time frame. For each coincidence, the spatial coordinates of the associated photons, denoted $\vec{L_1}$ and $\vec{L_2}$, were inferred from the crystal indices contained in the list-mode file. Then, the unit vector $\vec{u}$, from $\vec{L_1}$ to $\vec{L_2}$, was calculated as follows:

$$\vec{u} = \frac{\vec{L_2} - \vec{L_1}}{\left|\vec{L_2} - \vec{L_1}\right|} \tag{11.2}$$

The distance between the LOR and the line source, denoted r, was calculated as follows:

$$r = (\vec{L_1} - \vec{P_1}) \cdot \frac{\vec{u} \times \vec{v}}{\left|\vec{u} \times \vec{v}\right|} \tag{11.3}$$

Since LORs with $r > 21$ mm are too far away from the source to contain true events, they were excluded from further processing. Then the point of closest approach of each LOR to the line source, denoted $\vec{I}$, was calculated as follows:

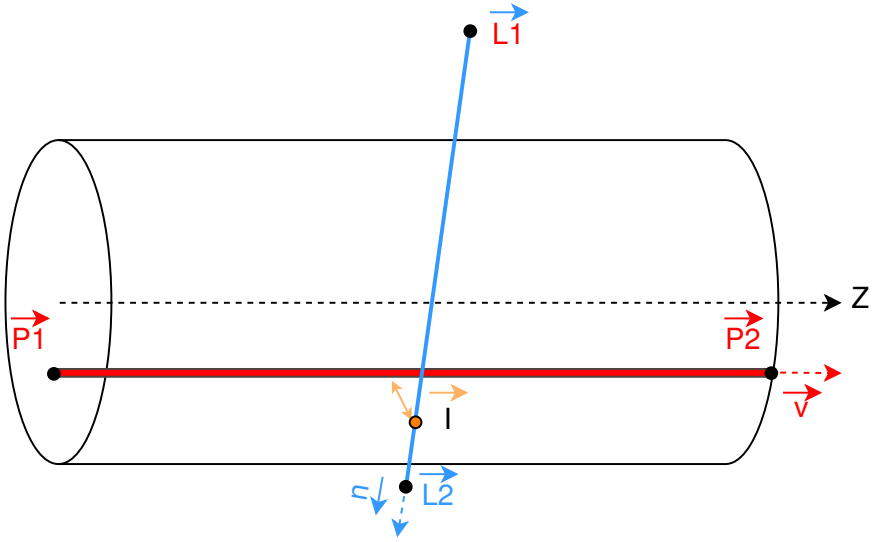

Figure 11.1: Illustration of the cylindrical NEMA count losses model/phantom used for the NEMA TOF resolution test. The line source is shown in red, a LOR is shown in blue, and the shortest distance between the source and the LOR is shown in orange.

$$\vec{I} = \vec{L_1} + \frac{(\vec{L_1} - \vec{P_1}) \cdot (\vec{u} - \vec{v}(\vec{u} \cdot \vec{v}))}{\left|\vec{u} \cdot \vec{v}\right|^2 - 1} \tag{11.4}$$

The timing error, denoted t, was then calculated based on the difference between the recorded TOF information and the expected TOF difference based on the point of closest approach of each LOR to the line source:

$$t = (t1 - t2) - \frac{\left|\vec{L_1} - \vec{I}\right| - \left|\vec{L_2} - \vec{I}\right|}{c}, \tag{11.5}$$

where c is the speed of light, and $t1$ and $t2$ are the TOF data recorded for the two coincidence photons at positions L_1 and L_2, respectively. In this equation, the timestamps provided by the electronics of the system are compared with the theoretical TOF information estimated from the spatial information of both the LORs and the source. All events for which $|t|$ was substantially greater than the expected FWTM (683 ps) were discarded as they were not participating in the subsequent processing.

Each coincidence was then accumulated into a 2D histogram, denoted $H(r,t)$, indexed by the distance between the LOR and the source r and the timing error t. Each 2D histogram had a size 41 $\times$ 29 bins, giving a resolution of 1.03 (mm) $\times$ 47.14 (ps), which was in compliance with the NEMA standard.

To remove scatter and random events from $H(r,t)$, the methodology presented in Section 9.2.2.2 (see Figure 9.5) was followed. As this correction method had already been developed (and validated) in NEAT, it was used for this analysis. The result of this process was a corrected 1D histogram, containing a number of counts in each time bin t.

The peak of the corrected histogram was determined from this 1D TOF profile using a three-point parabolic fit. The TOF resolution, denoted $\mathrm{CTR}_{\mathrm{mash}}$ and expressed in FWHM (ps), was then obtained by linear interpolation on the profile, based on the two points

adjacent to half of the maximum value. As these two methods (parabolic fit and linear interpolation) have already been implemented in NEAT for the spatial resolution test (see Section 9.2.3.2), they were reused.

11.2/ DATA PRE-PROCESSING

As mentioned in Section 9.1, the coincidence detection for Gen1 DMI4 scanners is performed with a time resolution sampling, denoted S, of 13.02 ps, but the recorded TOF list-mode data are further mashed by a factor of 13, denoted C. This results in a final sampling resolution of $\mathrm{C} \times \mathrm{S} = 169.26$ ps. Figure 11.2a shows a sample of the raw TOF data (Δt) contained in the list-mode file using a bin size of 13.02 ps. The data has been extracted for the first ten million counts of the first frame below the peak NECR. Figure 11.2b is a focus on the central part of the plot (Δt = 0) with the centre of each histogram bin (size 13.02 ps) indicated on the x-axis. From this figure, it can be seen that data are only present every 13^{th} bin, which corresponds to the mashing factor applied (C = 13). This raw data was processed according to the NEMA TOF resolution method described in Section 11.1. All presented 1D histograms of t were extracted before random and scatter removal. During the NEMA TOF resolution analysis, only a part of this data is kept (condition on r and on t, see section 11.1). This data is shown in Figure 11.3a and is used to obtain the 1D histogram of the computed timing error t (Equation 11.5) shown in Figure 11.3b.

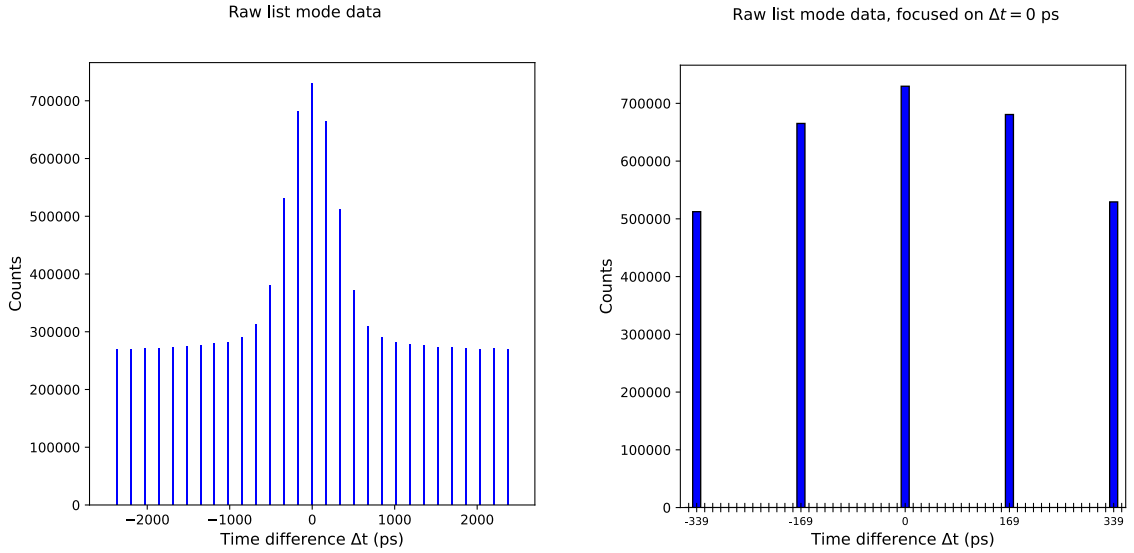

(a) **(b)**

Figure 11.2: Histogram of the raw TOF data extracted from the experimental list-mode file using bin sizes of 13.02 ps. **(a)** shows a large portion of this data, and **(b)** shows only a smaller portion of the data, with 13.02 ps bins marked on the x-axis.

Although scatter and random events have not been corrected at this point, it is apparent that the data shown in Figure 11.3b cannot be used to extract a FWHM. According to Wang et al. (2016), this histogram should have a Gaussian shape and zero mean. Although the mean of the data is close to zero (-1.65 ps), it is clear that it is not Gaus-

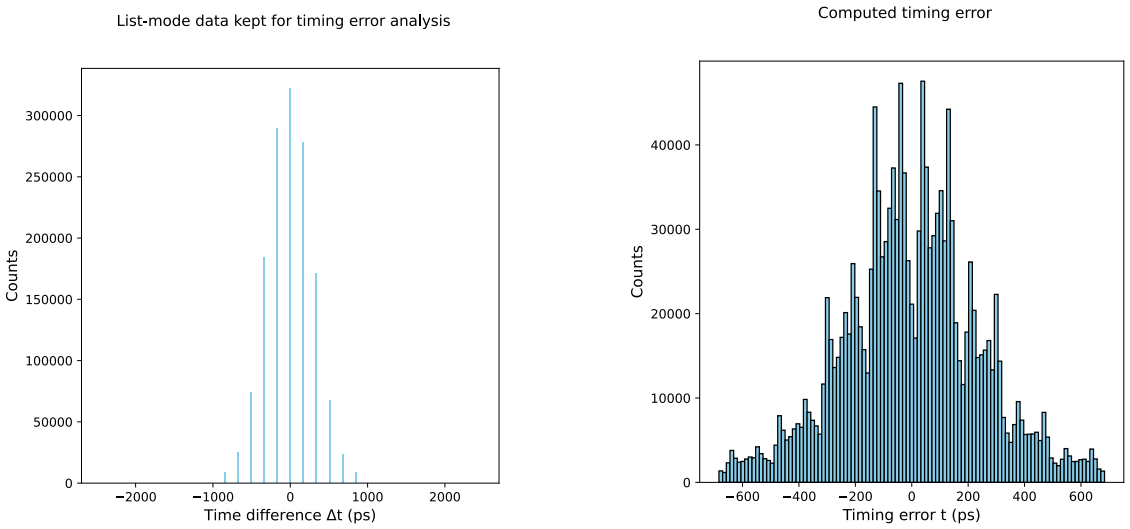

(a) **(b)**

Figure 11.3: Histograms of **(a)** processed TOF data and **(b)** the resulting timing error (bin size 13.02 ps).

sian, preventing further processing. This is due to the loss of information induced by the mashing of the TOF data into 169.26 ps bins. Combined with a finer estimation of LORs positioning during the estimation of r, the mashed TOF data is not fine enough to compute t. Nevertheless, an alternative approach was taken to be able to perform this NEMA standard on a Gen1 DMI scanner. Each of the non-zero bins (169.26 ps apart) of Figure 11.2b was redistributed to the 13 nearest bins of size 13.02 ps. To do this, the counts contained in each populated bin were distributed to the 13 smaller bins using a uniform number generator. Figure 11.4a shows the resulting TOF data, and Figure 11.4b shows the part of the data that was kept during the analysis.

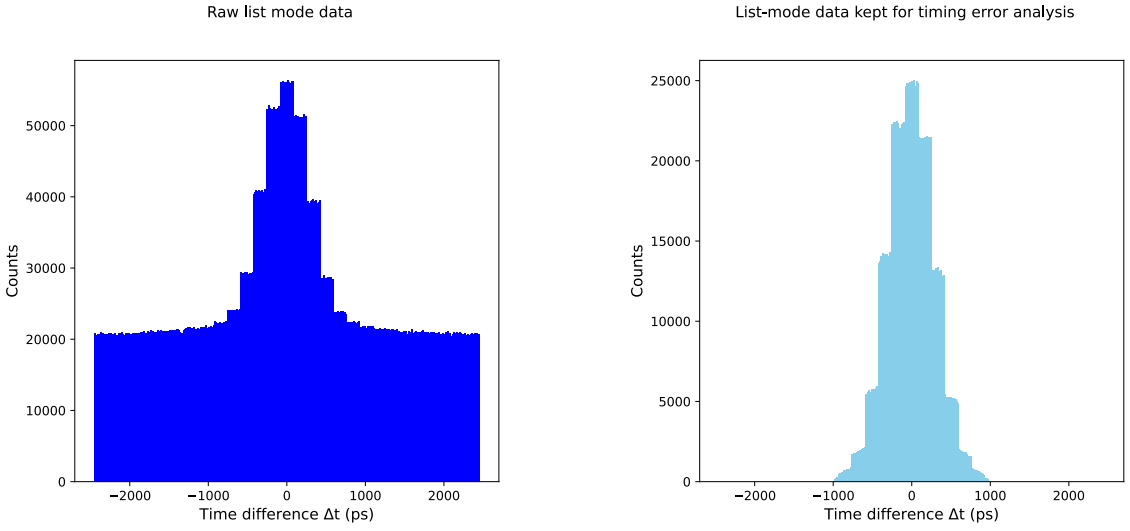

(a) **(b)**

Figure 11.4: Histograms of **(a)** the initial TOF data redistributed over 13-ps bins and **(b)** the TOF data kept during the NEMA process.

Although this method did not provide a way to recover the information lost during the mashing process, it improved the estimation of the timing error, as shown in Figure 11.5. Following the uniform re-distribution of the original data into smaller bins, the timing error histogram now has a Gaussian shape with a mean close to zero (-1.96); these data could then be correctly processed to assess the CTR of the DMI4 scanner according to the NEMA guidelines.

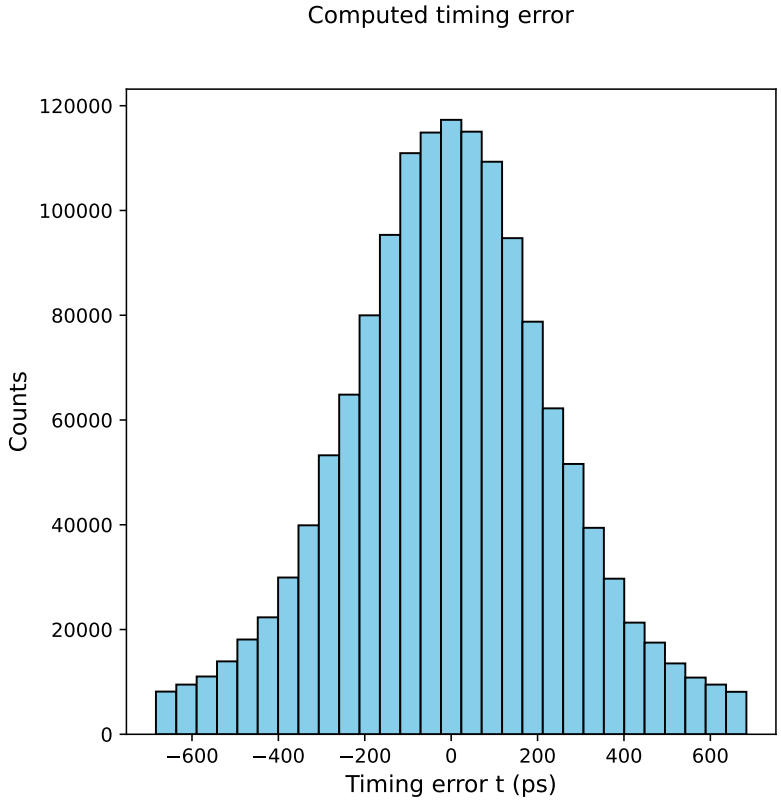

Figure 11.5: Histogram of the timing error calculated after the proposed pre-processing step. The resulting data is Gaussian with a mean close to zero. The data is histogramed over 29 bins in accordance with the sampling requirements of the NEMA report (see Section 11.1).

This pre-processing method was applied to all the frames of the experimental data analysed in order to obtain a CTR value, denoted $\mathrm{CTR}_{\mathrm{mash}}$. Throughout this thesis, an important amount of work was performed not only to propose a GATE model that is an accurate representation of the DMI, but also to ensure that the performance characteristics of the model are identical to those of the real system. With this spirit in mind, the simulated data were deliberately degraded to mimic the recording of TOF data in Gen1 systems. The simulated TOF information was first sampled into 169.26 ps bins (mimicking the experimental mashing factor), and each non-zero bin was then uniformly redistributed over 13 smaller bins of 13.02 ps, as described earlier. This redistributed data was then processed according to Section 11.2 to obtain the simulated $\mathrm{CTR}_{\mathrm{mash}}$.

As mentioned above, this pre-processing method allowed us to calculate the NEMA TOF resolution, but without recovering the loss of information due to the mashing process. To account for this degradation, an empirical correction factor was proposed in Equation 11.6, assuming a Gaussian distribution of the data. This correction was applied on the

calculated $\mathrm{CTR}_{\mathrm{mash}}$ values to obtain the final result, denoted $\mathrm{CTR}_{\mathrm{cor}}$. This correction factor was studied using GATE simulations in Test 2 of Section 11.4.3.

$$\mathrm{CTR}_{\mathrm{cor}} = \sqrt{\mathrm{CTR}_{\mathrm{mash}}{}^2 - \left[2\sqrt{2\ln(2)} \times \frac{CS}{\sqrt{6}}\right]^2} \tag{11.6}$$

In this expression, the term in square brackets represents the uncertainty contribution induced by the use of mashed data in the NEMA process:

- $2\sqrt{2ln(2)}$ is the term used to obtain a Gaussian FWHM from its standard deviation,
- $CS/\sqrt{6}$ is the derived global standard deviation of the uncertainty introduced by the mashing and processing steps. It is the quadratic sum of the errors associated with (i) the mashing of a uniformly sampled distribution [0, CS] by a factor C, ($CS/\sqrt{12}$), and (ii) the uniform up-sampling from bin size CS to bins of size S ($CS/\sqrt{12}$).

11.3/ RESULTS

Figure 11.6 shows the CTR as a function of the activity concentration AC for the experimental and simulated data points, as well as a linear fit using these points. As the time-of-flight resolution test was not available in the manufacturer's software for our Gen1 DMI4 scanner, the NEAT implementation of this standard cannot be directly validated using the GE console. Instead, we decided to compare the NEAT results with published data obtained on a Gen2 system. In fact, Gen2 DMI scanners were made available after the release of the NEMA NU 2-2018 standard, and their Gen2 GE console includes an implementation of the NEMA TOF resolution test. In their work, Zeimpekis et al. (2022)

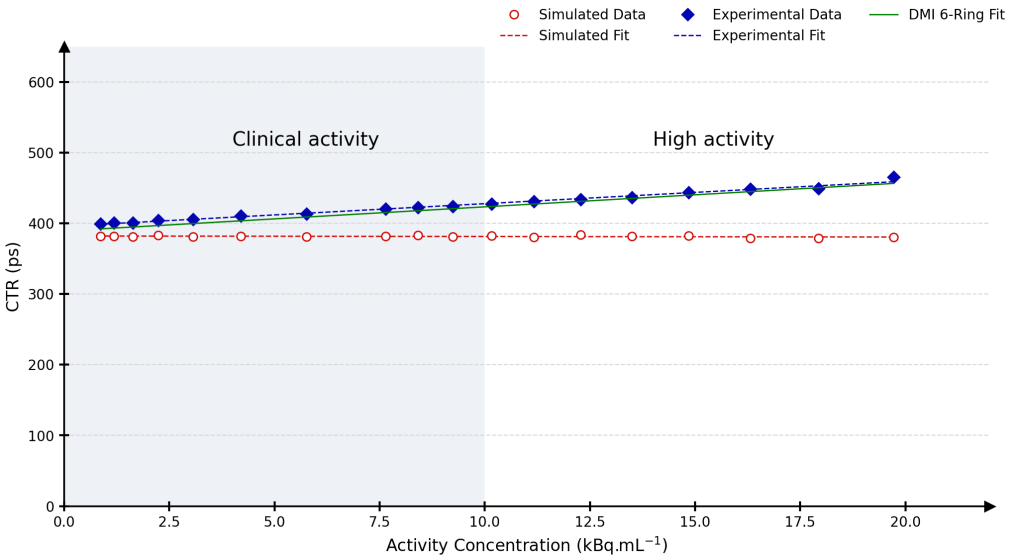

Figure 11.6: Experimental (blue) and simulated (red) CTR data points and the associated fits. The green fit is adapted from the time-of-flight resolution results presented by Zeimpekis et al. (2022) for a DMI6 scanner.

performed the NEMA TOF resolution standard on their DMI6 scanner. As a result, an additional linear fit (adapted from their work) is shown for their DMI6 scanner.

The linear fit equations for the experimental DMI4 scanner, the proposed GATE model, and the experimental DMI6 scanner are $\mathrm{CTR_{cor}} = 3.19\mathrm{AC}+395.9$, $\mathrm{CTR_{cor}} = -0.07\mathrm{AC}+382.1$ and $\mathrm{CTR} = 3.41\mathrm{AC} + 389.2$, respectively. The experimental data show a slight increase in the CTR value with respect to the activity concentration, while the simulated CTR values are more stable over the activity range with an average value of 381.4 ps.

11.4/ GATE STUDY

11.4.1/ AIM OF THE STUDY

As the TOF resolution test has only recently been codified in the NEMA standard, the temporal resolution of the DMI4 scanner is measured using a protocol defined by the manufacturer (see Section 9.2.6.2). Using this protocol, the temporal resolution of our DMI $\mathrm{CTR_{CTC}}$, was 375.05 ± 3.79 ps, which was in good agreement with other values reported in the literature, using the same protocol (see Section 9.3.6). In the proposed GATE model, a CTR value of 376 ps was set in the digitizer (see Section 10.4.2 and Figure 10.10).

When performing the NEMA TOF resolution test on experimental data, a CTR_{cor} value of 395.9 ps was found. This differs by 5.5% from the $\mathrm{CTR_{CTC}}$ value obtained following the manufacturer's protocol. In the literature, Zeimpekis et al. (2022) reports a CTR value of 389.2 ps for a DMI6 scanner, showing a relative difference of 3.8% with $\mathrm{CTR_{CTC}}$. Finally, a value of 382.1 ps was found for the proposed GATE model of the DMI4.

These results are unexpected, especially for the simulated CTR, since a value of 376 ps was explicitly set in the digitizer. In order to confirm these results (376 ps expected versus 382.5 ps obtained), several tests were carried out on simulated data to identify the origin of the observed difference. These are presented in the following sections.

11.4.2/ GATE READOUT POLICY

In the TOF resolution studies performed during this thesis, differences in the effects of the TakeEnergyWinner and TakeEnergyCentroid readout policies were noted. To the best of our knowledge, these differences are not mentioned in the GATE documentation, nor in the literature related to the validation of GATE models of PET scanners. Although these differences are part of the results of the TOF resolution studies, they are mentioned now to provide a better understanding of the reported results.

In the output of a GATE simulation, the recorded singles and coincidences contain information about the coordinates of the interaction in the crystals. This information can be found in two different representations.

In the first representation, each crystal is encoded by a unique combination of the crystalID, submoduleID (block), moduleID and rsectorID fields. Using LUTs which associates a crystal identifier with a spatial position, the recorded unique crystal identifier (see Section 10.2.2) can be used to assign a spatial position to each event. Using this represen-

tation, the only difference in events location between TakeEnergyWinner and TakeEnergyCentroid is due to their working principle (i.e. maximum energy or Anger's logic).

In the second representation, the interaction position in the detector ring is recorded using the spatial coordinates found in the fields globalPosX, globalPosY, and globalPosZ. The values stored in the globalPos fields will be fdifferent according to the readout policy used. With TakeEnergyCentroid, the values of the three globalPosare set at the centre of the crystal, even if the centroid-weighting has only been performed on one event. In contrast, when TakeEnergyWinner is used, the **exact location** of the interaction within a crystal is stored in the three globalPos fields. In this case, the spatial information of the detected photon is perfectly accurate.

11.4.3/ TEST REPORTS

According to Section 11.3, the simulated CTR values were mostly stable over the activity range considered. This is to be expected as there is no module in GATE that simulates CTR degradation as a function of dead time. Therefore, to speed up the analysis and simulation processes, only the first frame below the NECR peak frame of the NEMA count losses was simulated for each test. When necessary, true events were extracted using Algorithm 1. For all tests, the number of bins in the 2D histograms was fixed to 45 $\times$ 29, giving a resolution of 1.18 (mm) $\times$ 47.14 (ps).

REFERENCE SIMULATION

The aim of this simulation was to obtain as few biases as possible in the estimation the TOF resolution. To this end, the following simulation parameters were used:

- The value of the timeResolution digitizer module was set to 376 ps;
- The TakeEnergyWinner readout policy was used in conjunction with the globalPos representation of the event location, allowing perfect LOR placement during the NEMA analysis.
- No time mashing was performed, i.e. the timestamps recorded in the GATE list-mode file were used (no sampling);
- A back-to-back source is used, eliminating the temporal variability caused by the positron range, ensuring that all the annihilations take place at the source location;
- A very small source radius of 0.01 mm was placed in the NEMA count losses phantom to avoid variability in the back-to-back emission location;
- 500 000 true counts were analysed, removing any possible inaccuracy of the random and scatter correction process;

With this setup, a TOF resolution of 380 ps was calculated with NEAT. The observed difference from the expected 376 ps was probably due to small analysis uncertainties (2D histogram resolution, statistics). To verify the effect of count statistics, the NEAT analysis was reproduced on the same simulated data, but with only 100 000 true counts (20% of the initial amount). With this lower statistic, a CTR value of 382 ps was found, showing that our test results may indeed be subject to statistical uncertainty.

TEST 1: TIME-MASHING

The simulated data from Test 1 were reused for this test. The aim was to investigate the effect of the TOF data mashing and in particular the accuracy of the CTR correction method proposed in Equation 11.6. Following the methodology proposed for the experimental data (see Section 11.2), the simulated TOF data associated with 500 000 true events were sampled into time bins of size 169.26 ps, and the data from each bin were then uniformly redistributed into 13 bins of size 13.02 ps. When analysing the time-mashed true events, the obtained $\mathrm{CTR}_{\mathrm{mash}}$ was 413 ps. When $\mathrm{CTR}_{\mathrm{corr}}$ was calculated using Equation 11.6, a value of 380 ps was found, which was the value found for Test 1 when no time-mashing was performed using the same true counts.

TEST 2: SCATTER AND RANDOM REMOVAL

The simulated data from Test 1 were reused for this test, but 500 000 prompt counts (rather than true counts) where analysed to assess the effect of the random and scatter correction on TOF resolution (Test 2a). During the analysis, random and scatter counts were removed using NEAT. After correction, a CTR of 378 ps was obtained for this test. The analysis was reproduced using ten million counts (Test 2b) and the resulting CTR was 383 ps, showing that statistical uncertainty may also affect the study of prompt events.

TESTS 3 & 4: POSITRON RANGE AND SOURCE RADIUS

In the previous tests, a back-to-back source was used in combination with a very small source radius to obtain a thin line of annihilations. The simulation of Test 1 was reproduced twice: once with a positron source (Test 3), and again with a 1.6 mm line source (standard size, Test 4). For both tests, the CTRs obtained were 381 ps (versus 380 ps for Test 1), showing little to no effect of these parameters.

TEST 5: LOR POSITION

The simulation methodology of Test 1 was followed except that the readout policy was set to TakeEnergyCentroid instead of TakeEnergyWinner. No other changes were made to the methodology. For each of the newly simulated 500 000 true events, the spatial coordinates were obtained using the globalPos fields in Test 1, but this time only one position per crystal is returned (equivalent to using crystal indices, see Section 11.4.2). This change in readout policy allowed the study of possible differences in CTR when introducing a spatial uncertainty in the estimation of the LORs' position (see Equation 11.5 and Section 11.4.2).

Using the TakeEnergyCentroid readout policy, a CTR value of 387 ps was obtained, which is the largest difference (7 ps) from the initial 380 ps obtained in Test 1. This test shows that spatial uncertainty in the estimation of the LORs' position affects the expected timing error calculated in Equation 11.5. Since the CTR is calculated in terms of FWHM (ps), and assuming that the data are Gaussian, a quadratic difference can be used to quantify the induced bias on the CTR. Using the CTR obtained in this test (387 ps with TakeEnergyCentroid) and the initial CTR of Test 1 (380 ps with TakeEnergyWinner), a value of

$\sqrt{387^2 - 380^2} = 75$ FWHM ps was found.

SUMMARY

The results of Section 11.4 and the manufacturer's protocol are summarised in Table 11.1. The results of our simulated tests are reported in Table 11.2. For each test, we sought to isolate the influence of a single parameter on CTR.

Table 11.1: CTR values for the DMI4 (experimental and simulated) and DMI6 (experimental only) evaluated using the NEMA TOF resolution standard. The CTR value obtained using the manufacturer's protocol is also given (the reported activity is the net activity contained in the line source used for this test).

Method	Mashing + correction factor	Activity	CTR (FWHM ps)
NEMA DMI4	Yes	0 kBq.mL^{-1}	396
NEMA GATE model	Yes	0 kBq.mL^{-1}	382
NEMA DMI6 Zeimpekis et al. (2022)	No	0 kBq.mL^{-1}	389
Manufacturer's protocol DMI4	No	20 MBq	375

Table 11.2: Summary of our simulation tests, reporting the effect of different parameters on the TOF resolution calculation. The statistics of each test are also given.

Simulation	Analysed counts	Change from reference setup	CTR (FWHM ps)
Reference simulation	**500k trues**	**None**	**380**
Test 1: Time-mashing	500k trues (reference data)	Mashing + correction factor	380
Test 2a: Scatter and random removal	500k prompts (reference data)	Trues → Prompts + correction	378
Test 2b: Scatter and random removal	10M prompts reference data)	Trues → Prompts + correction	383
Test 3: Positron range	500k trues (new data)	Source type: Back-to-back → Positron	381
Test 4: source radius	500k trues (new data)	Source radius: 0.01 mm → 1.6 mm	381
Test 5: LOR position	500k trues (new data)	TakeEnergyWinner → TakeEnergyCentroid	387

11.5/ DISCUSSION

In this chapter we have applied the NEMA standard to evaluate the TOF resolution of our scanner. As our DMI4 scanner is of an older generation (Gen1), the TOF resolution analysis could not be done using the GE console. For this NEMA analysis, we had to perform a specific acquisition in list-mode. Generating, exporting, and processing the resulting file was a challenging task which could only be accomplished with the cooperation of the manufacturer.

From a purely computer science point of view, the large file size required the implementation of dedicated methods to enable the selection of specific frames and the loading of the associated data. Trade-offs between computational speed and IO load were made to allow the processing of such a large file in NEAT. As a result, the complete processing of a single time frame of 20 million prompt counts (as shown in Section 11.3) took 40 minutes, which leads to 12 hours of processing for the 18 frames. Incidentally, processing the entire file was not realistic, as the complete 76 billion prompt counts would require more than 75 days of processing.

As previously mentioned, the TOF information of Gen1 DMI scanners is mashed. It was shown in Section 11.2 that the mashed TOF data could not be processed directly, as the resulting TOF resolution histogram was not suitable for NEMA processing. In that section it was also shown that the NEMA processing could be performed by re-distributing the mashed data into bins of size 13.02 ps. However, this re-distribution effectively reduced the number of counts in each populated bin by a factor of 13, resulting in the need for a relatively large number of prompt counts per frame analysed (500 000 counts recommended in NEMA, 20 million used in this work). In addition, to account for the degradation of the TOF information induced by the mashing, an empirical correction factor was proposed in Equation 11.6, and studied in Test 1 of Section 11.4.3 on simulated data. According to this test, the empirical correction factor proved to be an estimate of the loss of resolution caused by the time-mashing. The proposed correction factor was therefore applied when processing the mashed experimental data. Finally, using the entire proposed methodology (with a correction factor), the CTR of the DMI4 scanner could be evaluated according to the NEMA TOF resolution test.

Since NEAT could not be directly validated using the GE console, we looked to the literature for points of comparison. The results obtained were compared with those of Zeimpekis et al. (2022), who calculated the CTR using their GE console. In fact, they have a DMI6 scanner equipped with the new generation of electronics (Gen2) with TOF data that are not mashed. Although the benefit of this upgrade to the system's electronics is significant in terms of count rates performance, the CTR performance is expected to remain identical at 0 kBq.mL^{-1} (GE Healthcare, 2016b,a). The difference between the two systems is therefore assumed to come essentially from the approximate correction provided by the empirical factor on our Gen1 DMI4 scanner. According to NEMA NU 2-2018, the CTR obtained at the intercept (0 kBq.mL^{-1}) for the Gen1 DMI4 scanner and the Gen2 DMI6 scanner were 395.9 and 389.2 ps, respectively. As these CTR values were in a 1.8% agreement, the NEAT implementation of this NEMA standard was considered validated.

For simulations with the proposed GATE model, the CTR$_{cor}$ was stable over the whole activity range as expected, since there is no digitizer module in GATE to degrade the TOF resolution with respect to the single rate. The simulated CTR$_{cor}$ value (382.1 ps) differed by 1.6% from the value used in the digitizer (376 ps).

The flexibility of Monte Carlo simulations was used to analyse different simulation setups, which were detailed in Section 11.4.3. As reported in Section 11.4.2, the main finding of the tests was the difference in the data provided by the TakeEnergyCentroid and TakeEnergyWinner readout policies in the globalPos GATE fields. While TakeEnergyCentroid repositions events to the centre of the crystals using Anger's logic, TakeEnergyWinner returns the exact spatial coordinates of events occurring in the detector ring. For the TakeEnergyWinner policy, the recorded TOF information corresponds to the distance travelled by the annihilation photons. On the contrary, as TakeEnergyCentroid repositions the event to the centre of the crystals, the TOF information is no longer directly linked to the distance travelled by the annihilation photons.

During the implementation of the NEMA standard in NEAT, two concerns were raised: (i) the difference between the simulated $\mathrm{CTR}_{\mathrm{corr}}$ (382.1 ps) and the value used in the digitizer (376 ps); and (ii) the difference between the experimental $\mathrm{CTR}_{\mathrm{corr}}$ obtained with NEAT (395.9 ps) and the $\mathrm{CTR}_{\mathrm{CTC}}$ value obtained using the manufacturer's coincidence timing measurement protocol (375 ps).

For the first concern (i), we can use the results of the simulation setups and state that the spatial error induced by TakeEnergyCentroid is about half the length of a crystal, which is 12.5 mm[1]. This distance results in a 83 ps maximum error in the estimation of the TOF information, with respect to the actual interaction coordinates of the photons in the crystals. In Test 5, the CTRs obtained with both readout policies were compared, and the change from exact coordinates (TakeEnergyWinner) to crystal centres (TakeEnergyCentroid) introduced a bias of 75 FWHM ps. Considering that most photons do not interact at the surface of the crystal but at some distance inside it (the mean free path in LYSO crystals is 11.5 mm at 511 keV), the theoretical 83 ps error mentioned above is a conservative estimate. We can therefore assume that the 75 FWHM (ps) error obtained in Test 5 is a reasonable Monte Carlo estimate of the bias introduced by TakeEnergyCentroid when performing the NEMA TOF resolution test. In our GATE model, the readout is performed with the TakeEnergyCentroid policy. If the CTR_{cor} value (382.1 ps) of our model were corrected for the error estimated in Test 5 (75 ps) using a quadratic difference, a value of 375 ps would be obtained, which is very close to the value used in the digitizer (376 ps). Finally, we hypothesise that the uncertainty in the position of the LORs (Test 5) has introduced a spatial error into the second term of Equation 11.5, resulting a higher CTR value when analysing the simulated data produced by our model according to the NEMA TOF resolution standard.

Let us now consider point (ii), the experimental differences between $\mathrm{CTR}_{\mathrm{corr}}$ (395.9 ps) and $\mathrm{CTR}_{\mathrm{CTC}}$ (375 ps). The manufacturer's protocol described in Section 9.2.6.2 is performed using a line source (similar to the NEMA sensitivity source) placed at the CFOV in air along the longitudinal axis of the PET scanner. When estimating the CTR according to the NEMA NU 2-2018 standard, the line source is off-centre and placed in a thicker attenuating medium (NEMA count losses acquisition). As shown by Wang et al. (2016) on the same scanner, the line source setup results in a better CTR due to the absence of scattering medium and a better coincidence fraction (defined as the ratio of the coincidence rate in the energy window to the singles rate in an open energy window). The manufacturer's protocol is based on measuring (usually immediately after calibration) the difference in arrival time of the two photons along a pair of detectors. The NEMA protocol compares this measurement for each LOR, as recorded in the list-mode file, with the expected TOF offset (based on distances), and so depends on data sampling. These arguments are indeed in favour of a standardised methodology for TOF measurement as a function of activity concentration. In our opinion (and that of others) the NEMA TOF resolution measurement, while not free from error, provides a realistic estimate of the CTR in a clinical setting. Taking into account experimental uncertainties, the NEMA results (395.9 ps for our Gen1 DMI4 scanner and 389.2 ps for a Gen2 DMI6 scanner from the literature) are reasonably close to the NEMA specification given by the manufacturer for Gen2 DMI scanners (385 ps at 0 kBq.mL^{-1}, see GE Healthcare (2016a)).

11.6/ CONCLUSION

In this chapter, we have studied the measurement of TOF resolution on our DMI scanner in accordance with the latest NEMA standard. We were able to comply with the standard despite the constraints imposed by a low sampling of the recorded TOF information. A methodology has been proposed to obtain a CTR value from the mashed TOF data.

[1] This error may be slightly higher for photons traversing the crystal along its diagonals.

Using GATE simulations, the accuracy of this factor has been verified and the effect of various parameters on TOF resolution has been studied.

CONCLUSION

The aim of this thesis was to create a complete GATE model of the DMI4 PET scanner.

In order to design and implement our GATE model, we first had to evaluate the performance characteristics of the scanner. These were measured on the CGFL Gen1 DMI4 PET scanner using the manufacturer's tools (GE console) according to the NEMA NU 2-2012 standard. The NEMA performance tests were carried out over several years and were also compared with the performance results available in the literature for other DMI4 systems.

Using the raw data from the performance evaluation, we then designed, implemented and validated a software named NEAT. In terms of design, this software was divided into two main parts: clinical data management and NEMA analyses. The data management tools were designed to automate the extraction of information from raw DMI4 data and to reorganise it into different representations (in particular 3D+TOF, SSRB, and RFS sinograms). The NEMA NU 2-2018 analyses were implemented in NEAT and validated by comparing the results of NEAT with those of the GE console over several years.

To design our DMI4 GATE model, we first relied on experimental information: the geometry of the model was implemented according to publicly available information (detector ring shape). The geometry was improved thanks to discussions with the manufacturer, in particular to implement the lead shielding present on both sides of the detector ring, and to reproduce crystal indexing and spacing similar to the experimental ones. The methodology used to design, implement, and define the values of the digitizer modules has been detailed. The remaining digitizer values, namely background noise, detection efficiency, and pile-up, were determined through optimisation processes. All GATE files related to our GATE model ('.mac' files) were integrated into NEAT.

To be able to analyse the simulated data, additional methods were implemented in NEAT. Specifically, data management methods were developed to reorganise the simulated data into clinical-like sinograms. The previously validated NEAT implementation of the NEMA analyses was used to evaluate the performance our GATE model. Throughout this thesis we have taken particular care to treat the simulated data as if it had been obtained experimentally using the DMI4.

To perform the reconstruction of simulated data, we have developed a reconstruction framework (simulation package) based on the PET toolbox. We have proposed and validated a methodology to generate the simulated files required by the PET toolbox for random, attenuation, and normalisation corrections. In its current implementation, the simulation package can perform tomographic reconstructions of simulated data using different algorithms (FBP, OSEM, and TOF-OSEM) and corrections (random, scatter, attenuation, normalisation). The implementations are the same as those of the manufacturer.

To complete the NEMA NU 2-2018 performance evaluation of our GATE model, we had to study its TOF resolution. Since this NEMA test was not implemented in the GE console, and because our Gen1 DMI4 system only records mashed TOF information, the acquisi-

tion and analysis of the required experimental data were challenging. Nevertheless, we studied this NEMA standard and proposed a methodology for evaluating the TOF performance of Gen1 DMI scanners. To allow a fair comparison between experimental and simulated data, the TOF information mashing was first applied to the simulated data, and the simulated CTR was then evaluated following the experimental methodology. In addition, we have reported some of our tests dedicated to the study of the different parameters that can affect the CTR values.

The proposed methodology and framework allowed us to adequately validate our GATE model by comparing its performance with that of the DMI4 installed at the CGFL using the NEMA NU 2-2018 standard. We can reasonably conclude that our GATE DMI4 model is capable of producing simulated data and images that are very similar to the clinical data and images obtained with a DMI4 scanner.

Since the start of this thesis, a lot of time has been spent on establishing a reliable framework for comparing experimental and simulated data. Nevertheless, further improvements to the simulation package could be envisaged. At the end of this thesis, PSF correction of simulated data could be achieved in the simulation package. However, we did not use it because we did not have time to study the results in detail. Regarding the simulated PET data corrections, three corrections remain to be implemented, namely decay, well-counter, and deadtime corrections. As these corrections were not necessary to perform most of the NEMA analyses (only needed for the NEMA accuracy of corrections test), they were set as additional objectives. At the end of this thesis, we were working on the implementation (in the simulation package) of the decay correction and well-counter calibration to obtain quantitative images (in $Bq.mL^{-1}$) at low activities[2]. This was part of our effort to enable the BSREM (Q.Clear) reconstruction of simulated data, which could not be achieved in the time available. The ability to reconstruct simulated data using the latest iterative algorithms would be a major advantage in optimising PET reconstruction parameters. Finally, another method that does not require the reconstructed FOV to be reduced (64 cm versus 70 cm for the experimental data) could be developed to generate the calibration files required by the simulation package.

In GATE models, the readout level is often set to the highest level (depth 1, at the rsector level) in order to obtain the highest sensitivity. This approach was used in our case to emulate the CSR in particular. If a CSR method had been available in GATE or if we had had time to implement such a method, we could have reduced the depth of the readout. Combined with the TakeEnergyCentroid readout policy, this would have better modelled the DMI4 Anger's logic, as it is performed at the block level (depth 3).

In this work, we showed that the performance of our model was very similar to that of the DMI4 of the CGFL. The largest differences were observed for the NEMA count losses and scatter fraction test, where the simulated true count rates were higher than the experimental ones. Incidentally, the peak NECR of our model was also higher than the experimental one. In GATE, optimising the count rates of a model at very high activities is often a challenging task, and our case was no exception. Optimising the count rates of our model has been an ongoing task throughout most of the thesis, where several digitizers have been designed and optimised to reduce the true count rates at very high activity. In this thesis, we have presented the optimised digitizer that provides the closest match between the NECRs of our model and the actual DMI4 scanner while matching the prompt rates of both systems. We hypothesise that the lack of CSR in GATE played a

[2] To obtain quantitative images at high activities, the deadtime correction would be needed.

role in the high true count rate of our model. If it were to be implemented, we believe that a new optimised digitizer would give a better match in terms of true count rates.

In our research group, the focus is on improving PET imaging, specifically on the topics of dynamic PET acquisition. The Monte Carlo model of the DMI created during this thesis can facilitate research related to this topic. One example is the work of two masters students, who studied the simulation of dynamic data using the proposed GATE model: F. Sayah in 2021 (Sayah, 2021) and H. Jozi in 2022 (Jozi, 2022). Briefly, they developed a simulation environment based on the definition of realistic time-dependent activity sources. Using digitised anatomy from real patients and image-derived time-activity curves, they developed a pipeline to reproduce clinical dynamic PET/CT acquisitions of patients in GATE. By the end of their master, they have shown proof of concept by simulating complete dynamic acquisitions as a sequence of several static acquisitions whose activity in defined regions evolves according to time-activity curves. For future applications, we want to use our GATE model to study the denoising of both static and dynamic PET images using deep learning approaches. In most state-of-the-art methods, the target noise-free reconstructed images are not available. Therefore, they use clinical images (target) that they degrade (by adding more noise or reducing the count statistics) to obtain a training set, composed of both noisy and noise-free images. With our validated model of the DMI4, we want to investigate an approach where the simulated annihilation location is used to generate the noise-free target data. In such a case, the generated target data would truly represent the activity distribution desired in PET imaging, as it would not be degraded by the acquisition and reconstruction processes. An additional advantage of this approach lies in the availability of the target data: it would not be limited by the number of clinical examinations performed, but only by the computing power used for the simulations.

PUBLICATIONS

ARTICLE IN PEER-REVIEWED JOURNAL

A. Merlet, B. Presles, K.-H. Su, J. Salvadori, F. Sayah, H. Jozi, A. Cochet, and J.-M. Vrigneaud. Validation of a Discovery MI 4-ring model according to the NEMA NU 2-2018 standards: from Monte Carlo simulations to clinical-like reconstructions. EJNMMI Physics, 2024. (Accepted)

J. Salvadori, **A. Merlet**, B. Presles, J. Cabello, N. Anizan, K.-H. Su, A. Cochet, A. Etxebeste, J.-M. Vrigneaud, D. Sarrut. PET digitization chain for Monte Carlo simulation in GATE. (Draft, planned for a submission in PMB)

ORAL PRESENTATIONS IN INTERNATIONAL CONFERENCES

A. Merlet, B. Presles, A. Cochet, J.-M. Vrigneaud. Monte Carlo simulation of a last generation PET scanner: preliminary results according to the NEMA NU2-2018 standard. Eur J Nucl Med Mol Imaging, Vol 48, Suppl 1, S181. EANM - *virtual*, 2021.

A. Merlet, J. Salvadori, A. Cochet, B. Presles, J.-M. Vrigneaud, Modeling the GE Discovery MI scanner in GATE: optimization of the digitizer. IEEE Medical Imaging Conference (MIC) - *virtual*, 2021.

E-POSTER WITH PRESENTATION IN INTERNATIONAL CONFERENCES

A. Merlet, B. Presles, K. H. Su, A. Cochet, J.-M. Vrigneaud. Development and validation of a Monte Carlo model for a SiPM-based PET scanner. Eur J Nucl Med Mol Imaging, Vol 49, Suppl 1, S345. EANM-*Barcelona*, 2022.

E-POSTER IN INTERNATIONAL CONFERENCES

J. Salvadori, **A. Merlet**, B. Presles, A. Etxebeste, J.-M. Vrigneaud, D. Sarrut. PET digitization chain for Monte Carlo simulation in GATE. Eur J Nucl Med Mol Imaging, Vol 50, Suppl 1, S690. EANM-*Vienna*, 2023.

ORAL PRESENTATION IN INTERNATIONAL WORKSHOPS

H. Jozi, F. Sayah, **A. Merlet**, B. Presles, A. Cochet, and J.-M. Vrigneaud. Dynamic PET simulations of breast cancer patients using GATE. OpenGate Meeting- *virtual*, 2022.

BIBLIOGRAPHY

Agostinelli, S., Allison, J., Amako, K., Apostolakis, J., Araujo, H., Arce, P., Asai, M., Axen, D., Banerjee, S., Barrand, G., Behner, F., Bellagamba, L., Boudreau, J., Broglia, L., Brunengo, A., Burkhardt, H., Chauvie, S., Chuma, J., Chytracek, R., Cooperman, G., Cosmo, G., Degtyarenko, P., Dell'Acqua, A., Depaola, G., Dietrich, D., Enami, R., Feliciello, A., Ferguson, C., Fesefeldt, H., Folger, G., Foppiano, F., Forti, A., Garelli, S., Giani, S., Giannitrapani, R., Gibin, D., Gomez Cadenas, J. J., Gonzalez, I., Gracia Abril, G., Greeniaus, G., Greiner, W., Grichine, V., Grossheim, A., Guatelli, S., Gumplinger, P., Hamatsu, R., Hashimoto, K., Hasui, H., Heikkinen, A., Howard, A., Ivanchenko, V., Johnson, A., Jones, F. W., Kallenbach, J., Kanaya, N., Kawabata, M., Kawabata, Y., Kawaguti, M., Kelner, S., Kent, P., Kimura, A., Kodama, T., Kokoulin, R., Kossov, M., Kurashige, H., Lamanna, E., Lampen, T., Lara, V., Lefebure, V., Lei, F., Liendl, M., Lockman, W., Longo, F., Magni, S., Maire, M., Medernach, E., Minamimoto, K., Mora de Freitas, P., Morita, Y., Murakami, K., Nagamatu, M., Nartallo, R., Nieminen, P., Nishimura, T., Ohtsubo, K., Okamura, M., O'Neale, S., Oohata, Y., Paech, K., Perl, J., Pfeiffer, A., Pia, M. G., Ranjard, F., Rybin, A., Sadilov, S., di Salvo, E., Santin, G., Sasaki, T., Savvas, N., Sawada, Y., Scherer, S., Sei, S., Sirotenko, V., Smith, D., Starkov, N., Stoecker, H., Sulkimo, J., Takahata, M., Tanaka, S., Tcherniaev, E., Safai Tehrani, E., Tropeano, M., Truscott, P., Uno, H., Urban, L., Urban, P., Verderi, M., Walkden, A., Wander, W., Weber, H., Wellisch, J. P., Wenaus, T., Williams, D. C., Wright, D., Yamada, T., Yoshida, H., and Zschiesche, D. (2003). **GEANT4 - A simulation toolkit**. *Nuclear Instruments and Methods in Physics Research, Section A: Accelerators, Spectrometers, Detectors and Associated Equipment*, 506(3):250–303.

Ahn, S., and Fessler, J. A. (2003). **Globally convergent image reconstruction for emission tomography using relaxed ordered subsets algorithms**. *IEEE Transactions on Medical Imaging*, 22(5):613–626.

Alessio, A. M., and Kinahan, P. E. (2008). **Application of a spatially variant system model for 3-D whole-body PET image reconstruction**. *2008 5th IEEE International Symposium on Biomedical Imaging: From Nano to Macro, Proceedings, ISBI*, 5(1):1315–1318.

Alessio, A. M., Kinahan, P. E., and Lewellen, T. K. (2006). **Modeling and incorporation of system response functions in 3-D whole body PET**. *IEEE Transactions on Medical Imaging*, 25(7):828–837.

Badawi, R. D., and Marsden, P. K. (1999). **Developments in component-based normalization for 3D PET**. *Physics in Medicine and Biology*, 44(2):571–594.

Bettinardi, V., Castiglioni, I., De Bernardi, E., and Gilardi, M. C. (2014). **PET quantification: Strategies for partial volume correction**. *Clinical and Translational Imaging*, 2(3):199–218.

Brasse, D., Kinahan, P. E., Lartizien, C., Comtat, C., Casey, M., and Michel, C. (2005). **Correction methods for random coincidences in fully 3D whole-body PET: Impact on data and image quality**. *Journal of Nuclear Medicine*, 46(5):859–867.

Burger, C., Goerres, G., Schoenes, S., Buck, A., Lonn, A., and Von Schulthess, G. (2002). **PET attenuation coefficients from CT images: Experimental evaluation of the transformation of CT into PET 511-keV attenuation coefficients**. *European Journal of Nuclear Medicine*, 29(7):922–927.

Buvat, I., and Castiglioni, I. (2002). **Monte Carlo simulations in SPET and PET**. *Quarterly Journal of Nuclear Medicine*, 46(1):48–61.

Buvat, I., and Lazaro, D. (2006). **Monte Carlo simulations in emission tomography and GATE: An overview**. *Nuclear Instruments and Methods in Physics Research, Section A: Accelerators, Spectrometers, Detectors and Associated Equipment*, 569(2 SPEC. ISS.):323–329.

Cai, L., Gao, J., and Zhao, D. (2020). **A review of the application of deep learning in medical image classification and segmentation**. *Annals of Translational Medicine*, 8(11):713–713.

Casey, M. E., and Nutt, R. (1986). **A multicrystal two dimensional bgo detector system for positron emission tomography**. *IEEE Transactions on Nuclear Science*, 33(1):460–463.

Cherry, S. R., Sorenson, J. A., and Phelps, M. E. (2012). **Physics in Nuclear Medicine**. Elsevier Saunders.

Chicheportiche, A., Marciano, R., and Orevi, M. (2020). **Comparison of NEMA characterizations for Discovery MI and Discovery MI-DR TOF PET/CT systems at different sites and with other commercial PET/CT systems**. *EJNMMI Physics*, 7(1).

Comanor, K. A., Virador, P. R., and Moses, W. W. (1996). **Algorithms to identify detector compton scatter in pet modules**. *IEEE Transactions on Nuclear Science*, 43(4 PART 1):2213–2218.

Conti, M., and Eriksson, L. (2016). **Physics of pure and non-pure positron emitters for PET: A review and a discussion**. *EJNMMI Physics*, 3(1).

Conti, M., Hong, I., and Michel, C. (2012). **Reconstruction of scattered and unscattered PET coincidences using TOF and energy information**. *Physics in Medicine and Biology*, 57(15).

Dahlbom, M., Schiepers, C., and Czernin, J. (2005). **Comparison of noise equivalent count rates and image noise**. *IEEE Transactions on Nuclear Science*, 52(5 I):1386–1390.

Daube-Witherspoon, M. E., Carson, R. E., and Green, M. V. (1988). **Post-injection transmission attenuation measurements for PET**. *IEEE Transactions on Nuclear Science*, 35(1):757–761.

Daube-Witherspoon, M. E., and Muehllehner, G. (1987). **Treatment of axial data in three-dimensional PET**. *Journal of Nuclear Medicine*, 28(11):1717–1724.

De Pierro, A. R., and Yamagishi, M. E. B. (2001). **Fast EM-like methods for maximum "a posteriori" estimates in emission tomography**. *IEEE Transactions on Medical Imaging*, 20(4):280–288.

Defrise, M., Kinahan, P. E., Townsend, D. W., Michel, C., Sibomana, M., and Newport, D. F. (1997). **Exact and approximate rebinning algorithms for 3-d pet data**. *IEEE Transactions on Medical Imaging*, 16(2):145–158.

Delso, G., Martinez, M. J., Torres, I., Ladebeck, R., Michel, C., Nekolla, S., and Ziegler, S. I. (2009). **Monte carlo simulations of the count rate performance of a clinical whole-body MR/PET scanner**. *Medical Physics*, 36(9):4126–4135.

Dempster, A. P., Laird, N. M., and Rubin, D. B. (1977). **Maximum Likelihood from Incomplete Data Via the EM Algorithm** . *Journal of the Royal Statistical Society: Series B (Methodological)*, 39(1):1–22.

Dönmez, S. (2017). **Radiation Detection and Measurement**. John Wiley.

España, S., Herraiz, J. L., Vicente, E., Vaquero, J. J., Desco, M., and Udias, J. M. (2009). **PeneloPET, a Monte Carlo PET simulation tool based on PENELOPE: Features and validation**. *Physics in Medicine and Biology*, 54(6):1723–1742.

GE Healthcare (2016a). **Discovery MI Gen2 Datasheet ™**.

GE Healthcare (2016b). **Discovery MI with LightBurst Digital 4-Ring Detector**.

Gilbert, P. (1972). **Iterative methods for the three-dimensional reconstruction of an object from projections**. *Journal of Theoretical Biology*, 36(1):105–117.

Gordon, R., Bender, R., and Herman, G. T. (1970). **Algebraic Reconstruction Techniques (ART) for three-dimensional electron microscopy and X-ray photography**. *Journal of Theoretical Biology*, 29(3):471–481.

Gundacker, S. (2014). **Time resolution in scintillator based detectors for positron emission tomography**. PhD thesis, Atominstitut der Technischen Universität Wien.

Gundacker, S., Martinez Turtos, R., Kratochwil, N., Pots, R. H., Paganoni, M., Lecoq, P., and Auffray, E. (2020). **Experimental time resolution limits of modern SiPMs and TOF-PET detectors exploring different scintillators and Cherenkov emission**. *Physics in Medicine and Biology*, 65(2).

Han, B. (2021). **Application of deep learning in medical imaging**. *Proceedings - 2021 2nd International Conference on Computing and Data Science, CDS 2021*, 16(4):49–56.

Harpen, M. D. (2004). **Positronium: Review of symmetry, conserved quantities and decay for the radiological physicist**. *Medical Physics*, 31(1):57–61.

Hoffman, E. J., Guerrero, T. M., Dahlbom, M., and Medicine, N. (1989). **PET system calibrations and corrections for quantitative and spatially accurate images**. *IEEE Transactions on Nuclear Science*, 36(1):1108–1112.

Hsu, D. F., Ilan, E., Peterson, W. T., Uribe, J., Lubberink, M., and Levin, C. S. (2017). **Studies of a next-generation silicon-photomultiplier-based time-of-flight PET/CT system**. *Journal of Nuclear Medicine*, 58(9):1511–1518.

Hudson, H. M., and Larkin, R. S. (1994). **Ordered Subsets of Projection Data**. *IEEE transactions on medical imaging*, 13(4):601–609.

Iatrou, M., Manjeshwar, R. M., Ross, S. G., Thielemans, K., and Stearns, C. W. (2006). **3D implementation of Scatter Estimation in 3D PET**. *IEEE Nuclear Science Symposium Conference Record*, 4:2142–2145.

Iatrou, M., Manjeshwar, R. M., and Stearns, C. W. (2007). **Comparison of two 3D implementations of TOF Scatter Estimation in 3D PET**. *IEEE Nuclear Science Symposium Conference Record*, 5:3474–3477.

Iatrou, M., Ross, S. G., Manjeshwar, R. M., and Stearns, C. W. (2004). **A fully 3D iterative image reconstruction algorithm incorporating data corrections**. *IEEE Nuclear Science Symposium Conference Record*, 4(C):2493–2497.

Iriarte, A., Marabini, R., Matej, S., Sorzano, C. O., and Lewitt, R. M. (2016). **System models for PET statistical iterative reconstruction: A review**. *Computerized Medical Imaging and Graphics*, 48:30–48.

Jan, S., Benoit, D., Becheva, E., Carlier, T., Cassol, F., Descourt, P., Frisson, T., Grevillot, L., Guigues, L., Maigne, L., Morel, C., Perrot, Y., Rehfeld, N., Sarrut, D., Schaart, D. R., Stute, S., Pietrzyk, U., Visvikis, D., Zahra, N., and Buvat, I. (2011). **GATE V6: A major enhancement of the GATE simulation platform enabling modelling of CT and radiotherapy**. *Physics in Medicine and Biology*, 56(4):881–901.

Jan, S., Santin, G., Strul, D., Staelens, S., Assié, K., Autret, D., Avner, S., Barbier, R., Bardiès, M., Bloomfield, P. M., Brasse, D., Breton, V., Bruyndonckx, P., Buvat, I., Chatziioannou, A. F., Choi, Y., Chung, Y. H., Comtat, C., Donnarieix, D., Ferrer, L., Glick, S. J., Groiselle, C. J., Guez, D., Honore, P. F., Kerhoas-Cavata, S., Kirov, A. S., Kohli, V., Koole, M., Krieguer, M., van der Laan, D. J., Lamare, F., Largeron, G., Lartizien, C., Lazaro, D., Maas, M. C., Maigne, L., Mayet, F., Melot, F., Merheb, C., Pennacchio, E., Perez, J., Pietrzyk, U., Rannou, F. R., Rey, M., Schaart, D. R., Schmidtlein, C. R., Simon, L., Song, T. Y., Vieira, J. M., Visvikis, D., Van de Walle, R., Wieërs, E., and Morel, C. (2004). **GATE: A simulation toolkit for PET and SPECT**. *Physics in Medicine and Biology*, 49(19):4543–4561.

Johnson, C. A., Yan, Y., Carson, R. E., Martino, R. L., and Daube-Witherspoon, M. E. (1995). **A System for the 3D Reconstruction of Retracted-Septa PET Data Using the EM Algorithm**. *IEEE Transactions on Nuclear Science*, 42(4):1223–1227.

Jozi, H. S. (2022). **Dynamic PET simulations of breast cancer patients using GATE**. Grenoble INP - Phelma, UGA.

Kalaitzidis, P., Gustafsson, J., Hindorf, C., and Ljungberg, M. (2022). **Validation of a computational chain from PET Monte Carlo simulations to reconstructed images**. *Heliyon*, 8(4):e09316.

Khalif, M., Stute, S., Wagadarikar, A., and Comtat, C. (2016). **Modeling the GE Signa PET-MR with Monte-Carlo Simulations using GATE**. *IEEE Nuclear Science Symposium and Medical Imaging Conference*.

Kinahan, P. E., Defrise, M., and Clackdoyle, R. (2004). **Analytic Image Reconstruction Methods**. Elsevier Inc.

Kinahan, P. E., Townsend, D. W., Beyer, T., and Sashin, D. (1998). **Attenuation correction for a combined 3D PET/CT scanner**. *Medical Physics*, 25(10):2046–2063.

Kowalski, P., Wiślicki, W., Shopa, R. Y., Raczyński, L., Klimaszewski, K., Curcenau, C., Czerwiński, E., Dulski, K., Gajos, A., Gorgol, M., Gupta-Sharma, N., Hiesmayr, B., Jasińska, B., Kapłon, L., Kisielewska-Kamińska, D., Korcyl, G., Kozik, T., Krzemień, W., Kubicz, E., Mohammed, M., Niedźwiecki, S., Pałka, M., Pawlik-Niedźwiecka, M., Raj, J., Rakoczy, K., Rudy, Z., Sharma, S., Shivani, S., Silarski, M., Skurzok, M., Zgardzińska, B., Zieliński, M., and Moskal, P. (2018). **Estimating the NEMA characteristics of the J-PET tomograph using the GATE package**. *Physics in Medicine and Biology*, 63(16).

Lamare, F., Turzo, A., Bizais, Y., Rest, C. C. L., and Visvikis, D. (2006). **Validation of a Monte Carlo simulation of the Philips Allegro/GEMINI PET systems using GATE**. *Physics in Medicine and Biology*, 51(4):943–962.

Levin, C. S., and Hoffman, E. J. (1999). **Calculation of positron range and its effect on the fundamental limit of positron emission tomography system spatial resolution**. *Physics in Medicine and Biology*, 44(3):781–799.

Lewitt, R. M. (1992). **Alternatives to voxels for image representation in iterative reconstruction algorithms**. *Physics in Medicine and Biology*, 37(3):705–716.

Li, S., Zhang, Q., Vuletic, I., Xie, Z., Yang, K., and Ren, Q. (2017). **Monte Carlo simulation of Ray-Scan 64 PET system and performance evaluation using GATE toolkit**. *Journal of Instrumentation*, 12(2).

Lindström, E., Lindsjö, L., Sundin, A., Sörensen, J., and Lubberink, M. (2020). **Evaluation of block-sequential regularized expectation maximization reconstruction of 68Ga-DOTATOC, 18F-fluoride, and 11C-acetate whole-body examinations acquired on a digital time-of-flight PET/CT scanner**. *EJNMMI Physics*, 7(1):1–14.

Lodge, M. A., Badawi, R. D., Gilbert, . R., Dibos, P. E., and Line, B. R. (2006). **Comparison of 2-Dimensional and 3-Dimensional Acquisition for 18 F-FDG PET Oncology Studies Performed on an LSO-Based Scanner COMPARISON OF 2D AND 3D PET ACQUISITION • Lodge et al. 23**. *J Nucl Med*, 47:23–31.

Lu, L., Zhang, H., Bian, Z., Ma, J., Feng, Q., and Chen, W. (2016). **Validation of a Monte Carlo simulation of the Inveon PET scanner using GATE**. *Nuclear Instruments and Methods in Physics Research, Section A: Accelerators, Spectrometers, Detectors and Associated Equipment*, 828:170–175.

Medicine, N. (1995). **1995 International Meeting on Fully Three-Dimensional Image Reconstruction in Radiology .** *Proceedings of the 3rd International Meeting on Fully Three-Dimensional Image Reconstruction in Radiology and Nuclear Medicine*, pages 67–71.

Moses, W. W. (2011). **Fundamental limits of spatial resolution in PET**. *Nuclear Instruments and Methods in Physics Research, Section A: Accelerators, Spectrometers, Detectors and Associated Equipment*, 648(SUPPL. 1):S236–S240.

Nuyts, J., Bequé, D., Dupont, P., and Mortelmans, L. (2002). **A concave prior penalizing relative differences for maximum-a-posteriori reconstruction in emission tomography**. *IEEE Transactions on Nuclear Science*, 49(1 I):56–60.

Oliver, J. F., and Rafecas, M. (2010). **Improving the singles rate method for modeling accidental coincidences in high-resolution PET**. *Physics in Medicine and Biology*, 55(22):6951–6971.

Oliver, J. F., and Rafecas, M. (2016). **Modelling random coincidences in positron emission tomography by using singles and prompts: A comparison study**. *PLoS ONE*, 11(9):1–22.

Ollinger, J. M. (1995). **Detector Efficiency and Compton Scatter in Fully 3D PET**. *IEEE Transactions on Nuclear Science*, 42(4):1168–1173.

Panin, V. Y., Kehren, F., Michel, C., and Casey, M. (2006). **Fully 3-D PET reconstruction with system matrix derived from point source measurements**. *IEEE Transactions on Medical Imaging*, 25(7):907–921.

Park, H., Yi, M., and Lee, J. S. (2022). **Silicon photomultiplier signal readout and multiplexing techniques for positron emission tomography: a review**. *Biomedical Engineering Letters*, 12(3):263–283.

Pépin, A., Stute, S., Jan, S., and Comtat, C. (2011). **Normalization of Monte Carlo PET data using GATE**. In *IEEE Nuclear Science Symposium Conference Record*, pages 4196–4200. Institute of Electrical and Electronics Engineers Inc.

Pfaehler, E., De Jong, J. R., Dierckx, R. A., van Velden, F. H., and Boellaard, R. (2018). **SMART (SiMulAtion and ReconsTruction) PET: an efficient PET simulation-reconstruction tool**. *EJNMMI Physics*, 5(1).

Polycarpou, I., Thielemans, K., Manjeshwar, R., Aguiar, P., Marsden, P. K., and Tsoumpas, C. (2011). **Comparative evaluation of scatter correction in 3D PET using different scatter-level approximations**. *Annals of Nuclear Medicine*, 25(9):643–649.

Qi, J. (2005). **Calculation of the sensitivity image in list-mode reconstruction**. *IEEE Nuclear Science Symposium Conference Record*, 4(5):1924–1928.

Qi, J., Leahy, R. M., Cherry, S. R., Chatziioannou, A., and Farquhar, T. H. (1998). **High-resolution 3D bayesian image reconstruction using the microPET small-animal scanner**. *Physics in Medicine and Biology*, 43(4):1001–1013.

Rahmim, A., Qi, J., and Sossi, V. (2013). **Resolution modeling in PET imaging: Theory, practice, benefits, and pitfalls**. *Medical Physics*, 40(6).

Rahmim, A., Tang, J., Lodge, M. A., Lashkari, S., Ay, M. R., Lautamäki, R., Tsui, B. M., and Bengel, F. M. (2008). **Analytic system matrix resolution modeling in PET: An application to Rb-82 cardiac imaging**. *Physics in Medicine and Biology*, 53(21):5947–5965.

Rapisarda, E., Bettinardi, V., Thielemans, K., and Gilardi, M. C. (2010). **Image-based point spread function implementation in a fully 3D OSEM reconstruction algorithm for PET**. *Physics in Medicine and Biology*, 55(14):4131–4151.

Rausch, I., Ruiz, A., Valverde-Pascual, I., Cal-González, J., Beyer, T., and Carrio, I. (2019). **Performance evaluation of the VereoS PET/CT system according to the NEMA NU2-2012 standard**. *Journal of Nuclear Medicine*, 60(4):561–567.

Reddin, J. S., Scheuermann, J. S., Bharkhada, D., Smith, A. M., Casey, M. E., Conti, M., and Karp, J. S. (2018). **Performance Evaluation of the SiPM-based Siemens Biograph Vision PET/CT System**. *2018 IEEE Nuclear Science Symposium and Medical Imaging Conference, NSS/MIC 2018 - Proceedings*, pages 1–5.

Renaud, J. M., Yip, K., Guimond, J., Trottier, M., Pibarot, P., Turcotte, E., Maguire, C., Lalonde, L., Gulenchyn, K., Farncombe, T., Wisenberg, G., Moody, J., Lee, B., Port, S. C., Turkington, T. G., Beanlands, R. S., and DeKemp, R. A. (2017). **Characterization of 3-Dimensional PET systems for accurate quantification of myocardial blood flow**. *Journal of Nuclear Medicine*, 58(1):103–109.

Reynés-Llompart, G., Gámez-Cenzano, C., Vercher-Conejero, J. L., Sabaté-Llobera, A., Calvo-Malvar, N., and Martí-Climent, J. M. (2018). **Phantom, clinical, and texture indices evaluation and optimization of a penalized-likelihood image reconstruction method (Q.Clear) on a BGO PET/CT scanner**. *Medical Physics*, 45(7):3214–3222.

Rising, M. E., Armstrong, J. C., Bolding, S. R., Brown, F. B., Bull, J. S., Burke, T. P., Clark, A. R., Dixon, D. A., Forster III, R. A., Giron, J. F., Grieve, T. S., Hughes III, H. G., Josey, C. J., Kulesza, J. A., Martz, R. L., McCartney, A. P., McKinney, G. W., Mosher, S. W., Pearson, E. J., Solomon Jr., C. J., Swaminarayan, S., Sweezy, J. E., Wilson, S. C., and Zukaitis, A. J. (2023). **MCNP Code Version 6.3.0 Release Notes**. Los Alamos National Laboratory, Los Alamos, NM, USA.

Rogers, D. W. (2006). **Fifty years of Monte Carlo simulations for medical physics**. *Physics in Medicine and Biology*, 51(13).

Ross, S. (2014). **Q.Clear**. *GE Healthcare, White Paper*, page 1–9.

Salvadori, J. (2020). **Caractérisation, optimisation et simulation des performances d'un TEP-TDM numérique**. PhD thesis, Université de Lorraine.

Salvadori, J., Labour, J., Odille, F., Marie, P. Y., Badel, J. N., Imbert, L., and Sarrut, D. (2020). **Monte Carlo simulation of digital photon counting PET**. *EJNMMI Physics*, 7(1):1–16.

Sarrut, D., Bała, M., Bardi s, M., Bert, J., Chauvin, M., Chatzipapas, K., Dupont, M., Etxebeste, A., Fanchon, L. M., Jan, S., Kayal, G., Kirov, A. S., Kowalski, P., Krzemien, W., Labour, J., Lenz, M., Loudos, G., Mehadji, B., Ménard, L., Morel, C., Papadimitroulas, P., Rafecas, M., Salvadori, J., Seiter, D., Stockhoff, M., Testa, E., Trigila, C., Pietrzyk, U., Vandenberghe, S., Verdier, M. A., Visvikis, D., Ziemons, K., Zvolský, M., and Roncali, E. (2021). **Advanced Monte Carlo simulations of emission tomography imaging systems with GATE**. *Physics in Medicine and Biology*, 66(10).

Sayah, F. (2021). **Génération de paires d' images dynamiques TEP idéales / bruitées pour entraîner un algorithme d' apprentissage profond**. Université Toulouse III, FSI-RMGBM.

Schmidtlein, C. R., Kirov, A. S., Nehmen, S. A., Erdi, Y. E., Humm, J. L., Amols, H. I., Bidaut, L. M., Ganin, A., Stearns, C. W., McDaniel, D. L., and Hamacher, K. A. (2006). **Validation of GATE Monte Carlo simulations of the GE Advance/Discovery LS PET scanners**. *Medical Physics*, 33(1):198–208.

Shao, Y., Cherry, S. R., Siegel, S., and Silverman, R. W. (1996). **A Study of inter-crystal scatter in small scintillator arrays designed for high resolution PET imaging**. *IEEE Transactions on Nuclear Science*, 43(3 PART 2):1938–1944.

Sheen, H., Im, K. C., Choi, Y., Shin, H., Han, Y., Chung, K., Cho, J., and Ahn, S. H. (2014). **GATE Monte Carlo simulation of GE Discovery 600 and a uniformity phantom**. *Journal of the Korean Physical Society*, 65(11):1802–1808.

Shepp, L. A., and Vardi, Y. (1982). **Maximum Likelihood Reconstruction for Emission Tomography**. *IEEE Transactions on Medical Imaging*, 1(2):113–122.

Simon, L., Strul, D., Santin, G., Krieguer, M., and Morel, C. (2004). **Simulation of time curves in small animal PET using GATE**. *Nuclear Instruments and Methods in Physics Research, Section A: Accelerators, Spectrometers, Detectors and Associated Equipment*, 527(1-2):190–194.

Soret, M., Bacharach, S. L., and Buvat, I. (2007). **Partial-volume effect in PET tumor imaging**. *Journal of Nuclear Medicine*, 48(6):932–945.

Staelens, S., D'Asseler, Y., Vandenberghe, S., Koole, M., Lemahieu, I., and Van de Walle, R. (2004). **A three-dimensional theoretical model incorporating spatial detection uncertainty in continuous detector PET**. *Physics in Medicine and Biology*, 49(11):2337–2350.

Stearns, C. W., McDaniel, D. L., Kohlmyer, S. G., Arul, P. R., Geiser, B. P., and Shanmugam, V. (2003). **Random coincidence estimation from single event rates on the Discovery ST PET/CT scanner**. In *IEEE Nuclear Science Symposium Conference Record*, volume 5, pages 3067–3069.

Strother, S. C., Casey, M. E., and Hoffman, E. J. (1990). **Measuring PET Scanner Sensitivity: Relating Countrates to Image Signal-to-Noise Ratios using Noise Equivalent Counts**. *IEEE Transactions on Nuclear Science*, 37(2):783–788.

Strydhorst, J., and Buvat, I. (2016). **Redesign of the GATE PET coincidence sorter**. *Physics in Medicine and Biology*, 61(18):N522–N531.

Teimoorisichani, M., and Goertzen, A. L. (2019). **Count rate performance of brain-dedicated PET scanners: A Monte Carlo simulation study**. *Physics in Medicine and Biology*, 64(21):0–27.

Teoh, E. J., McGowan, D. R., Macpherson, R. E., Bradley, K. M., and Gleeson, F. V. (2015). **Phantom and clinical evaluation of the Bayesian penalized likelihood reconstruction algorithm Q.Clear on an LYSO PET/CT system**. *Journal of Nuclear Medicine*, 56(9):1447–1452.

Tiwari, A., Merrick, M., Graves, S. A., and Sunderland, J. (2022). **Monte Carlo evaluation of hypothetical long axial field-of-view PET scanner using GE Discovery MI PET front-end architecture**. *Medical Physics*, 49(2):1139–1152.

Tohme, M. S., and Qi, J. (2009). **Iterative image reconstruction for positron emission tomography based on a detector response function estimated from point source measurements**. *Physics in Medicine and Biology*, 54(12):3709–3725.

Tong, S., Alessio, A. M., and Kinahan, P. E. (2010). **Noise and signal properties in PSF-based fully 3D PET image reconstruction: An experimental evaluation**. *Physics in Medicine and Biology*, 55(5):1453–1473.

Torres-Espallardo, I., Rafecas, M., Spanoudaki, V., McElroy, D. P., and Ziegler, S. I. (2008). **Effect of inter-crystal scatter on estimation methods for random coincidences and subsequent correction**. *Physics in Medicine and Biology*, 53(9):2391–2411.

Uribe, J., McDaniel, D. L., and Stearns, C. W. (2013). **Coincidence Time Correction (CTC) method for TOF-PET scanners with correction to account for misalignment of calibration phantom**. *IEEE Nuclear Science Symposium Conference Record*, 53188:13–15.

Veklerov, E., and Llacer, J. (1987). **Stopping Rule for the MLE Algorithm Based on Statistical Hypothesis Testing**. *IEEE Transactions on Medical Imaging*, 6(4):313–319.

Vicente, E., Herraiz, J. L., España, S., Herranz, E., Desco, M., Vaquero, J. J., and Udías, J. M. (2013). **Improved dead-time correction for PET scanners: Application to small-animal PET**. *Physics in Medicine and Biology*, 58(7):2059–2072.

Wagadarikar, A. A., Ivan, A., Dolinsky, S., and McDaniel, D. L. (2014). **Sensitivity improvement of time-of-flight (ToF) PET detector through recovery of compton scattered annihilation photons**. In *IEEE Transactions on Nuclear Science*, volume 61, pages 121–125. IEEE.

Wagatsuma, K., Miwa, K., Sakata, M., Oda, K., Ono, H., Kameyama, M., Toyohara, J., and Ishii, K. (2017). **Comparison between new-generation SiPM-based and conventional PMT-based TOF-PET/CT**. *Physica Medica*, 42:203–210.

Wang, G. C., Li, X., Niu, X., Du, H., Balakrishnan, K., Ye, H., and Burr, K. (2016). **PET Timing Performance Measurement Method Using NEMA NEC Phantom**. *IEEE Transactions on Nuclear Science*, 63(3):1335–1342.

Watson, C. C. (2000). **New, faster, image-based scatter correction for 3D PET**. *IEEE Transactions on Nuclear Science*, 47(4 PART 2):1587–1594.

Watson, C. C. (2007). **Extension of single scatter simulation to scatter correction of time-of-flight PET**. *IEEE Transactions on Nuclear Science*, 54(5):1679–1686.

Watson, C. C., Hu, J., and Zhou, C. (2018). **Extension of the SSS PET scatter correction algorithm to include double scatter**. *2018 IEEE Nuclear Science Symposium and Medical Imaging Conference, NSS/MIC 2018 - Proceedings*, pages 1–4.

Watson, C. C., Hu, J., and Zhou, C. (2020). **Double Scatter Simulation for More Accurate Image Reconstruction in Positron Emission Tomography**. *IEEE Transactions on Radiation and Plasma Medical Sciences*, 4(5):570–584.

Watson, C. C., Newport, D., and Casey, M. E. (1996). **A Single Scatter Simulation Technique for Scatter Correction in 3D PET**. *Three-Dimensional Image Reconstruction in Radiation and Nuclear Medicine*, pages 255–268.

Watson, C. C., Newport, D., Casey, M. E., Dekemp, R. A., Beanlands, R. S., and Schmand, M. (1997). **Evaluation of simulation-based scatter correction for 3-D PET cardiac imaging**. *IEEE Transactions on Nuclear Science*, 44(1):90–97.

Werner, M. E., Surti, S., and Karp, J. S. (2006). **Implementation and evaluation of a 3D PET single scatter simulation with TOF modeling**. *IEEE Nuclear Science Symposium Conference Record*, 3:1768–1773.

Yamamoto, S., Amano, M., Miura, S., Iida, H., and Kanno, I. (1986). **Deadtime correction method using random coincidence for PET**. *Journal of Nuclear Medicine*, 27(12):1925–1928.

Yamaya, T., Hagiwara, N., Obi, T., Yamaguchi, M., Ohyama, N., Kitamura, K., Hasegawa, T., Haneishi, H., Yoshida, E., Inadama, N., and Murayama, H. (2005). **Transaxial system models for jPET-D4 image reconstruction**. *Physics in Medicine and Biology*, 50(22):5339–5355.

Zaidi, H. (1999). **Relevance of accurate Monte Carlo modeling in nuclear medical imaging**. *Medical Physics*, 26(4):574–608.

Zaidi, H. (2000). **Comparative evaluation of scatter correction techniques in 3D positron emission tomography**. *European Journal of Nuclear Medicine*, 27(12):1813–1826.

Zaidi, H., and Koral, K. F. (2004). **Scatter modelling and compensation in emission tomography**. *European Journal of Nuclear Medicine and Molecular Imaging*, 31(5):761–782.

Zaidi, H., and Montandon, M. L. (2007). **Scatter Compensation Techniques in PET**. *PET Clinics*, 2(2):219–234.

Zeimpekis, K. G., Kotasidis, F. A., Huellner, M., Nemirovsky, A., Kaufmann, P. A., and Treyer, V. (2022). **NEMA NU 2–2018 performance evaluation of a new generation 30-cm axial field-of-view Discovery MI PET/CT**. *European Journal of Nuclear Medicine and Molecular Imaging*, 49(9):3023–3032.

Zhang, C., Sang, Z., Wang, X., Zhang, X., and Yang, Y. (2019a). **The effects of inter-crystal scattering events on the performance of PET detectors**. *Physics in Medicine and Biology*, 64(20).

Zhang, W., Gao, J., Yang, Y., Liang, D., Liu, X., Zheng, H., and Hu, Z. (2019b). **Image reconstruction for positron emission tomography based on patch-based regularization and dictionary learning**. *Medical Physics*, 46(11):5014–5026.

III

ANNEXES

A

EXPERIMENTAL AND VALIDATION DATA

A.1/ NEMA SENSITIVITY

Table A.1 shows the sensitivity results evaluated with the GE console and with NEAT for years 2017, 2020, and 2022. Year 2021 was presented in Section 9.3.1. Across all years, the sensitivities obtained with GE console and with NEAT were below 1% relative difference. Figure A.1 show the axial sensitivity profiles for these years, where the maximum relative difference between GE console and NEAT was 9.29% for year 2022.

Table A.1: Sensitivity results (in cps.kBq^{-1}) for our four realisations evaluated with the GE console and with NEAT.

Source Position	GE Console				NEAT			
	2017	2020	2021	2022	2017	2020	2021	2022
CFOV	12.91	12.81	12.90	13.16	12.92	12.80	12.90	13.17
10 cm radial offset	13.21	12.83	13.03	12.96	13.21	12.83	13.03	12.96

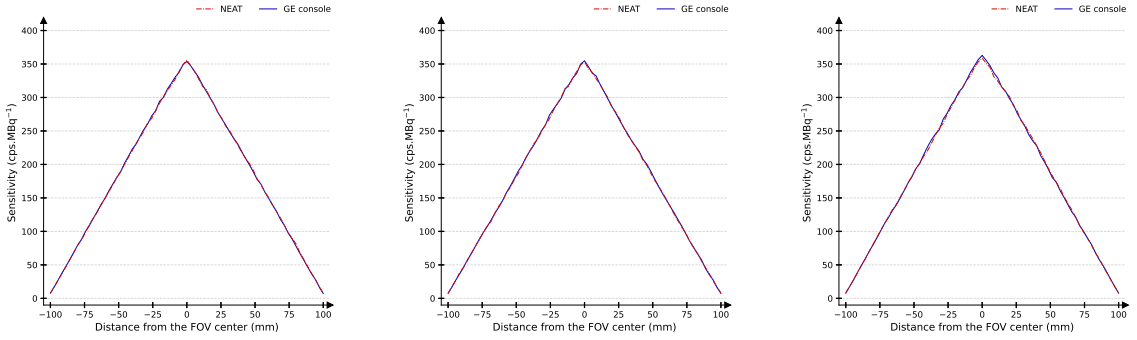

(a) **(b)** **(c)**

Figure A.1: Comparison of axial sensitivity profiles for NEAT (in red) and the GE console (in blue), with a source placed at the CFOV. The maximum relative differences were **(a)** 4.96% for year 2017, **(b)** 5.67% for year 2020, and **(c)** 9.29% for year 2022.

A.2/ NEMA COUNT LOSSES AND SCATTER FRACTION

The experimental data obtained in Section 9.3.2 was processed in NEAT, and the results are presented in Table A.2. The relative differences between NEAT and the GE console for several metrics of the NEMA count losses and scatter fraction standard are shown in Table A.3. During the development of NEAT, large differences with the GE console were observed when the activity concentration was more than 35 kBq.mL^{-1}, likely due to cut-off effects in the GE console processing. As an example, at an average activity concentration of 36.2 kBq.mL^{-1} in 2017, the associated scatter and random rates RDs were 10.7% and 6.4%, respectively. When considering the second frame (33 kBq.mL^{-1}), the scatter and random rates RDs dropped to 3.6% and 3.3%, which was similar to the largest RDs observed for other years.

Table A.2: Metrics for the NEMA count losses and scatter fraction test. The results were calculated with NEAT for the years 2017, 2020, and 2021.

Measurement	**NEAT**		
	2017	2020	2021
NECR			
Peak (kcps)	178.8	170.7	164.5
Activity (kBq.mL^{-1})	22.6	23.5	23.5
True count rate			
Peak (kcps)	809.73	752.46	740.95
Activity (kBq.mL^{-1})	33.0	34.3	31.2
Scatter fraction			
At peak NECR (%)	41.3	42.4	42.5

Table A.3: Validation of NEAT by comparison with the GE console across three years. Differences are calculated in terms of relative difference between the data presented in Table 9.5 (GE console) and Table A.2 (NEAT).

Metric	Neat vs GE console		
	2017	2020	2021
Largest RD (%) across 24 frames			
Prompt rates	2.7	2.6	2.5
Random rates	6.4	3.3	3.2
Scatter rates	10.7	3.7	3.6
True rates	0.4	0.1	0.3
NECR	3.3	2.6	3.0
Peak NECR			
RD (%)	−2.8	−2.3	−2.6
Activity concentration (kBq.mL^{-1})	22.6	23.5	23.5
Peak true count rate			
RD (%)	−0.4	0.0	−0.3
Activity concentration (kBq.mL^{-1})	36.2	34.3	31.2
Scatter fraction at peak NECR			
RD (%)	2.2	0.1	2.1

A.3/ NEMA SPATIAL RESOLUTION

The detail of the yearly NEMA spatial resolution tests is show in Table A.4, where the analysis was performed using the GE console. The same initial data was then processed in NEAT, and the results are presented in Table A.5. Table A.6 contains the relative differences between the GE console and NEAT, obtained using the two former tables. The largest relative difference (6.38%) was observed for the FWTM in the radial direction for a source placed at a 10 cm radial offset in year 2020.

Table A.4: FWHM and FWTM (in mm) values for the spatial resolution test, averaged over both axial source positions. Data were analysed with the GE console for our four acquisitions.

Resolution Direction	GE console mean							
	2017		2020		2021		2022	
	FWHM	FWTM	FWHM	FWTM	FWHM	FWTM	FWHM	FWTM
1 cm radial offset								
Radial	4.52	8.91	4.27	8.97	4.47	8.86	4.26	8.89
Tangential	4.35	8.59	4.22	8.77	4.29	8.57	4.33	8.63
Axial	4.63	10.21	4.49	10.24	4.63	10.29	4.48	10.23
10 cm radial offset								
Radial	5.58	10.56	5.60	10.60	5.58	10.65	5.54	10.50
Tangential	4.69	9.31	4.71	9.40	4.53	9.76	4.70	9.37
Axial	5.52	11.59	5.68	11.65	6.28	11.98	6.11	11.90
20 cm radial offset								
Radial	7.46	14.26	7.44	14.15	7.40	14.14	7.39	14.16
Tangential	5.17	9.60	5.18	9.61	5.18	9.72	5.19	9.63
Axial	6.15	12.06	6.18	12.15	6.27	12.24	5.89	12.11

Table A.5: FWHM and FWTM (in mm) values of four acquisitions averaged over both axial source positions. Data were analysed with NEAT.

Resolution Direction	NEAT mean							
	2017		2020		2021		2022	
	FWHM	FWTM	FWHM	FWTM	FWHM	FWTM	FWHM	FWTM
1 cm radial offset								
Radial	4.40	8.49	4.25	8.47	4.34	8.48	4.16	8.46
Tangential	4.20	8.21	4.09	8.41	4.17	8.20	4.22	8.27
Axial	4.48	9.95	4.27	9.97	4.49	10.07	4.32	9.98
10 cm radial offset								
Radial	5.54	10.41	5.58	10.71	5.67	11.33	5.63	10.95
Tangential	4.52	8.90	4.55	8.92	4.40	9.78	4.56	8.98
Axial	5.32	11.42	5.40	11.35	6.21	11.79	5.97	11.64
20 cm radial offset								
Radial	7.28	14.03	7.22	14.04	7.27	14.35	7.18	13.99
Tangential	5.07	9.69	5.05	9.68	5.10	9.88	5.07	9.68
Axial	6.17	12.19	6.20	12.34	6.29	12.45	5.93	12.20

Table A.6: Relative differences between NEAT (Table A.5) and GE console (Table A.4)

Resolution Direction	RD NEAT vs GE console							
	2017		2020		2021		2022	
	FWHM	FWTM	FWHM	FWTM	FWHM	FWTM	FWHM	FWTM
1 cm radial offset								
Radial	−2.65 %	−4.71 %	−0.35 %	−5.52 %	−2.91 %	−4.29 %	−2.46 %	−4.89 %
Tangential	−3.34 %	−4.37 %	−3.08 %	−4.10 %	−2.80 %	−4.32 %	−2.54 %	−4.23 %
Axial	−3.14 %	−2.55 %	−4.90 %	−2.64 %	−2.92 %	−2.09 %	−3.58 %	−2.40 %
10 cm radial offset								
Radial	−0.63 %	−1.42 %	−0.27 %	1.04%	1.70%	6.38%	1.62%	4.29%
Tangential	−3.62 %	−4.35 %	−3.40 %	−5.06 %	−2.76 %	0.26%	−3.09 %	−4.11 %
Axial	−3.62 %	−1.42 %	−4.85 %	−2.53 %	−1.04 %	−1.59 %	−2.37 %	−2.23 %
20 cm radial offset								
Radial	−2.35 %	−1.58 %	−2.89 %	−0.78 %	−1.76 %	1.49%	−2.78 %	−1.20 %
Tangential	−1.84 %	0.99%	−2.42 %	0.73%	−1.45 %	1.65%	−2.31 %	0.57%
Axial	0.33%	1.12%	0.40%	1.56%	0.40%	1.76%	0.68%	0.78%